



Two-component mantle melting-mixing model for the generation of mid-ocean ridge basalts: Implications for the volatile content of the Pacific upper mantle

Kei Shimizu^{a,*}, Alberto E. Saal^a, Corinne E. Myers^a, Ashley N. Nagle^a,
Erik H. Hauri^b, Donald W. Forsyth^a, Vadim S. Kamenetsky^c, Yaoling Niu^d

^a Department of Earth, Environmental and Planetary Sciences, Brown University, Providence, RI 02912, USA

^b Department of Terrestrial Magnetism, Carnegie Institute of Washington, DC 20015, USA

^c School of Physical Sciences, University of Tasmania, Hobart, Tasmania 7001, Australia

^d Department of Earth Sciences, Durham University, Durham DH1 3LE, UK

Received 2 April 2015; accepted in revised form 28 October 2015; Available online 27 November 2015

Abstract

We report major, trace, and volatile element (CO₂, H₂O, F, Cl, S) contents and Sr, Nd, and Pb isotopes of mid-ocean ridge basalt (MORB) glasses from the Northern East Pacific Rise (NEPR) off-axis seamounts, the Quebrada-Discovery-GoFar (QDG) transform fault system, and the Macquarie Island. The incompatible trace element (ITE) contents of the samples range from highly depleted (DMORB, Th/La ≤ 0.035) to enriched (EMORB, Th/La ≥ 0.07), and the isotopic composition spans the entire range observed in EPR MORB. Our data suggest that at the time of melt generation, the source that generated the EMORB was essentially peridotitic, and that the composition of NMORB might not represent melting of a single upper mantle source (DMM), but rather mixing of melts from a two-component mantle (depleted and enriched DMM or D-DMM and E-DMM, respectively). After filtering the volatile element data for secondary processes (degassing, sulfide saturation, assimilation of seawater-derived component, and fractional crystallization), we use the volatiles to ITE ratios of our samples and a two-component mantle melting-mixing model to estimate the volatile content of the D-DMM (CO₂ = 22 ppm, H₂O = 59 ppm, F = 8 ppm, Cl = 0.4 ppm, and S = 100 ppm) and the E-DMM (CO₂ = 990 ppm, H₂O = 660 ppm, F = 31 ppm, Cl = 22 ppm, and S = 165 ppm). Our two-component mantle melting-mixing model reproduces the kernel density estimates (KDE) of Th/La and ¹⁴³Nd/¹⁴⁴Nd ratios for our samples and for EPR axial MORB compiled from the literature. This model suggests that: (1) 78% of the Pacific upper mantle is highly depleted (D-DMM) while 22% is enriched (E-DMM) in volatile and refractory ITE, (2) the melts produced during variable degrees of melting of the E-DMM controls most of the MORB geochemical variation, and (3) a fraction (~65% to 80%) of the low degree EMORB melts (produced by ~1.3% melting) may escape melt aggregation by freezing at the base of the oceanic lithosphere, significantly enriching it in volatile and trace element contents. Our results are consistent with previously proposed geodynamical processes acting at mid-ocean ridges and with the generation of the E-DMM. Our observations indicate that the D-DMM and E-DMM have (1) a relatively constant CO₂/Cl ratio of ~57 ± 8, and (2) volatile and ITE element abundance patterns that can be related by a simple melting event, supporting the hypothesis that the E-DMM is a recycled oceanic lithosphere mantle metasomatized by low degree melts. Our calculation and model give rise to a Pacific upper mantle with volatile content of CO₂ = 235 ppm, H₂O = 191 ppm, F = 13 ppm, Cl = 5 ppm, and S = 114 ppm.

© 2015 Elsevier Ltd. All rights reserved.

* Corresponding author. Tel.: +1 631 7216378.

E-mail address: kei_shimizu@brown.edu (K. Shimizu).

1. INTRODUCTION

The unique physical properties of the asthenosphere such as low seismic velocity (Nishimura and Forsyth, 1989), high electrical conductivity (Evans et al., 2005), and seismic anisotropy (Forsyth, 1975) have been attributed to either temperature (Priestley and McKenzie, 2006), grain size (Faul and Jackson, 2005), water content (Karato and Jung, 1998) or to the presence of a low melt fraction (Anderson and Spetzler, 1970). We rely on the composition of the asthenosphere to understand the parameters controlling the observed physical properties of this mechanically weak region of the upper mantle; and we resort to geochemical studies of Mid-Ocean Ridge Basalts (MORB) to unravel the composition of the asthenosphere.

In particular, the volatile element composition of the upper mantle provides an essential constraint for understanding mantle melting and melt compositions (Gaetani and Grove, 1998; Asimow and Langmuir, 2003; Dasgupta and Hirschmann, 2006; Hirschmann et al., 2009; Filiberto et al., 2012, 2014; Tenner et al., 2012; Dasgupta et al., 2013), mantle viscosity (Hirth and Kohlstedt, 1996; Jung and Karato, 2001), mantle seismic velocity (Jacobsen et al., 2008; Karato, 2012), mantle heterogeneity (Kingsley and Schilling, 1995; Hauri, 2002; Saal et al., 2002; Simons et al., 2002; Cartigny et al., 2008), and crustal recycling (Javoy et al., 1982; Dixon et al., 2002; Donnelly et al., 2004).

The precise analysis of volatile elements (CO₂, H₂O, F, Cl, S) in quenched MORB glasses can be used to estimate the volatile element composition of the upper mantle. However, due to the presence of long-lived magma chambers, axial MORB from fast spreading ridges like the East Pacific Rise (EPR), experience extensive fractional crystallization and homogenization of magmas through melt aggregation (Batiza and Niu, 1992; Sinton and Detrick, 1992; Langmuir et al., 1993; Niu et al., 1996). To make an accurate estimate of the volatile element composition of the upper mantle, it is important to determine to what extent the geochemical variations in axial MORB do represent a homogeneous mantle composition with variations in the physical conditions of magma generation and transport; or alternatively, whether they are inherited from mixing processes during the aggregation of melts originating from an heterogeneous upper mantle (Batiza et al., 1990; Shen and Forsyth, 1995; Hirschmann and Stolper, 1996; Niu et al., 1999, 2002). In contrast to axial MORB, lavas from intra-transform faults and seamounts share a common mantle source with axial MORB, but represent smaller melt volumes tapped locally from areas lacking steady-state magma chambers and along-axis transport (Langmuir and Bender, 1984; Fornari et al., 1988; Batiza et al., 1990; Perfit et al., 1996; Reynolds and Langmuir, 1997; Niu et al., 2002; Sims et al., 2002). Thus, these melts that experience relatively small amount of differentiation and homogenization provide better estimates of the volatile contents of the heterogeneous upper mantle.

Here we report major, trace, and volatile element and Sr, Nd, and Pb isotopic composition of primitive (high MgO) glassy basalt samples from the NEPR off-axis seamounts, the Quebrada-Discovery-GoFar (QDG) transform

fault system, and the Macquarie Island. After filtering the volatile element data for secondary processes, we present a two-component (D-DMM and E-DMM) mantle melting-mixing model that successfully reproduces the trace and volatile element contents and isotopic composition of the EPR MORB and provides the volatile element budget of the Pacific upper mantle.

2. SAMPLES AND METHODS

The samples in this study are glassy basalts from the NEPR off-axis seamounts, the QDG transform fault system, and the Macquarie Island. Major elements, trace elements, and isotopic compositions of NEPR seamounts (Niu and Batiza, 1997; Niu et al., 2002) and Macquarie Island samples (Kamenetsky et al., 2000; Kamenetsky and Maas, 2002) have been previously analyzed and discussed, while those for the QDG transform fault samples are new data. Volatile elements for NEPR seamounts and QDG transform fault samples are new data, while those of Macquarie Island lavas (except for CO₂) have been previously analyzed and discussed (Kamenetsky et al., 2000). Except for the isotope data, all samples were reanalyzed for major, trace, and volatile elements on the same glass chips to avoid additional uncertainty of analyzing different elements in different glass chips or bulk rock and inter-laboratory bias, therefore, previously published data have not been used in this study.

Forty-seven dredges of young, glassy basalt were collected by the R/V Knorr from the QDG study area. The QDG transform fault system on the EPR (3–5°S) is composed of three different transform faults that offset the fast-spreading EPR (134–140 mm/yr) by approximately 400 km, with at least 8 intra-transform spreading centers varying in length from <10 to 93 km (Fig. 1a).

Seventy-four glassy basalt samples from the NEPR seamounts in this study were collected by the R/V Thomas Washington between 5 and 15°N latitude from near-ridge seamounts on the 1988 Raitt 02 expedition (Batiza et al., 1990; Batiza and Niu, 1992) (Fig. 1b). Seamounts are located on both the Pacific and Cocos plates. All samples were collected within 180 km from the ridge axis and 78% of them were collected within 50 km.

The fifty-three glassy basalt samples from the Macquarie Island in this study were collected by B. J. Griffin, M. J. Rubenach, J. L. Everard and B. Goscombe (Fig. 1c). Macquarie Island (54°30'S, 158°56'E) is an exposure of the Macquarie Ridge located about 1200 km south of New Zealand. The island was formed in the last 10 Myrs by transpression due to difference in motion of the Australia and Pacific plates (Johnson and Molnar, 1972; Ruff et al., 1989). The island is considered an uplifted section of oceanic crust and mantle formed at an oceanic spreading center (e.g. Varne et al., 1969, 2000; Christodoulou et al., 1984; Goscombe and Everard, 1998).

We mounted three to six chips of fresh, clean, naturally quenched glass from each sample in indium metal and polished them using diamond paste down to 0.25 μm. Multiple chips are used to determine the reproducibility of the measurements due to the analytical technique as well

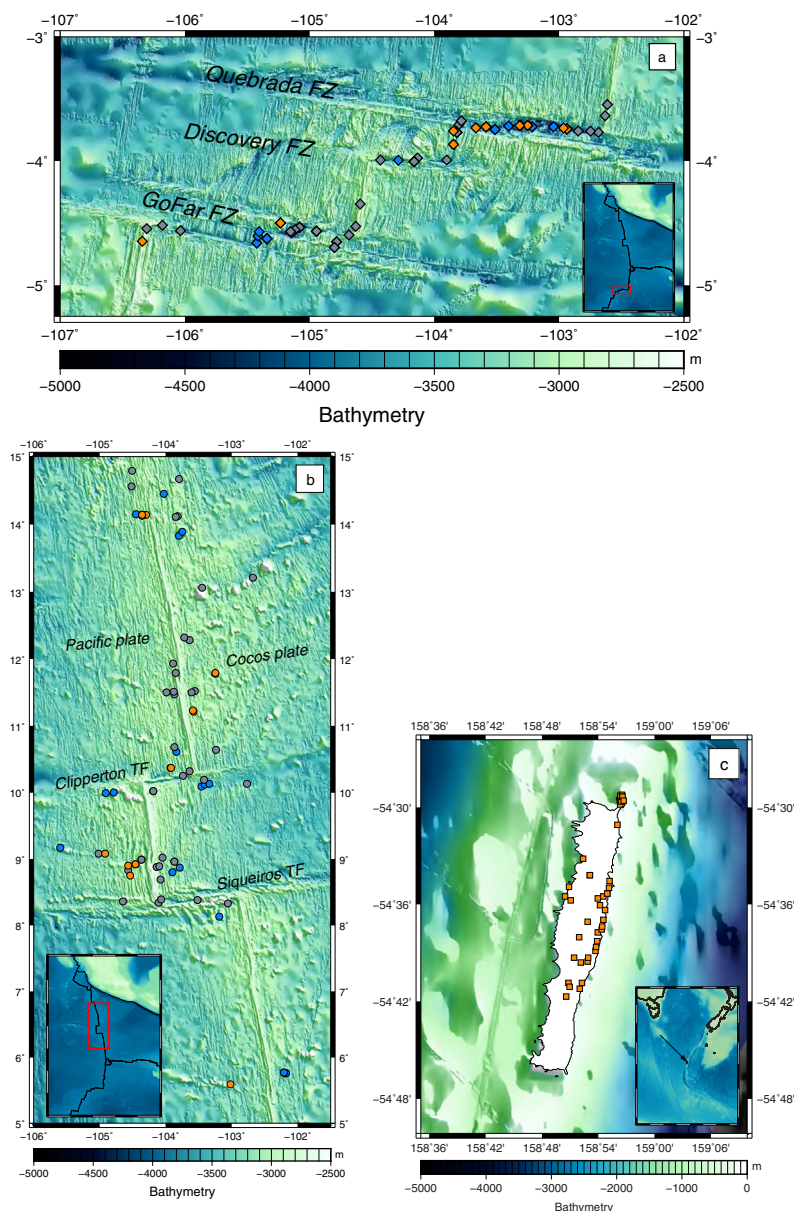


Fig. 1. (a) Bathymetric map of the QDG fracture zone system on the EPR (3–5°S) and (b) Northern EPR seamounts (5–15°N). (c) Macquarie Island located about 1200 km south of New Zealand. The symbols indicate sample locations and the colors indicate the degree of ITE enrichment; blue (DMORB, $\text{Th/La} \leq 0.035$), gray (NMORB, $0.035 < \text{Th/La} < 0.07$), and orange (EMORB, $\text{Th/La} \geq 0.07$).

as the natural variation in the glasses. The major, trace, and volatile element measurements were made on the same glass chip. Although major and trace element data from previous studies (Kamenetsky and Maas, 2002; Niu et al., 2002) were not used to avoid potential sample heterogeneity and lab bias, the previous published and new data are very consistent with each other. The analytical error (2σ SE) of each samples were calculated from the measurements of three to six glass chips per sample.

Major elements were analyzed using the Cameca SX-100 electron microprobe at Brown University using a 2 μm spot size. Analyses were performed using a 15 keV accelerating voltage and 10 nA beam current. Counting times for MgO , Al_2O_3 , MnO , P_2O_5 , and K_2O were 20 s for peak

and 10 s for background. All other major elements, Na_2O , SiO_2 , FeO^* , TiO_2 , and CaO , used 10 s peak and 5 s background counting times. Standard used were Smithsonian basalts VG-A99B (USNM 113498) and VG-2B (USNM 111240) (Jarosewich et al., 1980). Average analytical error (2σ SE) of the major element analyses were $<1\%$ for SiO_2 , Al_2O_3 , and MgO , $<2\%$ for FeO and CaO , $<3\%$ for Na_2O and TiO_2 ; for K_2O and P_2O_5 the errors were significantly larger (1–20% and 2–30% respectively). Major element analyses of the NEPR seamount samples are on average within 6% of those from Niu and Batiza (1997) for all elements except MnO and K_2O (within 13% of published analyses). Analyses of the Macquarie Island seamount samples are on average within 8% of those from

Kamenetsky et al. (2000) for all elements except MnO (within 18% of published analyses).

Trace elements were analyzed on the mounted glasses using the Quadrupole ICPMS X-Series II and 193 nm wavelength excimer Photon Machines Analyte G2 laser ablation system at Brown University. The standards used are BIR-1G, BHVO-2G, and BCR-2G, and the preferred values of elemental concentration from the GeoREM database (<http://georem.mpch-mainz.gwdg.de/>) were used. Analyses were conducted using a 160 μm spot size, the power output was 0.5 mJ, and repetition rate of 20 Hz. The background was measured for 30 s and then 20 s count time for pre-sputter and analysis. We used CaO as the internal standard. Average analytical error (2σ SE) of the samples was <6% for all elements. Trace element analyses of the NEPR seamount samples are on average within 20% of those from Niu and Batiza (1997). Analyses of the Macquarie Island seamount samples are on average within 10% of those from Kamenetsky et al. (2000) and Kamenetsky and Eggins (2012) for all elements, except for Li, V, Rb, Sr, Pb, and U (within 30% of published analyses). K concentrations of our samples measured using the electron microprobe and LA-ICP-MS are within 12% on average. For this study, the more precise K concentrations measured using LA-ICP-MS were used.

Volatile analyses for H_2O , CO_2 , F, Cl, and S were performed using the Cameca 6F ion probe at Carnegie Institution of Washington Department of Terrestrial Magnetism (for details on analytical techniques and standards see Hauri et al. (2002)). Each glass chip was analyzed using a 10–15 nA Cs^+ primary beam with a 300 s pre-sputter and 200 s counting time. Detection limits for these analyses are <0.5 ppm for F, S, Cl and ~ 4 to 5 ppm for H_2O , CO_2 . Average analytical precision (2σ SE) for volatile analyses was $\leq 5\%$ for all volatiles except Cl with 8%.

Sr and Nd isotopic measurements were made on a selected set of 27 QDG transform fault samples. Pb isotopic measurements were made on a selected set of 4 QDG transform fault samples. Basaltic glasses were handpicked, leached with cold 6 N HCl for 20 min, and then rinsed with Milli-Q water prior to dissolution. Nd, Sr, and Pb column chemistry were performed using Ln, Sr-spec, and AG1-X8 (100–200 mesh) resins respectively. Nd, Sr, and Pb isotopic compositions were measured on a Thermo Scientific NEPTUNE plus at Brown University. Sr and Nd were introduced to the mass spectrometer using a PFA 50 μl nebulizer coupled with a glass spray chamber, while Pb was introduced with an APEX introduction system. The mass spectrometer was equipped with an H-skimmer cone and H-sampler cone. The baseline measurement was taken at -0.5 amu. $^{143}\text{Nd}/^{144}\text{Nd}$ and $^{87}\text{Sr}/^{86}\text{Sr}$ are corrected for instrumental mass fractionation using $^{146}\text{Nd}/^{144}\text{Nd} = 0.7219$ and $^{88}\text{Sr}/^{86}\text{Sr} = 0.1194$ respectively. Pb solution was spiked with NBS SRM-997 Tl solution with a Pb/Tl = 4 to correct for the mass fractionation using exponential law with a $^{203}\text{Tl}/^{205}\text{Tl} = 0.418922$. $^{143}\text{Nd}/^{144}\text{Nd}$ and $^{87}\text{Sr}/^{86}\text{Sr}$ of samples are reported relative to La Jolla Nd Standard $^{143}\text{Nd}/^{144}\text{Nd} = 0.511850$ and NBS SRM 987 $^{87}\text{Sr}/^{86}\text{Sr} = 0.71024$ respectively. $^{206}\text{Pb}/^{204}\text{Pb}$, $^{207}\text{Pb}/^{204}\text{Pb}$, $^{208}\text{Pb}/^{204}\text{Pb}$ are reported relative to the NBS 981 Standard

$^{206}\text{Pb}/^{204}\text{Pb} = 16.9356$, $^{207}\text{Pb}/^{204}\text{Pb} = 15.4891$, and $^{208}\text{Pb}/^{204}\text{Pb} = 36.7006$ (Todd et al., 1996). The internal precision of the Sr and Nd analyses is 5–10 ppm and the external precision is 30 ppm for Sr (2σ , $n = 75$) and 25 ppm for Nd (2σ , $n = 104$). The internal precision of the Pb analysis is 20–45 ppm and the external precision is 45–80 ppm (2σ , $n = 75$). The Sr and Pb blanks were <50 pg, and Nd blanks were <30 pg. Sr, Nd, and Pb isotopic composition for a selection of NEPR seamounts and Macquarie Island basalts are from Niu et al. (2002), Kamenetsky and Maas (2002) respectively.

3. RESULTS

Major, trace, and volatile element concentrations of all samples are presented in Table S1, along with pressure of sample collection (P_{coll}), pressure of CO_2 – H_2O vapor saturation (P_{sat} calculated using the model of Dixon et al. (1995)) and Sr, Nd and Pb isotopic composition. The Macquarie Island samples were collected sub-aerially, however this does not correspond to their pressure of eruption since the eruption occurred under water prior to the tectonic uplift of the island (Duncan and Varne, 1988). Portner et al. (2010) estimated the paleo-ridge depth between 2000 to 3500 m.b.s.l. based on the benthic foraminifera from inter- and intra-pillow calcareous oozes (Quilty et al., 2008). Here we use an average of their estimated eruption pressure and assume a P_{coll} for Macquarie Island samples of 275 ± 75 bars.

The composition of the samples ranges from tholeiitic to alkalic basalts (Fig. 2a and S1). Most of the samples in this study have $\text{MgO} > 6.0$ wt% with a total range of 3.3 to 9.8 wt%. The variation in major element composition of the samples with decreasing MgO generally follows a typical MORB differentiation trend (Fig. S2a–f, description of the model LLDs are given in Section 4.4). Differences in major element content such as FeOt and Al_2O_3 for a given MgO are partly due to the large range in H_2O concentration (0.05–1.62 wt%) in our samples leading to variable delay of plagioclase saturation (e.g. Sinton and Fryer, 1987; Asimow and Langmuir, 2003). The samples with high H_2O content tend to have higher Al_2O_3 and lower FeOt than samples with low H_2O content for a given MgO due to greater delay of plagioclase crystallization. The differences in major element contents of our samples for a given MgO also reflect the compositional variation of parental melt potentially due to variable pressure and temperatures of melt generation, mantle source composition, and mixing between melts.

We use the Th/La ratio of our samples as a proxy for the long-term geochemical enrichment/depletion of the mantle source instead of $(\text{La}/\text{Sm})_{\text{N}}$ and $\text{K}_2\text{O}/\text{TiO}_2$, which are more susceptible to fractionation at small degrees of melting. Based on the Th/La ratio, the samples are divided into three groups, EMORB ($\text{Th}/\text{La} \geq 0.07$), NMORB ($0.035 < \text{Th}/\text{La} < 0.07$), and DMORB ($\text{Th}/\text{La} \leq 0.035$) (Fig. 2a and b). Although not exact, the rough boundary between the three groups in terms of $(\text{La}/\text{Sm})_{\text{N}}$ and $\text{K}_2\text{O}/\text{TiO}_2$ ratios are as follows; EMORB ($(\text{La}/\text{Sm})_{\text{N}} \geq 1$ and $\text{K}_2\text{O}/\text{TiO}_2 \geq 0.15$), NMORB ($0.5 < (\text{La}/\text{Sm})_{\text{N}} < 1$ and

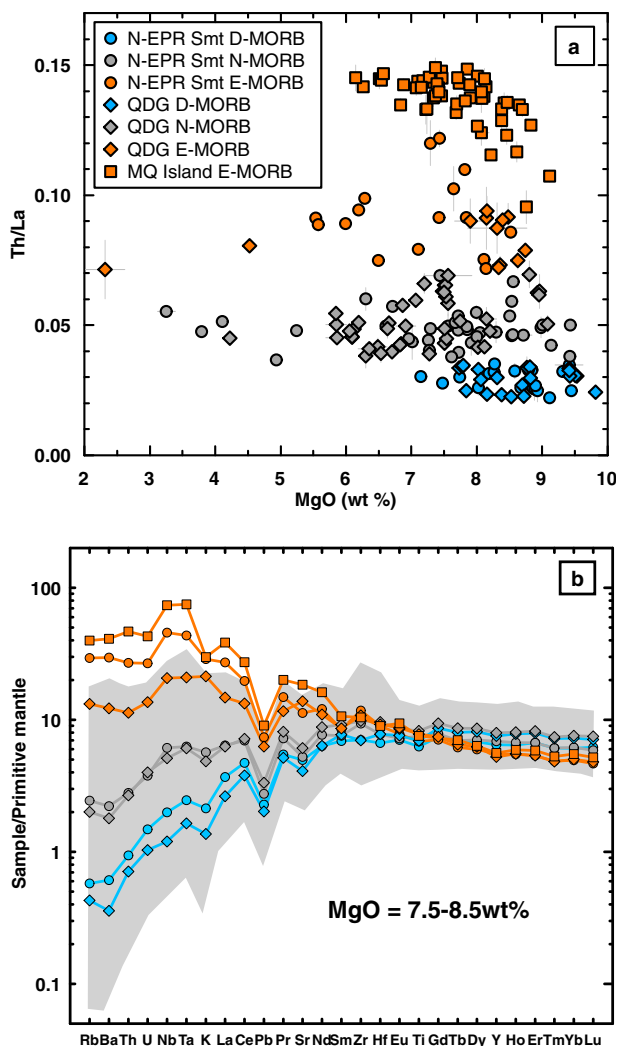


Fig. 2. (a) Th/La versus MgO for the samples. Most of the samples have MgO > 6.0 wt%. Samples are separated into three groups DMORB (blue, Th/La \leq 0.035), NMORB (gray, 0.035 < Th/La < 0.07), and EMORB (orange, Th/La \geq 0.07). Error bars are 2σ SE. (b) Primitive mantle normalized trace element diagram of representative samples from each location and enrichment group. All plotted samples have between 7.5 and 8.5 wt% MgO. The grey field is the entire range of trace element abundance observed in a compilation of EPR axial MORB Gale et al. (2013), Mallick et al. (in revision) that have greater than 6 wt% MgO. Primitive mantle composition is from McDonough and Sun (1995).

$0.05 < K_2O/TiO_2 < 0.15$), and DMORB ($(La/Sm)_N \leq 0.5$ and $K_2O/TiO_2 \leq 0.05$). For simplicity, from now on we will label the mantle source of NMORB, DMORB and EMORB as DMM, D-DMM, and E-DMM respectively.

The isotopic composition of the samples covers a large portion of the total range observed in EPR MORB (Fig. 3a and b). The EMORB samples tend to plot towards radiogenic Sr and Pb isotopic composition, and DMORB samples tend to plot towards unradiogenic Sr and Pb isotopic composition, suggesting that the Th/La of the samples can be used as a first order proxy for long-term ITE enrichment in the mantle source. However, Th/La is not always a

good proxy for long-term mantle ITE enrichment since there are samples covering the whole range in Th/La with the isotopic composition of EMORB (Fig. 3c). This may suggest that these isotopically enriched DMORB and NMORB samples are derived from an E-DMM source that experienced recent depletion by fractional melting, where the incremental fractional melts did not completely aggregate before eruption.

4. THE EFFECT OF SECONDARY PROCESSES ON VOLATILES

Previous studies have shown that volatile elements have bulk distribution coefficients similar to refractory ITEs during mantle melting: CO₂ has a bulk partition coefficient similar to Nb–Th–Ba, F to Nd–P, Cl to K–Nb, S to heavy REEs such as Dy, and H₂O to Ce–La (Michael, 1988, 1995; Dixon, 1997; Michael and Cornell, 1998; Danyushevsky et al., 2000; Saal et al., 2002; Workman et al., 2006; Rosenthal et al., 2015). A recent experimental study by Rosenthal et al. (2015) show that CO₂ behave more similar to Ba than Nb and F more similar to La than Nd. F/La is not used in this paper since the negative correlation between F/La and La/Sm might suggest a more incompatible behavior of La compared to F. The most commonly used ratios CO₂/Nb, H₂O/Ce, Cl/K, Cl/Nb, F/Nd, and S/Dy along with CO₂/Ba and Cl/Ba are used in this paper. These volatile to ITE ratios will change if the samples experience secondary processes that only affect the volatile elements, such as degassing, assimilation of hydrothermally altered materials, and sulfide saturation. Fractional crystallization may affect the volatile to ITE ratios in magmas depending on the extent of fractional crystallization and the difference in incompatibility of the elements in the crystallizing mineral. Once those processes are accounted for and the samples have been filtered for those processes, the volatile to trace element ratios can be used to determine the mantle source volatile abundances considering the small fractionation of these ratios during mantle melting.

4.1. Degassing: CO₂–H₂O saturation and P_{sat} versus P_{coll}

At typical submarine pressures of eruption (>50 bars), H₂O, Cl, F and S are relatively soluble in basaltic magma such that the effect of degassing is considered relatively small (Schilling et al., 1980; Wallace and Carmichael, 1992; Carroll and Webster, 1994; Michael, 1995; Michael and Cornell, 1998; Danyushevsky et al., 2000; Edmonds et al., 2009; Lesne et al., 2011). In contrast, the low solubility of CO₂ in basaltic magma results in significant CO₂ degassing during magma ascent and flow on the ocean floor (Dixon and Stolper, 1995; Soule et al., 2012). As a result, almost all MORB lavas are saturated or supersaturated with a CO₂–H₂O rich vapor phase upon eruption.

The measured CO₂ and H₂O contents of the samples were used to calculate CO₂–H₂O saturation pressures (P_{sat}) using the model of Dixon et al. (1995) (Fig. 4a). The comparison between P_{sat} and pressure of sample collection (P_{coll}) can be used to assess saturation/super-saturation/under-saturation of the samples in a CO₂–H₂O vapor phase

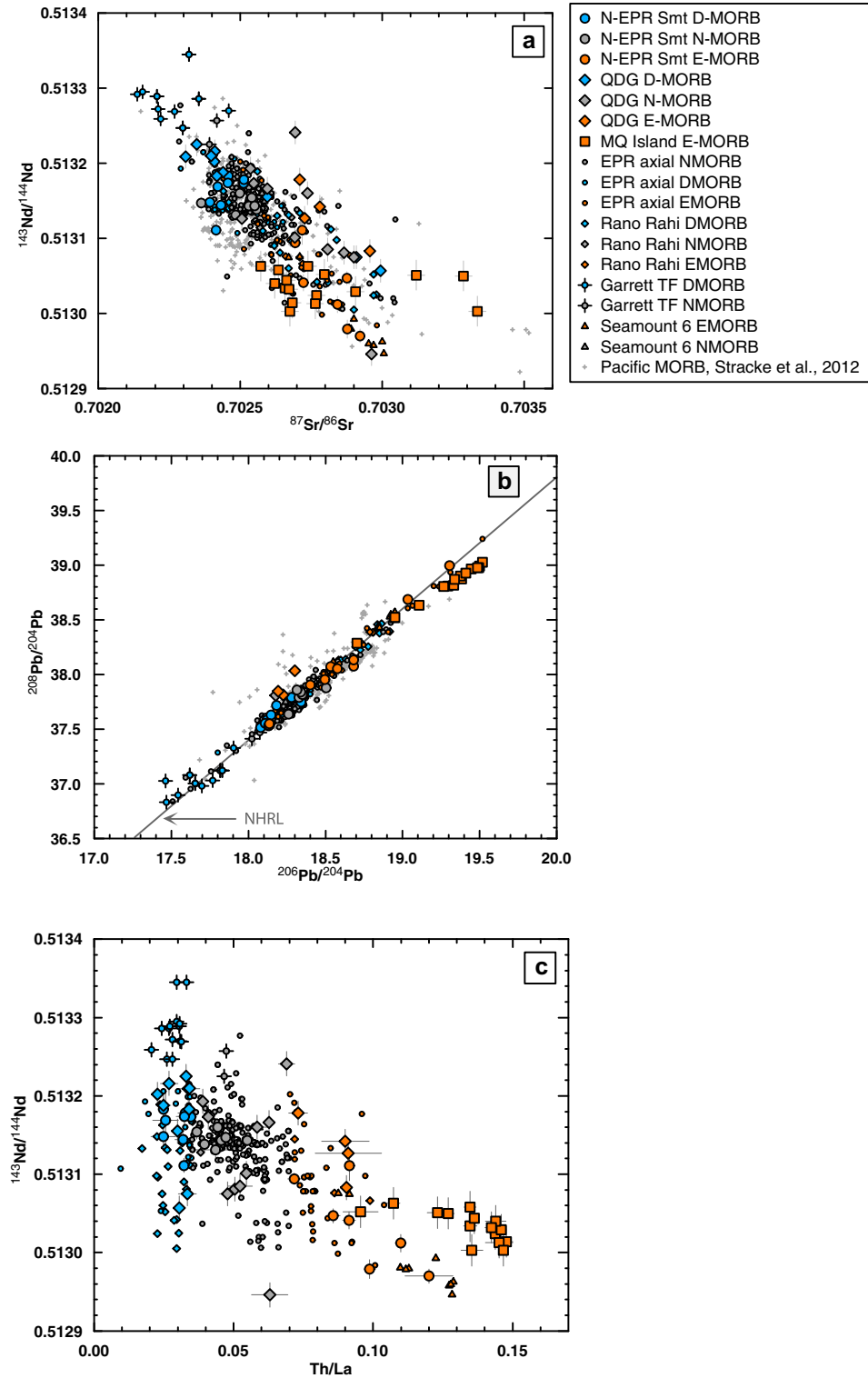


Fig. 3. (a) $^{143}\text{Nd}/^{144}\text{Nd}$ versus $^{87}\text{Sr}/^{86}\text{Sr}$, (b) $^{208}\text{Pb}/^{204}\text{Pb}$ versus $^{206}\text{Pb}/^{204}\text{Pb}$ and (c) $^{143}\text{Nd}/^{144}\text{Nd}$ versus Th/La ratios for the samples in this study. In (a), (b), and (c), the small circles are EPR axial MORB Gale et al. (2013), Mallick et al. (in revision), small diamonds are Rano Rahi seamounts Hall et al. (2006), small triangles are Seamount 6 Brandl et al. (2012), and the circle with cross are Garrett transform fault Wendt et al. (1999). The isotopic composition for NEPR seamounts and Macquarie Island samples are from Niu et al. (2002), Kamenetsky and Maas (2002) respectively. In (a) and (b) we also added the Pacific MORB data from a compilation by Stracke (2012). Error bars are 2σ for isotopic composition and 2σ SE for the Th/La ratios.

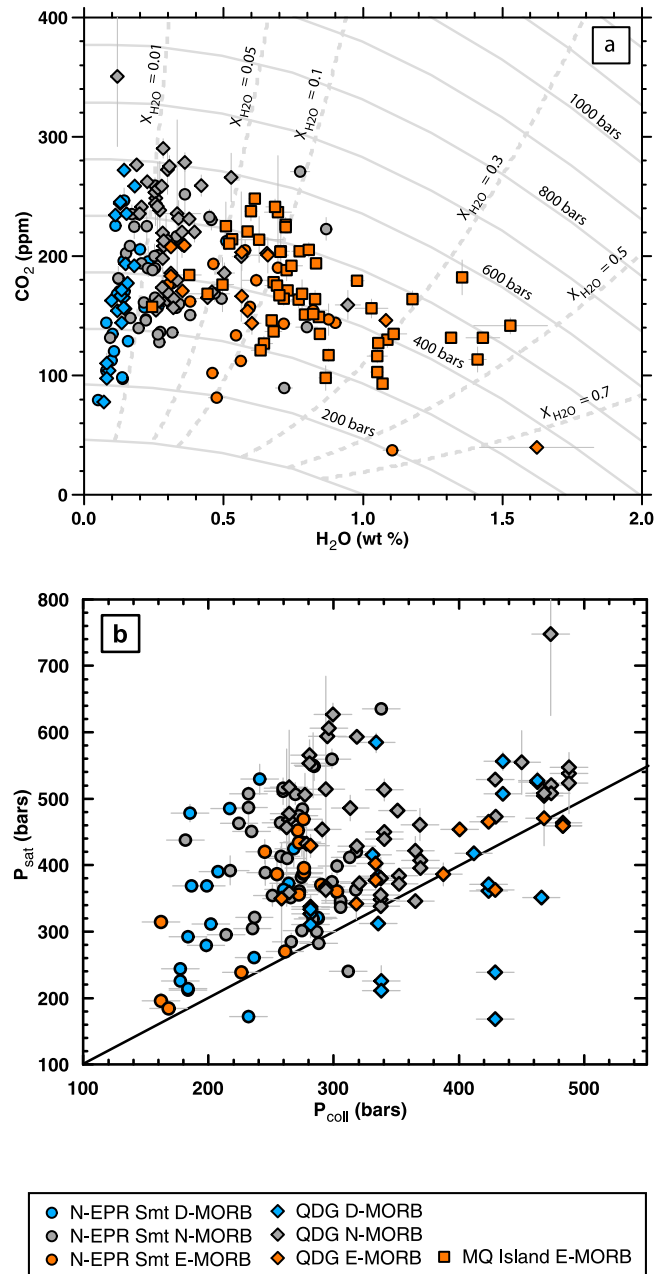


Fig. 4. (a) CO₂ versus H₂O for the samples and their pressure of H₂O–CO₂ saturation. Isobars (solid lines) and isopleth of mole fraction of H₂O in the vapor phase (X_{H₂O}) (dashed lines) determined from the solubility model of Dixon et al. (1995). Error bars are 2σ SE. (b) Pressure of H₂O–CO₂ saturation (P_{sat}) versus pressure of collection (P_{coll}) for the samples. P_{sat} is calculated from the solubility model of Dixon et al. (1995). The black line is a 1:1 line. P_{coll} for Macquarie Island samples (not shown in Fig. 4b) is 275 ± 75 bars, which is the estimated average paleo-ridge based on the benthic foraminifera from inter- and intra-pillow calcareous oozes (Quilty et al., 2008; Portner et al., 2010). Note that the lowest P_{sat} recorded in the Macquarie Island samples (273.5 bars) matches well with the estimated P_{coll}. Eight depleted samples plot below the 1:1 line outside of the error bars, indicating they are H₂O–CO₂ undersaturated. Sample D42A2 was not considered undersaturated since it is very close to the 1:1 line (8 bars). Samples that plot on the line are saturated, while those plotting above the line are supersaturated in CO₂. Error bars for P_{sat} are based on the 2σ SE of the measured CO₂ and H₂O concentrations in the glasses. Error bars for P_{coll} are ±15 bars.

as well as the velocity of magma ascent relative to the magma-vapor equilibration rate. Samples with P_{sat} higher than P_{coll} are super-saturated in a CO₂–H₂O vapor phase (Fig. 4b), which indicates that the magma ascent rate was too fast to allow magma-vapor equilibration (Dixon and

Stolper, 1995; Dixon et al., 1995). Samples with P_{sat} equal to P_{coll} are saturated in a CO₂–H₂O vapor phase, which indicates that the magma ascent rate was slow, allowing the magma-vapor equilibration. Samples with P_{sat} lower than P_{coll} indicates that the lavas are undersaturated in

the CO₂–H₂O vapor phase, assuming that the lavas did not erupt at a shallower depth reaching saturation and subsequently flowed down-slope. 95% of the samples are either saturated or super saturated with a CO₂–H₂O vapor phase at the P_{coll}, therefore most likely they experienced CO₂–H₂O degassing. Eight DMORB samples, most of which are from the QDG transform fault system, appear to be undersaturated in CO₂–H₂O vapor phase (Fig. 4b). The vapor undersaturation of these DMORB samples is due to their low volatile contents and their deep eruption depth (avg. P_{coll} = 385 ± 77). Five of the eight samples have depth of saturation shallower than 2400 m.b.s.l. (P_{sat} lower than 240 bars), which is the shallowest bathymetric depth for the areas of sample collection. Therefore, these five samples could not have erupted at a shallower depth (<2400 m.b.s.l.) and subsequently flowed down-slope. Thus, these five samples are undersaturated in a CO₂–H₂O vapor phase and their CO₂ content have not been affected by degassing. In contrast, three of the eight samples have depth of saturation 3500–3700 m.b.s.l. (P_{sat} of 350–370 bars), which is a common bathymetric depth that is found in the vicinity (<10 km) of the area of samples collection. Although we cannot confidently rule out that these three samples could have erupted at shallower depth and flowed down-slope, we consider that the most likely explanation is that they are undersaturated in a CO₂–H₂O vapor phase given their high CO₂/Nb ratios (244 ± 26) similar to those measured in the other five CO₂–H₂O undersaturated samples and in the Siqueiros melt inclusions (Saal et al., 2002). In contrast, one NMORB sample from the NEPR seamount and one EMORB sample from the QDG transform fault system with P_{sat} below the P_{coll} (Fig. 4b) have very low CO₂/Nb (<20) suggesting significant CO₂ degassing. Therefore, we assumed they were erupted at shallow depth and transported down-slope.

Although solubility of H₂O is higher than CO₂ in basaltic magmas, degassing may affect the H₂O content of the samples with high mole fraction of H₂O in the vapor phase (X_{H₂O}) such as the Macquarie Island samples. We used the CO₂–H₂O degassing program (Solex) from Witham et al. (2012) to assess the effect of degassing on the H₂O content of the samples. To estimate the effect of degassing on the H₂O content of the lavas, we assume the initial volatile content to be similar to those of the Macquarie Island samples 47963 with 1.41 wt% H₂O and an 7.32 wt% CO₂ (using a CO₂/Ba of 134 and the Ba content 546 ppm of the sample 47963, refer to Section 5.3 for an explanation on the CO₂/Ba ratio) at a temperature of 1300 °C. According to the model, the melt after ~99.8% degassing of its CO₂ (128 ppm CO₂) still retains ~97.6% of its H₂O (1.38 wt%) assuming open system degassing. In contrast, closed system degassing can lead to 72.9% loss of H₂O (final water content of 0.38 wt%), but the volume fraction of exsolved gas in such magma (79%) exceeds the critical fraction for magma fragmentation of 75% (Sparks, 1978; Wilson et al., 1980). We do not believe that the samples represent close system degassing because (1) although some of the Macquarie Island samples are hyaloclastites and others are glass pillow rims (Kamenetsky et al., 2000), we observe a strong correlation between H₂O and Ce (similar H₂O/Ce

average and 2 sigma) in all the sample regardless of the eruption mechanism. (2) There is no correlation between the H₂O content and hydrogen isotopic composition of the samples (Bindeman et al., 2012). (3) Kamenetsky et al. (2002) analyzed the gas bubbles within the glasses using laser Raman spectroscopy and found that they had a CO₂ dominant composition. (4) Although some hyaloclastites in Macquarie Island formed by fragmentation due to explosive eruption, they formed mainly due to thermal shock granulation (Dickinson et al., 2009; Portner et al., 2010). Therefore, we conclude that degassing occurred under open system, and it had minimal effect on the H₂O content of our samples.

4.2. Chlorine and water: contamination process

Here we use Cl/K ratio to track shallow level processes such as assimilation of hydrothermal circulation of seawater and seawater brines (Michael and Cornell, 1998; Kent et al., 1999, 2002; Lassiter et al., 2002; Simons et al., 2002; Stroncik and Haase, 2004; le Roux et al., 2006). Michael and Cornell (1998) define uncontaminated Cl/K ratios of 0.01–0.02 for NMORB and 0.08 for EMORB. When Cl/K ratios are compared to Th/La, the majority of the samples follow two distinct trends (Fig. 5a): One with a large range of Cl/K at roughly constant Th/La ratios in DMORB and NMORB samples indicative of assimilation of seawater or seawater brines (Michael and Cornell, 1998; Kent et al., 1999; le Roux et al., 2006). This trend is mostly defined by the DMORB and NMORB samples because they are the most susceptible samples to Cl contamination due to their low Cl concentration. The second trend is defined by the correlation between Cl/K and the extent of ITE enrichment. This trend includes as an extreme, the EMORB samples from Macquarie Island that consistently plots at a Cl/K of ~0.09 slightly above the mantle limit of 0.08 proposed by Michael and Cornell (1998) for the EMORB (Fig. 5b). This relatively constant Cl/K of ~0.09 is consistent with the measurement of the same sample set by Kendrick et al. (2012), Kamenetsky and Eggins (2012). In contrast, EMORB samples with Cl/K > 0.1 are potentially contaminated since they have a considerably higher Cl/K compared to the rest of the EMORB samples. Therefore EMORB samples including the Macquarie Island samples with Cl/K < 0.1 are most likely not contaminated by assimilation of seawater or seawater brines, while the EMORB samples with Cl/K > 0.1 are potentially contaminated.

In addition to Cl, circulating hydrothermal fluids may also affect H₂O contents in the basalts, and Fig. 6 shows calculated effects of various contaminants on the Cl/K and H₂O/Ce ratios of a DMORB sample (D42A from QDG TF). The samples that have high Cl/K (>0.1) can be explained by addition of up to 0.1–0.2% of a 15–50 wt % NaCl brine. Contamination by high salinity brine is a reasonable explanation for the high Cl/K, which increases this ratio much more than H₂O/Ce during contamination. It is possible to create very saline brines along the EPR where the hydrothermal circulation can occur at depths coincident with the top of the axial magma chamber along

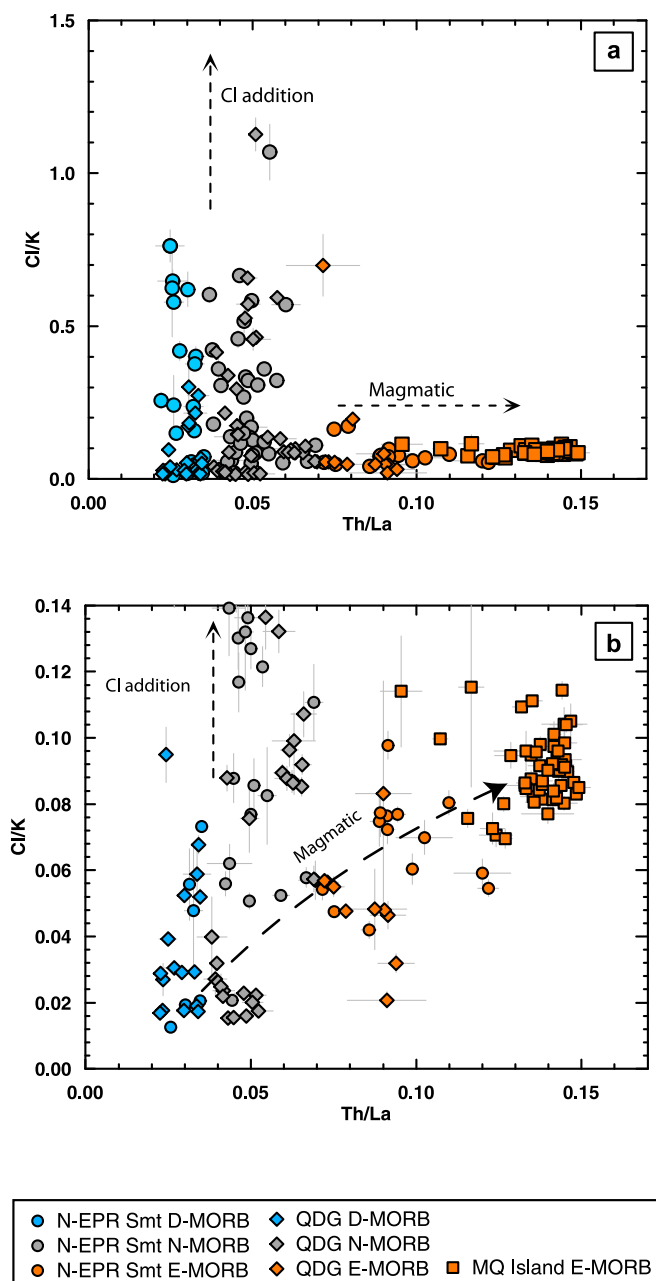


Fig. 5. (a) Cl/K versus Th/La ratios for the samples in this study. (b) Cl/K versus Th/La ratios for samples with Cl/K < 0.14. Two primary trends can be distinguished: One with a large range of Cl/K at roughly constant Th/La representing Cl addition (the assimilation of seawater and seawater brines) and a second defined by a correlation between Cl/K and indicators of magmatic ITE enrichment. Error bars are 2σ SE.

the ridge axis at ~ 4000 m.b.s.l (le Roux et al., 2006). This corresponds to a depth of 1200 meters into the oceanic crust, or a pressure of 620 bars (assuming 2800 m ocean depth, water density of 1000 kg/m^3 , and crust density of 2890 kg/m^3 (Carlson and Raskin, 1984)), which matches well with the highest P_{sat} recorded in our samples except for one NMORB sample that erupted at a deeper depth (Fig. 4b). At these pressures and temperatures, supercritical two-phase separation of seawater may occur, producing a vapor phase and dense, highly saline brine up to 50 wt% NaCl (Kelley and Delaney, 1987; Vanko, 1988).

In terms of seawater assimilation, the DMORB and NMORB samples with high $\text{H}_2\text{O}/\text{Ce}$ ratios often have high Cl/K (Fig. 6 inset), suggesting that high $\text{H}_2\text{O}/\text{Ce}$ ratios of DMORB and NMORB samples may be due to assimilation of seawater. In contrast, the EMORB samples with the highest $\text{H}_2\text{O}/\text{Ce}$ ratios have a relatively low Cl/K (Fig. 6 inset), which is inconsistent with the idea that assimilation of seawater is causing the high $\text{H}_2\text{O}/\text{Ce}$ ratios in these samples.

The $\text{H}_2\text{O}/\text{Ce}$ ratio of our unfiltered samples range from average Pacific MORB value of 150 (Dixon et al., 2002) up

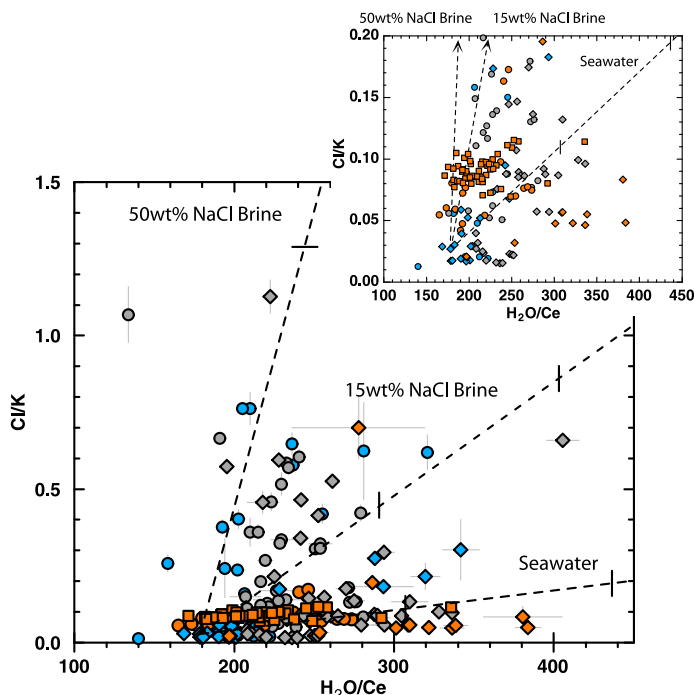


Fig. 6. Cl/K versus H_2O/Ce ratios for the samples in this study. The dashed lines represent the effects of seawater and NaCl brines of different concentrations contaminating a DMORB sample (D42A from QDG TF). Tick marks on the dashed lines shows the effect of 0.1 wt% assimilation of the contaminant. The compositions of the contaminants were taken from (Kent et al., 1999; le Roux et al., 2006). The inset shows samples with $Cl/K < 0.2$. Error bars are 2σ SE.

to ~ 400 (Fig. 7a). We filter DMORB and NMORB samples with Cl/K ratio higher than 0.04 and 0.06 respectively, since it is later shown in Section 5.5.2 that samples with Cl/K as high as these values can be produced by magma mixing processes rather than assimilation of hydrothermal material. As discussed earlier in this section, EMORB samples with Cl/K ratio higher than 0.1 are also filtered for contamination. After filtering the samples for contamination using the Cl/K ratios, it is apparent that a large fraction of the measured range in H_2O/Ce of DMORB and NMORB samples is due to contamination by hydrothermal circulation of seawater and seawater brine, but the range in H_2O/Ce of the EMORB samples persists (Fig. 7b).

4.3. Sulfur and sulfide saturation

The sulfur content at sulfide saturation (SCSS) of a melt depends on melt and sulfide compositions, fO_2 , fS_2 , temperature, and pressure (Wallace and Carmichael, 1992; Carroll and Webster, 1994; Mavrogenes and O'Neill, 1999; O'Neill and Mavrogenes, 2002; Liu et al., 2007; Fortin et al., 2015; Wykes et al., 2015). We calculated the SCSS of the samples using the sulfide saturation model of Fortin et al. (2015) and compared the results with the measured sulfur content (Fig. 8). We used the pressure of CO_2 – H_2O saturation (Section 4.1), and the melt temperature was estimated based on the mole fractions of MgO and Al_2O_3 in the melt (Wallace and Carmichael, 1992) corrected for the effect of H_2O on the liquidus temperature (Medard and Grove, 2008). More than half of the samples (57%) are sulfide undersaturated

according to the sulfide saturation model of Fortin et al. (2015). We have also calculated the SCSS using the model of Mavrogenes and O'Neill (1999) in conjunction with the model of O'Neill and Mavrogenes (2002), in which case all of our samples are sulfide undersaturated. These results do not change even if we calculate the SCSS of our samples using the pressure at the bottom of the oceanic crust of 1800 bars (assuming a 6.4 km thick oceanic crust and a crustal density of 2890 kg m^{-3} (Carlson and Raskin, 1984)). Although these results may seem at odds with the observation of sulfide blebs in MORB, these sulfides may not be in equilibrium with the melt: they may be products of quench effects, magma mixing, crustal assimilation, etc. If this was the case, despite the observation of sulfide blebs in MORB, a majority of our samples may indeed be sulfide undersaturated.

Alternatively the model of Fortin et al. (2015) might be overestimating the SCSS of our samples. The strong partitioning of Cu and Ni found in sulfides in MORB (Patten et al., 2013) may reduce the $aFeS_{(sulfide)}$ and stabilize sulfides in melts at lower SCSS compared to pure $FeS_{(sulfide)}$ (Ariskin et al., 2013; Wykes et al., 2015). Therefore, SCSS models based on parameterization that do not consider Cu and Ni contents in sulfide may overestimate the SCSS of MORB samples. The $aFeS_{(sulfide)}$ in sulfides found in MORB samples (Patten et al., 2013) calculated assuming the activity coefficient of $FeS_{(sulfide)}$ is approximately 1.0 following Kiseeva and Wood (2015), ranges from 0.7 to 0.8. Although an $aFeS_{(sulfide)}$ of 0.7–0.8 decreases the SCSS for our samples calculated using the model of Mavrogenes and O'Neill (1999) in conjunction with O'Neill and

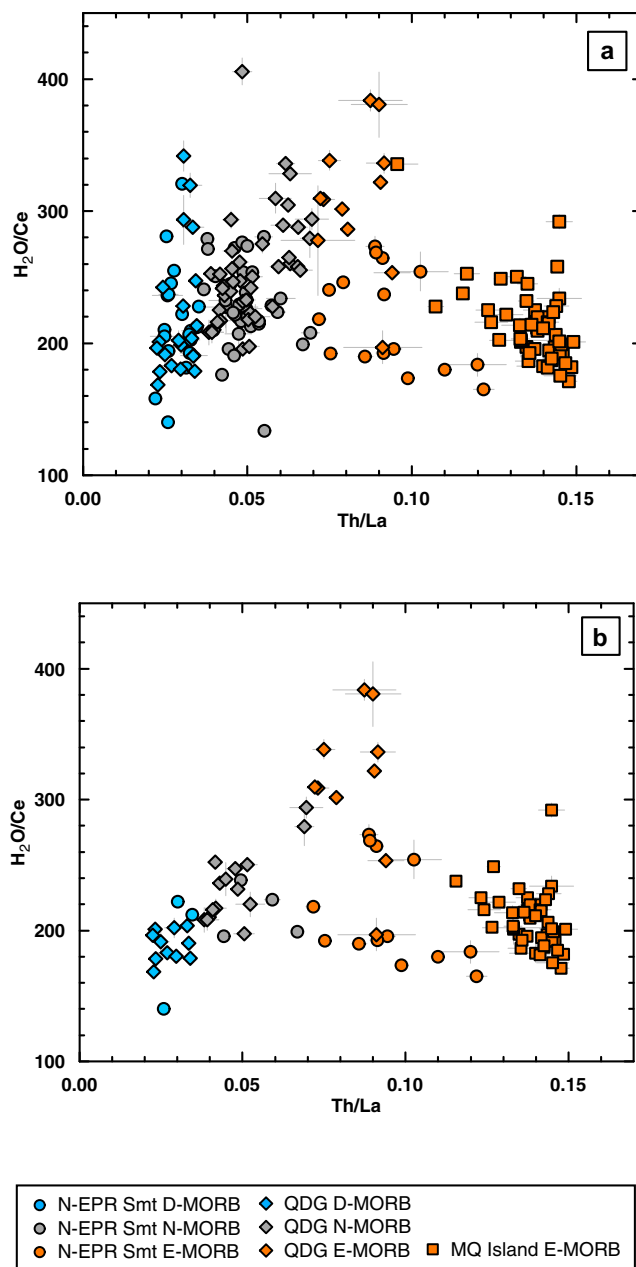


Fig. 7. (a). H_2O/Ce versus Th/La ratios for all the samples. (b). H_2O/Ce versus Th/La ratios for samples uncontaminated by hydrothermal altered materials. DMORB samples with $Cl/K > 0.04$, NMORB samples with $Cl/K > 0.06$, and EMORB samples with $Cl/K > 0.1$ were filtered from the data set. We used Cl/K limits slightly higher than those proposed by Michael and Cornell (1998) for the D- and N-MORB samples, since we show in Section 5.5.2 that values as high $Cl/K \sim 0.04$, for DMORB and ~ 0.06 for NMORB can be produced by the two component mantle melting mixing model and they may not necessarily indicate assimilation of hydrothermally altered material.

Mavrogenes (2002), they are still high compared to the measured sulfur content, suggesting that all our samples are sulfide undersaturated.

Despite this possibility that all our samples are sulfide undersaturated, we used the model of Fortin et al. (2015) to make conservative estimates of the SCSS of our samples given the observation of sulfide blebs in most MORB. After filtering our samples for sulfide saturation, the average S/Dy of the sulfide undersaturated DMORB, NMORB,

and EMORB samples are 259 ± 64 (2σ), 247 ± 47 , and 189 ± 58 respectively (Fig. 9). Although there is significant overlap between groups, the more ITE enriched samples tend to have lower S/Dy ratio. In particular the average S/Dy of the most ITE enriched samples (Macquarie Island samples) is 179 ± 37 (2σ). This trend of decreasing S/Dy with ITE enrichment is opposite of that expected from the higher modal abundance of garnet in the mantle during deeper melting of the E-DMM.

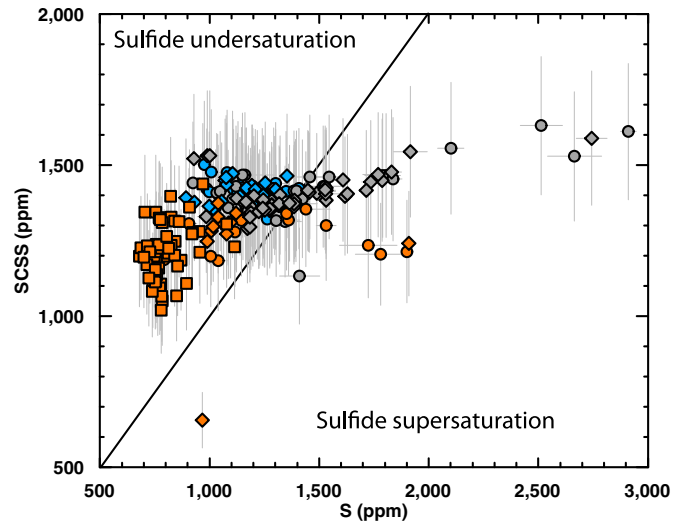


Fig. 8. Sulfur content at sulfide saturation (SCSS) versus measured sulfur for the samples. The SCSS was calculated using the sulfide saturation model of Fortin et al. (2015). The solid line is the 1:1 line. The majority of the samples plot to the left of the 1:1 line indicating that they are sulfide undersaturated. Error bars of the sulfur content are 2σ SE. Error bars of the SCSS ($\pm 14\%$) for the calculated SCSS using the model of Fortin et al. (2015) are based on the average deviation of the calculated SCSS from the measured S content in the experiments with basaltic compositions and S contents similar to our samples (1000–1700 ppm).

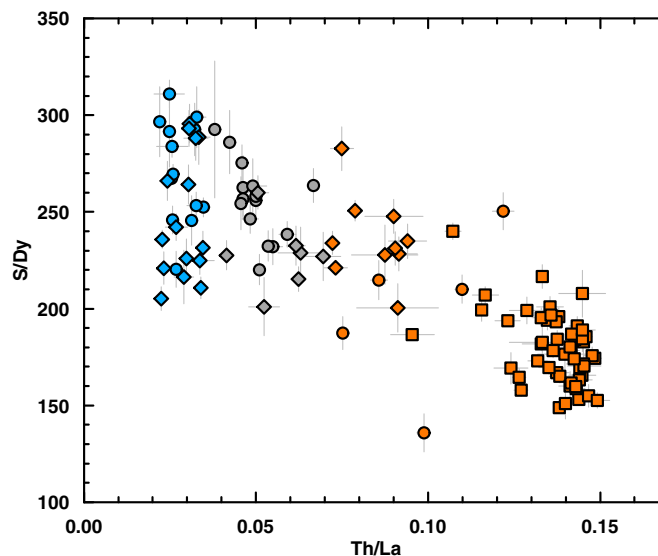


Fig. 9. S/Dy versus Th/La for the sulfide undersaturated samples based on the SCSS model of Fortin et al. (2015). The average S/Dy of the sulfide undersaturated DMORB, NMORB, and EMORB samples are 259 ± 64 , 247 ± 47 , and 189 ± 58 respectively, similar to the range of 225 ± 49 observed in depleted Siqueiros melt inclusions Saal et al. (2002).

4.4. Fractional crystallization

Fractional crystallization is one of the processes that could potentially fractionate the volatile to trace elements ratios in a melt. To estimate the magnitude of this fractionation, the MELTS program (Ghiorso and Sack, 1995; Asimow and Ghiorso, 1998) was used to model an

isobaric fractional crystallization of model primitive DMORB and EMORB. For detailed explanation of the model LLDs, refer to the caption of Fig. S2. The major element composition of the model DMORB and EMORB LLDs generally follow the trends defined by our DMORB and EMORB samples showing the validity of this model in predicting the effect of fractional crystallization on the

volatile to trace element ratios of our samples (Fig. S2a–f). However, the H₂O-rich Macquarie Island EMORB samples have higher Al₂O₃ and lower FeO for a given MgO compared to the model EMORB LLD suggesting a smaller amount of plagioclase crystallization in these samples due to their high H₂O contents of 1–1.5 wt%. We show that an alternative EMORB LLD using the same initial major element composition, but with high H₂O content (1.5 wt%), reproduces the Macquarie samples (Fig. S2a–f).

The mineral-melt (except plagioclase-melt) partition coefficients for the volatile elements are from Hauri et al. (2006) (H₂O, F, and S) and Rosenthal et al. (2015) (CO₂) and those for the trace elements are from Kelemen et al. (2003). The incompatibility of Cl has been estimated to be similar to Ba and Rb (Schilling et al., 1980), thus the Ba partition coefficient from Kelemen et al. (2003) was used to simulate the behavior of Cl during fractional crystallization. Furthermore CO₂ and Cl abundances correlate positively in the vapor undersaturated Siqueiros melt inclusion, which suggests a similarly incompatible behavior of CO₂ and Cl (Saal et al., 2002). Recent experimental results of Rosenthal et al. (2015) has shown that the bulk partition coefficient of CO₂ is slightly higher than Ba and more incompatible than Nb. For the CO₂ partition coefficient, experimental results of Rosenthal et al. (2015) are used. The plagioclase-melt partition coefficients for H₂O is from Johnson (2006) and those for the trace elements are from Blundy and Wood (1994). The experimental results of Bindeman et al. (1998) suggests the relatively compatible behavior of F and Cl in plagioclase, but even using their minimum partition coefficient would cause decreasing F/Nd and Cl/K ratios with decreasing MgO during plagioclase fractionation, which is not observed in our samples. Therefore, F and Cl, and S are assumed to be perfectly incompatible in plagioclase due to lack of reliable experimental data on their partitioning between plagioclase and basaltic melt.

The change in volatile to trace element ratios relative to the initial ratios (average ratios of all the DMORB samples and all the EMORB samples) after fractional crystallization to a MgO content in the melt of 5 wt% are ~11% for H₂O/Ce, ~18% for DMORB and 11% for EMORB for CO₂/Ba and Cl/Ba, 10% for F/Nd and 15% for S/Dy (Fig. S2g–m). The variation in CO₂/Ba and Cl/Ba ratios during fractional crystallization is noticeable due to the effect plagioclase and its dependence on the water content of the melt, but note that equivalent ratios such as CO₂/Nb, Cl/K, and Cl/Nb remain essentially constant. Thus, the use of CO₂/Ba and Cl/Ba may require a careful evaluation of fractional crystallization. Although non-trivial, the fractionation of H₂O/Ce, CO₂/Ba, Cl/Ba, F/Nd, and S/Dy due to fractional crystallization is within the range of the analytical error for the measured ratios and the amount of fractionation listed above should be considered as the maximum fractionation of the ratios, since 93% of our samples have MgO content between 6 and 10 wt%. Therefore, the magnitudes of the fractionation of volatile to ITE ratios are not large enough to alter our interpretation of the data.

5. DISCUSSION

5.1. The enriched component in the Pacific upper mantle (peridotite versus pyroxenite)

It is important to present some evidence that might help establish the lithology of the E-DMM. The origin of the enriched components in the source of MORB has been a topic of debate (e.g. Hirschmann and Stolper, 1996; Niu et al., 2002; Sobolev et al., 2007). Three samples from QDG TF have a very similar enriched isotopic composition indicative of derivation from an E-DMM, while their trace element pattern ranges from EMORB to DMORB (Fig. 10a and b). The range in trace element enrichment of these samples at an essentially constant isotopic composition suggests that the E-DMM melted incrementally without the aggregation of the different melt fractions, as expected at an intra-transform spreading settings (Morgan and Forsyth, 1988; Reynolds and Langmuir, 1997), producing melts with relatively constant isotopic composition but progressively depleted in ITE. This observation is reinforced by the composition of lavas used in this study, showing a range in Th/La ratios at relatively constant Nd, Sr, Pb isotopic composition, where the variation in Th/La increases from essentially a single value at the depleted isotopic ratio to the largest Th/La variation at the enriched isotopic ratio, indicative of variable depletion in ITE during melting of the E-DMM (Fig. 3c). All the observations together support the statement that the E-DMM is melting incrementally without the aggregation of the different melt fractions. Furthermore, when we compare the DMORB samples produced from melting a source with isotopic composition indicative of E-DMM and of a D-DMM, we notice that both DMORB have essentially identical ITE concentration and very similar major element composition (Fig. 10c and d). These observations would be difficult to explain if the E-DMM and D-DMM sources were different lithologies (pyroxenite and peridotite respectively). Furthermore the δD of the Macquarie Island EMORB is similar to those of the D- and N-MORB (Bindeman et al., 2012), which is difficult to reconcile with the expected lower δD of a recycled oceanic crust dehydrated at a subduction environment (Shaw et al., 2008). Finally, the primitive major element composition of EMORB estimated by correction for fractional crystallization considering the water content of the melt is consistent with melting of a garnet peridotite (Appendix B and Fig. S3). The simple explanation for these observations is that the E-DMM is a peridotitic source.

Our statement does not rule out that recycled pyroxenites could have contributed to the generation of an E-DMM, but at the time of melt generation the source that melted to generate the EMORB was essentially peridotitic. Therefore, in this paper the lithology of E-DMM is considered a fertile peridotite rather than a pyroxenite. It is later shown in Sections 5.3 and 5.6 that this is supported by the relatively constant CO₂/Cl ratio of $\sim 57 \pm 8$ in E-DMM and D-DMM and by the fact that their volatile and ITE element abundance patterns can be related by a simple melting event; observations that are difficult to reconcile with a

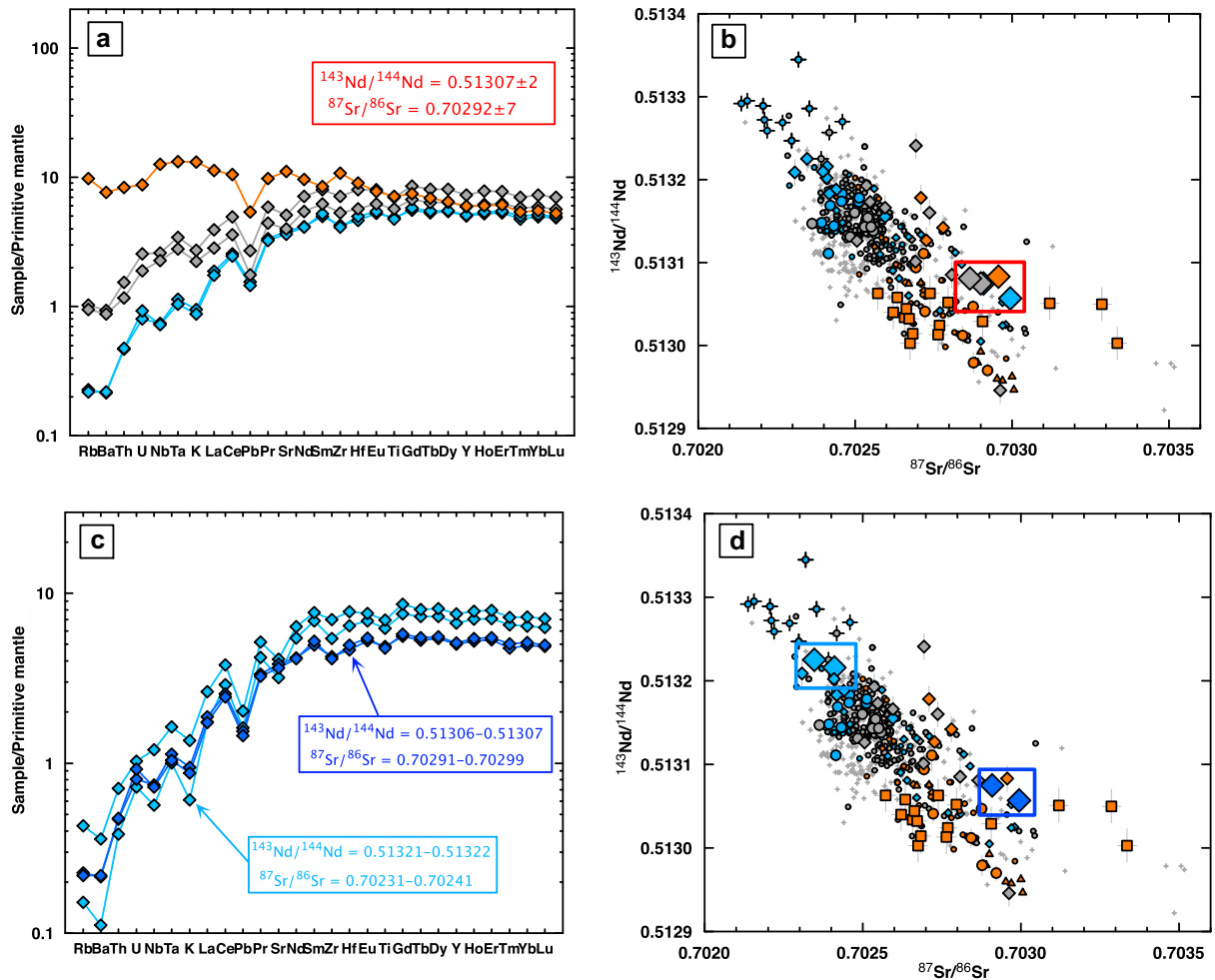


Fig. 10. (a) Primitive mantle normalized trace element diagram and (b) Sr and Nd isotopic composition of five samples (DMORB samples D45A and D45B, NMORB samples D37A and D47A, and EMORB sample D8B). All five samples have MgO between 8.0 and 9.0 wt%. (c) Primitive mantle normalized trace element diagram and (d) Sr and Nd isotopic composition of the isotopically depleted DMORB samples (blue, D44B and D10B) compared to isotopically enriched DMORB samples (dark blue, D45A and D45B). All four samples have MgO between 8.0 and 9.5 wt%. Primitive mantle composition is from [McDonough and Sun \(1995\)](#). Symbols are as in [Fig. 3](#). (For interpretation of the references to color in this figure legend, the reader is referred to the web version of this article.)

pyroxenite generated during recycling of the oceanic crust affected by subduction processes as the origin for the EMORB source.

5.2. The origin of NMORB: the presence of an NMORB mantle (DMM) or melting and mixing of two mantle components (D-DMM and E-DMM)

The NMORB samples in this study have intermediate volatile and trace element contents and isotopic compositions between the DMORB and EMORB samples. A fundamental question is whether NMORB and its volatile and trace element contents represent either the melting of a single mantle source (DMM) or the mixture of DMORB and EMORB. The answer to such question has significant implications for the evolution and composition of the Pacific upper mantle. [Pickle et al. \(2009\)](#) in their study of the QDG TF system show that there is a significant correlation between the bathymetry, the calculated crustal thickness

using residual mantle Bouguer anomaly (RMBA) and the composition of the erupted basalts in each ridge segment of the TF system. The shallow ridges have relatively thicker crust (i.e., higher magma flux) and lavas with intermediate compositions (NMORB) that underwent larger extent of magma differentiation (long lived magma chamber) compared to deeper ridges.

In fact, we do not have any real evidence for an NMORB mantle. The estimated probability density function defined by the Nd isotopes of clinopyroxene from abyssal peridotites ([Warren et al., 2009](#) and references therein) are similar to that defined by lavas from the QDG transform fault, NEPR seamounts, and other MORB from seamounts and intra-transform faults ([Wendt et al., 1999](#); [Hall et al., 2006](#); [Brandl et al., 2012](#)) ([Fig. 11](#)). The more homogeneous isotopic composition of the lavas may be due to melt aggregation either in the mantle or in magma chambers. Furthermore, the small length-scale of the isotopic variation (<2 cm) in abyssal peridotites suggests a

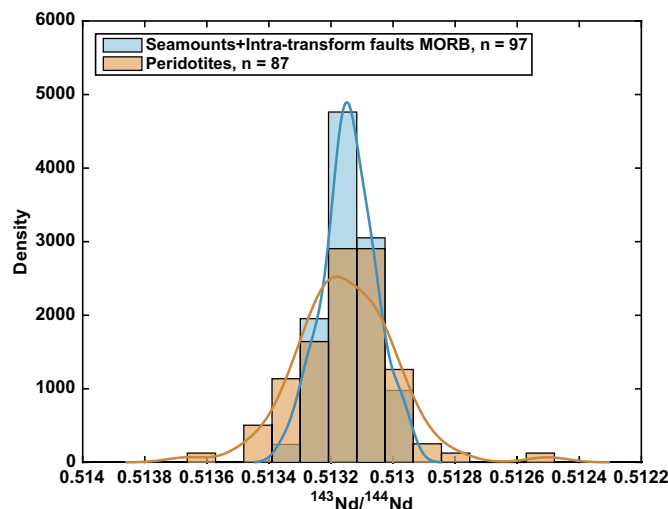


Fig. 11. Estimated probability density function of Nd isotopic composition in lavas from QDG transform fault, NEPR seamounts and other MORB from seamounts and intra-transform faults [Wendt et al. \(1999\)](#), [Hall et al. \(2006\)](#), [Brandl et al. \(2012\)](#) compared to clinopyroxene from abyssal peridotites ([Warren et al., 2009](#) and references therein). The seamount and transform fault lavas and the clinopyroxene from abyssal peridotites display a similar frequency distribution.

shallow level melt infiltration origin for the isotopic composition observed in clinopyroxenes from the lithospheric mantle rather than representing the compositional variation of the actual convecting mantle ([Warren et al., 2009](#); [Warren and Shimizu, 2010](#)). All these observations strongly suggest that the NMORB might represent mixing of melts from a two-component D-DMM and E-DMM mantle ([Niu et al., 1996](#); [Niu and Batiza, 1997](#)) rather than an actual DMM mantle source. To test this hypothesis we present a two-component mantle melting-mixing model in Section 5.4.

5.3. The volatile contents of the two Pacific upper mantle components (D-DMM and E-DMM)

In order to evaluate the two-component mantle melting-mixing model, it is important to first establish the range of the volatile budget for the two components given the significant effect that volatiles have on the melting process ([Gaetani and Grove, 1998](#); [Asimow and Langmuir, 2003](#); [Dasgupta and Hirschmann, 2006](#); [Hirschmann et al., 2009](#); [Filiberto et al., 2012, 2014](#); [Tenner et al., 2012](#); [Dasgupta et al., 2013](#)). Here we establish the range of volatile element contents of the D-DMM and E-DMM using the volatile to trace element ratios of our samples.

The average CO_2/Nb for the eight DMORB samples undersaturated in $\text{CO}_2\text{-H}_2\text{O}$ vapor phase (258 ± 40 , 2σ) ([Fig. 12a](#) and [b](#)) is consistent with the average CO_2/Nb ratio of 239 ± 46 reported for primitive un-degassed melt inclusions from the Siqueiros transform fault ([Saal et al., 2002](#)). This ratio can be used to determine the CO_2 content of the D-DMM. Assuming Nb concentration of 0.0864 ppm (D-DMM from [Workman and Hart \(2005\)](#)), the CO_2 content of D-DMM is 22.3 ± 3.5 (2σ) ppm ([Table 1](#)). We obtain a similar D-DMM CO_2 content of 23.8 ± 14 (2σ) ppm ([Table 1](#)) using the CO_2/Ba of the

samples (105 ± 61) ([Fig. 12c](#) and [d](#)) and assuming Ba concentration of 0.227 ppm (D-DMM from [Workman and Hart \(2005\)](#)).

In contrast to the DMORB samples, the measured CO_2/Nb and CO_2/Ba of the EMORB samples cannot be directly used to determine their mantle CO_2 contents since their CO_2 has been significantly affected by degassing. [Cartigny et al. \(2008\)](#) estimated a higher CO_2/Nb of 537 ± 112 for EMORB by correcting the CO_2 content for degassing using their carbon isotopic composition ([Fig. 12a](#)). The measured CO_2/Nb and CO_2/Ba for our EMORB samples clearly deviate from this ratio due to degassing of the CO_2 -rich vapor phase. In order to estimate the primitive CO_2 content in our EMORB, we use a different approach from that of [Cartigny et al. \(2008\)](#); namely, we use the correlation between CO_2 and Cl [$\text{CO}_2 = 22(\pm 14) + \text{Cl} \times 57(\pm 8)$] (uncertainties are 1σ) observed in the primitive un-degassed melt inclusions from the Siqueiros transform zone ([Saal et al., 2002](#)). We use the Cl content of the uncontaminated Macquarie Island samples to calculate the CO_2 content of the EMORB prior to degassing since they are the most ITE enriched EMORB samples, and therefore, the most likely melts representative of the E-DMM. Once corrected for degassing the estimated CO_2/Nb and CO_2/Ba of EMORB are 744 ± 165 (2σ) and 134 ± 23 (2σ) respectively. Our estimated EMORB CO_2/Nb (744 ± 165) is within error of the EMORB CO_2/Nb (537 ± 112) estimated by [Cartigny et al. \(2008\)](#) using a completely different approach ([Fig. 12a](#)). Furthermore, when we calculate the CO_2/Ba of the samples in [Cartigny et al. \(2008\)](#), we obtain a value of 97.8 ± 28 that compares well with our proposed value of 134 ± 23 ([Fig. 12c](#)). Using our EMORB CO_2/Nb and CO_2/Ba , the estimated CO_2 contents of the E-DMM are 990 ± 220 (2σ) ppm and 1010 ± 173 (2σ) ppm respectively ([Table 1](#)), assuming Nb and Ba content of 1.33 ppm and 7.54 ppm in the E-DMM ([Donnelly et al., 2004](#)). The

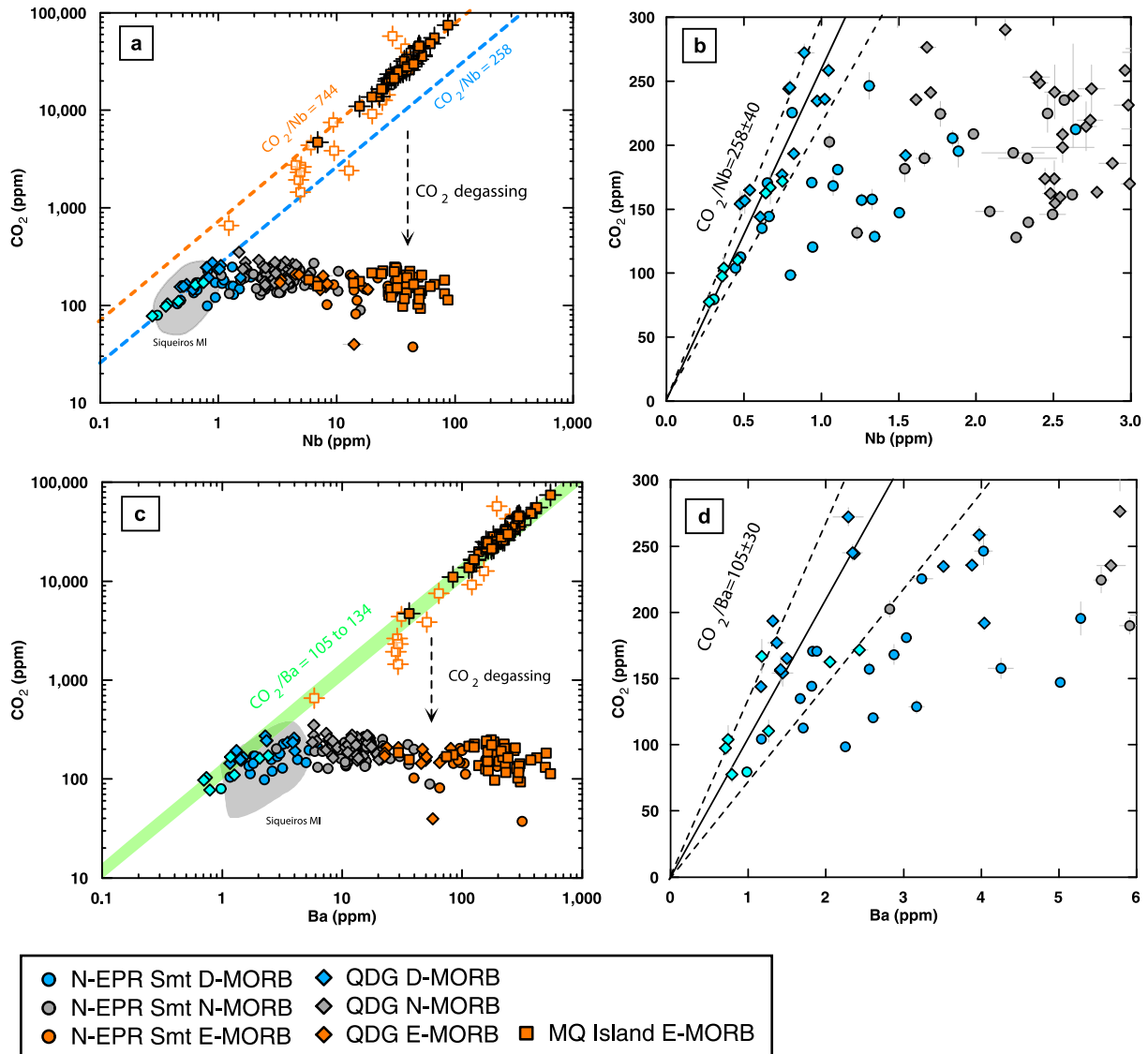


Fig. 12. (a) and (b) Measured and estimated CO₂ versus Nb of the samples (a) is in logarithmic scale and (b) is in linear scale and zoomed in. CO₂ in Macquarie Island samples (filled square with cross) estimated from the CO₂–Cl correlation (see Section 5.3). Also plotted are estimated CO₂ versus measured Nb in Mid-Atlantic Ridge MORB samples (open square with cross) from Cartigny et al. (2008). CO₂-undersaturated samples (light blue diamonds) define a constant CO₂/Nb ratio of 258 ± 40 (2σ) (dotted blue line), which is within error of the average CO₂/Nb (239 ± 46) of Siqueiros melt inclusions (gray field) from Saal et al. (2002). The CO₂ content estimated using the CO₂–Cl correlation (see Section 5.3), versus measured Nb of Macquarie Island samples defines a CO₂/Nb of 744 ± 154 (2σ) (dotted orange line) consistent within error of the CO₂/Nb of 537 ± 112 defined independently by the Mid-Atlantic Ridge MORB samples from Cartigny et al. (2008). (c) and (d) Measured and estimated CO₂ versus Ba of the samples. Symbols as in (a) and (b). (c) is in logarithmic scale and (d) is in linear scale and zoomed in. CO₂-undersaturated samples (light blue diamonds) define a CO₂/Ba ratio of 105 ± 60 (2σ), consistent with the Siqueiros melt inclusions (gray field) Saal et al. (2002) with higher CO₂/Ba ratios compared to those with lower CO₂/Ba ratios that might have interacted with plagioclase Saal et al. (2007). The CO₂ content estimated using the CO₂–Cl correlation (see Section 5.3), versus measured Ba of Macquarie Island samples defines a CO₂/Ba of 134 ± 23 (2σ) consistent within error of the CO₂/Ba of 97.8 ± 28 defined independently by the Mid-Atlantic Ridge MORB samples from Cartigny et al. (2008). The similar CO₂/Ba ratio of E-DMM (134 ± 23) and D-DMM (105 ± 61) suggests that the CO₂/Ba ratio is also relatively constant in the Pacific upper mantle (green field), as first observed by Michael and Graham (2013). Error bars are 2σ SE. (For interpretation of the references to colour in this figure legend, the reader is referred to the web version of this article.)

consistent estimate of CO₂/Nb and CO₂/Ba for the E-DMM using two different methods suggests that the CO₂–Cl relationship can be used to estimate the pre-degassing CO₂ content of Cl uncontaminated MORB

samples. In addition, the fact that we can use the same CO₂–Cl relationship for the DMORB and EMORB samples suggests that the CO₂/Cl ratio of Pacific upper mantle is relatively constant at $\sim 57 \pm 8$. Furthermore, the similar

Table 1
Estimated volatile element concentration of D-DMM, E-DMM, and the Pacific upper mantle.

Element	D-DMM ^a			E-DMM ^b			Pacific upper mantle (78% D-DMM + 22% E-DMM) (ppm)
	Average (ppm)	Range (ppm)	2 σ (ppm)	Average (ppm)	Range (ppm)	2 σ (ppm)	
CO ₂ ^c	22.3	19.8–24.3	3.5	990	800–1219	220	
CO ₂ ^d	23.8	16.0–32.3	14	1010	866–1184	173	
CO₂	22			990			235
Cl ^e	1.0	0.54–1.70	0.64	19.6	5.24–25.2	9.01	
Cl ^f	0.76	0.33–1.26	0.54	19.5	9.48–32.7	9.59	
Cl ^g	0.87	0.31–1.81	0.91	19	8.75–32.9	8.43	
Cl	0.4			22			5
H ₂ O ^h	80	58.9–93.5	17	517	325–633	184	
H₂O	59			660			191
F ⁱ	8.3	6.9–10.1	1.4	37.8	24.0–55.9	15.7	
F	8			31			13
S ^j	122	97–147	30	126	91–188	39	
S	100			165			114

Bold numbers represent model values.

^a Trace element concentration from [Workman and Hart \(2005\)](#).

^b Trace element concentration from [Donnelly et al. \(2004\)](#).

^c From CO₂/Nb ratio. For CO₂ content of the EMORB we used the CO₂–Cl correlation (refer to Section 5.3 for explanation).

^d From CO₂/Ba ratio. For CO₂ content of the EMORB we used the CO₂–Cl correlation (refer to Section 5.3 for explanation).

^e From Cl/K ratio.

^f From Cl/Nb ratio.

^g From Cl/Ba ratio.

^h From H₂O/Ce ratio. For E-DMM H₂O content, we only used the QDG EMORB samples (refer to Section 5.3 for explanation).

ⁱ From F/Nd ratio.

^j From S/Dy ratio.

CO₂/Ba ratio of E-DMM (134 ± 23) and D-DMM (105 ± 61) suggests that the CO₂/Ba ratio is also relatively constant in the Pacific upper mantle, as first observed by [Michael and Graham \(2013\)](#).

The higher C content of the EMORB relative to the NMORB has been ascribed to recycling of C (e.g. [Marty and Zimmermann, 1999](#)). The relatively constant CO₂/Cl and CO₂/Ba ratio in the D-DMM and E-DMM suggests the lack of significant fractionation between CO₂, Ba, and Cl during the formation of E-DMM. The C enrichment of E-DMM is difficult to explain by subduction processes since this process recycles C back into the mantle much more efficiently than the fluid mobiles Cl ([Wallace, 2005](#)) and Ba. The recycling of the oceanic mantle lithosphere previously metasomatized by low degree melt as the source of the E-DMM ([Niu et al., 2002](#)) is more consistent with our observation since CO₂, Ba, and Cl are highly incompatible elements and do not significantly fractionate from each other during melting.

We obtain consistent D-DMM and E-DMM Cl contents using the Cl/K of the Cl-uncontaminated samples. The Cl/K ranges from 0.01 to 0.1 ([Fig. 5b](#)). The range in Cl/K of the Cl-uncontaminated DMORB samples is 0.01–0.04, and the average Cl/K is 0.023 ± 0.015 (2 σ). Based on this average Cl/K and assuming K content in the mantle source of 43.2 ppm (Based on K/Nb ratio of 500 in our DMORB samples and a Nb concentration of 0.0864 from D-DMM composition of [Workman and Hart](#)

(2005)) the estimated Cl concentration of the D-DMM 1.0 ± 0.64 (2 σ) ppm ([Table 1](#)). The range in Cl/K of the Cl uncontaminated EMORB samples is 0.02–0.096 ([Fig. 5b](#)), and the average Cl/K is 0.078 ± 0.037 (2 σ). The Cl content of the E-DMM is 19.6 ± 9.01 (2 σ) ppm assuming K content in the mantle source of 253 ppm ([Table 1](#)) (Based on K/Nb ratio of 190 in our EMORB samples and a Nb concentration of 1.33 for the E-DMM of [Donnelly et al. \(2004\)](#)). We obtain similar D-DMM and E-DMM Cl contents using the Cl/Nb and Cl/Ba ratios of our samples ([Table 1](#)).

The total range of H₂O/Ce of the Cl uncontaminated samples ranges from 140 to 384 ([Fig. 7b](#)). The range in H₂O/Ce of the Cl uncontaminated DMORB samples is 140 to 220, and the average H₂O/Ce is 190 ± 41 (2 σ). Based on this average H₂O/Ce and assuming Ce content in the D-DMM of 0.421 ppm ([Workman and Hart, 2005](#)) the estimated H₂O concentration of the D-DMM is 80 ± 17 (2 σ) ppm ([Table 1](#)). The range in H₂O/Ce of the Cl uncontaminated EMORB samples is 165–384. Despite this large range in H₂O/Ce ratios of our EMORB samples, those having on average high H₂O/Ce ratios (QDG EMORB) are considered more representative of the E-DMM source. This assumption is based on the hypothesis that the range in H₂O/Ce ratio of EMORB has been produced by the diffusive loss of H₂O (H⁺) during E-DMM storage or EMORB percolation through the ambient D-DMM as explained in detail in Section 5.5.5 below. The average H₂O/Ce of the

Cl uncontaminated QDG EMORB (high $\text{H}_2\text{O}/\text{Ce}$ EMORB) is 313 ± 112 (2σ). Using this $\text{H}_2\text{O}/\text{Ce}$ ratio, the average H_2O content of the E-DMM is 517 ± 184 (2σ) ppm (Table 1) assuming Ce content in the mantle source of 1.65 ppm (Donnelly et al., 2004).

Previously, the F/Nd ratios of oceanic basalts have been found to be fairly constant (20.1 ± 5.8) with no correlation between this ratio and isotopic data (Workman et al., 2006). The F/Nd ratio of our samples, however, ranges from 14.3 to 45.4, significantly outside the previous global range (Fig. 13). The samples are not filtered for Cl contamination since seawater and high salinity brine contains insignificant amount of F (Holland, 1984), and most likely did not affect the F/Nd beyond analytical error. The range in F/Nd of the DMORB samples is 14.3–21.0, and the average F/Nd is 17.2 ± 2.9 (2σ). Based on this average F/Nd and assuming Nd content in the D-DMM of 0.483 ppm (Workman and Hart, 2005) the estimated F concentration of the D-DMM is 8.3 ± 1.4 (2σ) ppm (Table 1). The range in F/Nd of the EMORB samples is 19.5–45.0, and the average F/Nd is 30.7 ± 12.7 (2σ). The average F content of the E-DMM is 37.8 ± 15.7 (2σ) ppm (Table 1) assuming Nd content of 1.23 ppm (Donnelly et al., 2004).

The total range in S/Dy of the sulfide undersaturated samples is 136–311 (Fig. 9). The range in S/Dy of the sulfide undersaturated DMORB samples is 204–311, and the average S/Dy is 259 ± 64 (2σ). Based on this average S/Dy and assuming Dy content in the D-DMM of 0.471 ppm (Workman and Hart, 2005) the estimated S concentration of the D-DMM is 122 ± 30 (2σ) ppm (Table 1). The range in S/Dy of the sulfide undersaturated EMORB samples is 136–283, and their average S/Dy is 189 ± 58 (2σ). The average S content of the E-DMM is 126 ± 39 (2σ) ppm (Table 1) assuming Dy content in the mantle source of 0.666 ppm

(Donnelly et al., 2004). These mantle S content estimates are consistent with previous estimates (Morgan, 1986; Chaussidon et al., 1989; Lorand, 1990; Saal et al., 2002; Bézos et al., 2005).

5.4. Two-component mantle melting-mixing model: modeling method

We conducted near-fractional melting models for D-DMM and E-DMM using the pHMELTS program (Ghiorso et al., 2002; Asimow et al., 2004; Smith and Asimow, 2005) and subsequently mixed the calculated DMORB and EMORB following the method of Rudge et al. (2013). We used the major element composition of DMM from Workman and Hart (2005) for both the D- and E-DMM, based on the hypothesis that D- and E-DMM are both peridotitic (Section 5.1) and the assumption that the differences in their major element composition has a small effect on their melting behavior compared to the significant difference in their H_2O content (Section 5.3, Table 1). The trace element composition of D-DMM and E-DMM were taken from Workman and Hart (2005) and from Donnelly et al. (2004), respectively. The volatile element compositions of the D-DMM ($\text{CO}_2 = 22$ ppm, $\text{H}_2\text{O} = 59$ ppm, F = 8 ppm, Cl = 0.4 ppm, and S = 100 ppm) and of the E-DMM ($\text{CO}_2 = 990$ ppm, $\text{H}_2\text{O} = 660$ ppm, F = 31 ppm, Cl = 22 ppm, and S = 165 ppm) were obtained by running the model iteratively until it matches the observed geochemical data for D-, N- and EMORB. As can be seen in Table 1 the volatile contents used in the model are mostly within the range estimated from the measured volatile-refractory ITE ratios (Table 1). All volatile elements except for H_2O were considered as passive tracer elements. However, the H_2O

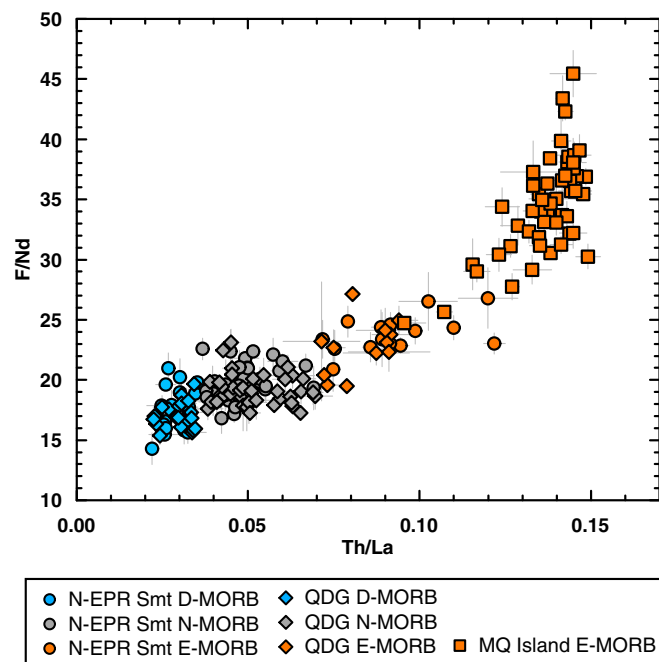


Fig. 13. F/Nd versus Th/La ratios for the samples. F/Nd ratio of our samples ranges from 14.3 to 45.4, significantly outside the previously defined global constant F/Nd ratio of 20.1 ± 5.8 Workman et al. (2006).

concentration in the melt is also calculated as a tracer independent from that thermodynamic calculation by pHMELTS using the partition coefficient from Hauri et al. (2006), and this tracer H₂O concentration is used in the following sections. The partition coefficients for H₂O and F are from Hauri et al. (2006) and the trace element partition coefficients are from Kelemen et al. (2003). For reasons given in Section 4.4, the Ba partition coefficient from Kelemen et al. (2003) was used to simulate the behavior of Cl. For the CO₂ partition coefficient, experimental results of Rosenthal et al. (2015) are used. The SCSS model of Fortin et al. (2015) was used in conjunction with pHMELTS to calculate the S concentration of each one of the incremental D-DMM and E-DMM melts obtained from the model. The sulfur content at sulfide saturation (SCSS) was calculated for each incremental melt using their major element composition, H₂O content, P, and T obtained using pHMELTS. The S content of the incremental melts is set to zero when the sulfide in the mantle is consumed. The Sr, Nd, and Pb isotopic composition of the D-DMM are assumed to be those of sample GN10-3 from Garret transform fault (Wendt et al., 1999), which is a sample with one of the most depleted Sr, Nd, and Pb isotopic compositions in the EPR. The Sr, Nd and Pb isotopes used for the E-DMM are the highest Sr, and Pb isotopes and the lowest Nd isotopes measured for EPR EMORB. We used the Sr and Nd isotopic composition of the sample 3010-1502 from NERP seamount 6 (Brandl et al., 2012) and Pb isotopic composition of the Macquarie Island sample GG256 (Kamenetsky and Maas, 2002). Although this E-DMM is a hypothetical source since its isotopic composition is not defined by single sample, this is done only to reproduce some of the extreme isotopically enriched samples, and the results of our model does not significantly change by using a similar isotopic composition of a single sample (e.g. R78-6) from the NEPR seamount (Niu et al., 2002). We used a mantle potential temperature of 1350 °C. Melt extraction starts when the degree of melting reaches 0.5 wt%, and 0.5 wt% melt (relative to the instantaneous solid mass) is retained in the mantle at each melting step (near fractional melting). The final pressure of melting, at the top of melting triangle, was set to the bottom of a 6.4 km oceanic crust, 1800 bars, assuming crustal density of 2890 kg m⁻³ (Carlson and Raskin, 1984). This is a simplification for the model, and in reality final depth of melting varies among distinct ridge settings (Morgan and Forsyth, 1988; Shen and Forsyth, 1992). For the description of the mixing model, refer to Appendix C and for more details refer to Rudge et al. (2013).

We consider four main parameters in the two-component mantle melting-mixing model (Table 2): (1)

The fraction of the D-DMM in the Pacific upper mantle (p_{DDMM}); for simplicity and following the traditional view of a well-mixed upper mantle (van Keken et al., 2002) we assumed a uniform distribution of D-DMM and E-DMM everywhere in our model (beneath the fracture zone, the seamounts and the ridge axis); hence p_{DDMM} is kept constant for these three different ridge settings. (2) The mixing parameter (N), indicating the extent of aggregation of the melts produced from both mantle sources. (3) The degree of melting below which we allow for a fraction of the EMORB to escape the aggregation within the melting triangle (F_{ext}); this melt is assumed to avert the aggregation at the wings of the melting triangle by forming part of the freezing front at the base of the oceanic lithosphere (Sparks and Parmentier, 1991; Montesi and Behn, 2007; Katz, 2008; Gregg et al., 2009; Hebert and Montesi, 2010, 2011; Katz and Weatherley, 2012). (4) The fraction of EMORB with $F < F_{ext}$ that is allowed to escape aggregation (f_{escape}).

The Kernel smoothed probability density estimates (KDE) of Th/La ratio and ¹⁴³Nd/¹⁴⁴Nd isotopic ratio of the model and natural samples are used to assess the match between the model and (1) our QDG TF samples (Fig. 14a and d), (2) our NEPR seamounts samples (Fig. 14b and e), and (3) the compilation of EPR axial MORB (Mallick et al., in revision; Gale et al., 2013) (Fig. 14c and f). We tested two different variations of the two-component melting-mixing model to obtain the model KDEs that best matches those of natural samples. The first model is where no melt escape from the melting triangle and all the incremental melts are aggregated. Although the model can reproduce the KDEs for the ¹⁴³Nd/¹⁴⁴Nd of our samples, the Th/La KDEs are far too enriched compared to those of our samples (Fig. S4). The second model is where a fraction of the EMORB (f_{escape}), representing a low degree melting ($F < F_{ext}$), escapes the melt aggregation by forming part of the freezing front at the base of the oceanic lithosphere. The resulting model ¹⁴³Nd/¹⁴⁴Nd and Th/La KDEs can reproduce those of our QDG TF samples, our NEPR seamounts samples, and the compilation of EPR axial MORB (Fig. 14). The parameters required to obtain the best-matching model KDEs for the three ridge settings (transform fault, seamount and ridge axis) are as follow: QDG transform fault ($p_{DDMM} = 0.78$, $N = 16$, $F_{ext} = 1.3\%$, $f_{escape} = 0.65$), NEPR seamounts ($p_{DDMM} = 0.78$, $N = 40$, $F_{ext} = 1.3\%$, $f_{escape} = 0.75$), and compilation of EPR axial MORB ($p_{DDMM} = 0.78$, $N = 99$, $F_{ext} = 1.3\%$, $f_{escape} = 0.80$). The main parameter controlling the compositional difference of lavas from these three ridge settings is the mixing parameter N . We have explored a range of values of p_{DDMM} , F_{ext} , and f_{escape} .

Table 2
Parameters used in the two-component mantle melting-mixing model.^a

Parameter	Value	Description
p_{DDMM}	0.78	Solid fraction of D-DMM in the upper mantle
N	16–99	Extent of melt aggregation ($N = 0$ means no aggregation, $N = \infty$ means complete aggregation)
F_{ext}	1.3%	Degree of melting below which a fraction of EMORB may escape the melt aggregation
f_{escape}	0.65–0.8	Fraction of EMORB with $F < F_{ext}$ that escapes aggregation

^a Based on the model of Rudge et al. (2013).

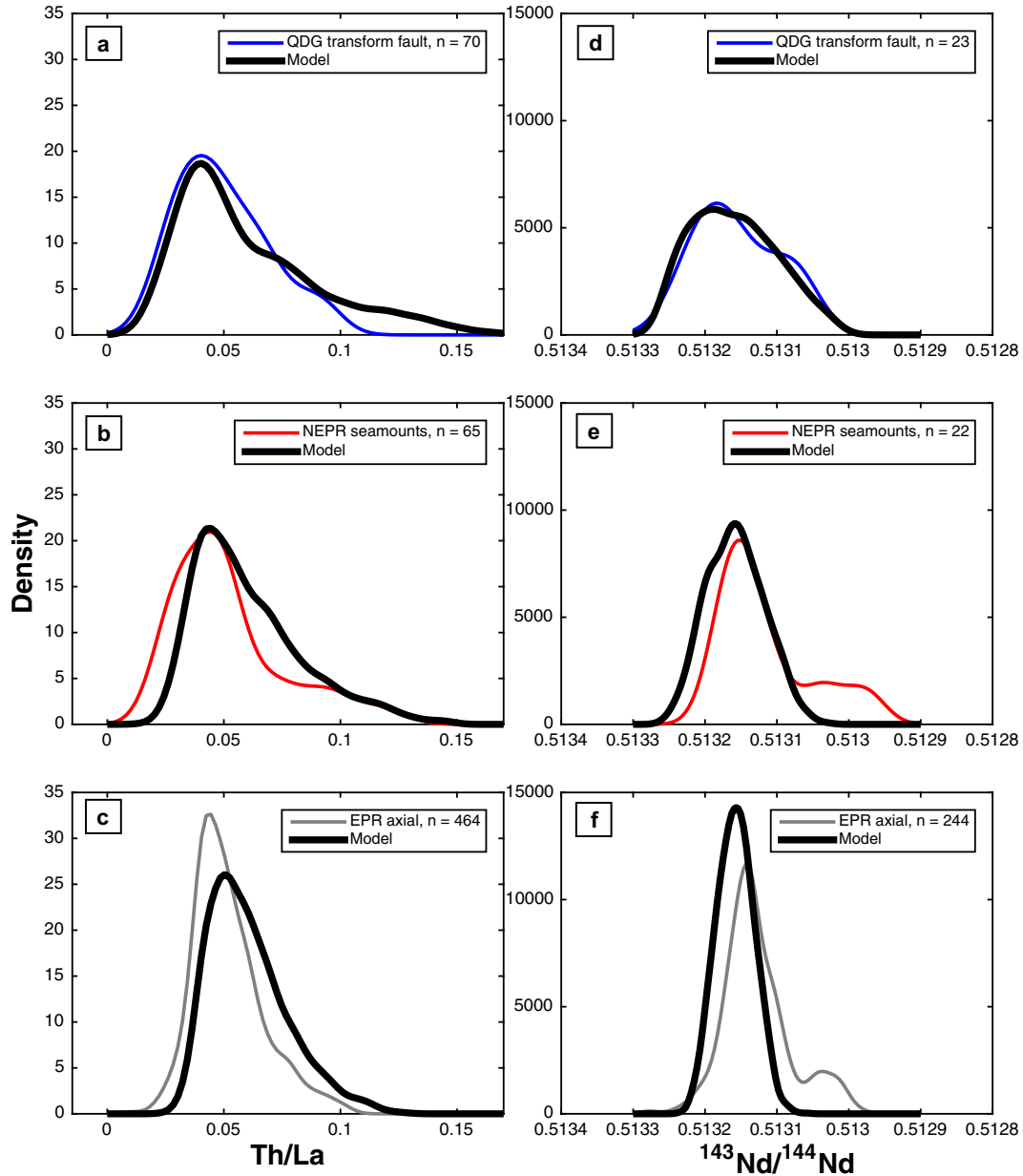


Fig. 14. Kernel smoothed probability density estimates (KDE) for Th/La (a, b, c) and $^{143}\text{Nd}/^{144}\text{Nd}$ (d, e, f) using a model where a fraction of the EMORB melt ($f_{\text{escape}} = 65\text{--}80\%$), representing a low degree melting ($F < F_{\text{ext}} = 1.3\%$), escape the melt aggregation by forming part of the freezing front at the base of the oceanic lithosphere (thick black line) reproducing KDEs of (a, d) our QDG TF samples (blue line), (b, e) our NEPR seamount samples (red line), and (c, f) compilation of EPR axial MORB (grey line) (Gale et al., 2013; Mallick et al., in revision), see Section 5.4 in text for explanation of the models and parameters. The parameters required to obtain the best-matching model KDEs for the three ridge settings (transform fault, seamount and ridge axis) are as follow: QDG transform fault ($p_{DDMM} = 0.78$, $N = 16$, $F_{\text{ext}} = 1.3\%$, $f_{\text{escape}} = 0.65$), NEPR seamounts ($p_{DDMM} = 0.78$, $N = 40$, $F_{\text{ext}} = 1.3\%$, $f_{\text{escape}} = 0.75$), and compilation of EPR axial MORB ($p_{DDMM} = 0.78$, $N = 99$, $F_{\text{ext}} = 1.3\%$, $f_{\text{escape}} = 0.80$). (For interpretation of the references to colour in this figure legend, the reader is referred to the web version of this article.)

keeping the mixing parameter N constant for each ridge settings. The result of running 100 models for each ridge settings shows that in successful runs reproducing the natural KDEs, the parameters p_{DDMM} and F_{ext} negatively correlates with each other, while f_{escape} does not correlate well with either p_{DDMM} or F_{ext} . The range of parameters that produces model KDEs that matches those of natural sam-

ples are as follows: $p_{DDMM} = 0.74\text{--}0.82$, $F_{\text{ext}} = 0.7\text{--}2.9\%$, $f_{\text{escape}} = 0.64\text{--}0.93$. Within these ranges, the values of the parameters given above for the three ridge settings best matches the KDEs of the natural samples assuming uniform distribution of D-DMM and E-DMM in a well-mixed upper mantle (van Keken et al., 2002). We did not attempt to reproduce the KDE of Macquarie Island

samples because they mostly represent melts from a single E-DMM component (see [Appendix D](#)).

Under the assumption that the compositions and uniform distribution of D-DMM and E-DMM used in this model are similar to those in the Pacific upper mantle, the results have potentially important implications on the melt transport processes beneath MOR, the control that the E-DMM melts have on the composition of axial MORB, the trace and volatile element budgets of the metasomatized oceanic lithosphere ([Niu et al., 2002](#)), the degree of melting and mixing at different ridge settings (transform fault, seamounts, ridge axis), and the composition of the Pacific upper mantle.

For all three ridge settings a fraction of a low degree melting of the E-DMM must escape melt aggregation, which has potential implications for melt transport process as well as the volatile and trace element budget of the oceanic lithosphere. A possible mechanism by which this melt could escape aggregation may be by low degree melts of a E-DMM produced at the wings of the melting triangle vertically migrating and freezing at the thermal boundary layer consistent with geodynamic models of the mid-ocean ridge ([Sparks and Parmentier, 1991](#); [Montesi and Behn, 2007](#); [Gregg et al., 2009](#); [Hebert and Montesi, 2010, 2011](#); [Havlin et al., 2013](#)). Therefore, it is quite plausible that a fraction of the EMORB (and perhaps DMORB, although we cannot observe this geochemically) escapes the melt aggregation by freezing at the base of the oceanic lithosphere instead of erupting off-axis. The consequence of such a process is that the base of the oceanic lithosphere becomes enriched in volatile and trace elements, which will eventually be recycled back into the mantle at subduction zones and might be responsible for the generation of the E-DMM ([Niu et al., 2002](#); [Donnelly et al., 2004](#)). Following this hypothesis, and to be consistent within our model, the fraction of EMORB that escaped the melt aggregation (65–80% of the $F < F_{\text{ext}} = 1.3\%$) is mixed with the bottom 22% of the oceanic lithospheric mantle (residual bottom ~13 km of a 60 km thick oceanic lithosphere calculated using pHMELTS). The 22% fraction of the oceanic lithospheric mantle that is metasomatized is required to reproduce the proportion of E-DMM in the Pacific upper mantle estimated from our two-component mantle melting-mixing model. The major element composition of this metasomatized lithosphere is similar to that of E-DMM used as starting composition in our model ([Table S2](#)); as we mentioned earlier in this section; this is due to the small amount of melt added to the residual peridotite to form the E-DMM. Furthermore, the primitive mantle normalized trace element pattern of such a modeled metasomatized lithosphere ([Fig. 15](#)) closely resembles those of the E-DMM composition from [Donnelly et al. \(2004\)](#). Although we acknowledge the circularity in this model, the idea of a small amount of low degree melts escaping the aggregation by metasomatizing the lower oceanic lithosphere seems to be consistent with our two-component mantle melting-mixing model, the proposed processes acting at mid-ocean ridges and with the models for the generation of the E-DMM ([Sparks and Parmentier, 1991](#); [Niu et al., 2002](#); [Montesi and Behn, 2007](#); [Katz, 2008](#);

[Gregg et al., 2009](#); [Hebert and Montesi, 2010, 2011](#); [Katz and Weatherley, 2012](#)).

Another potential implication from the model result is that melting of a DMM mantle may not be necessary to explain the composition of NMORB, since the mixture of DMORB and EMORB can reproduce the composition of an NMORB. In other words, our model can reproduce the KDEs of a compilation of axial NMORB erupting at the EPR reasonably well. This may suggest that the extensive melt aggregation of DMORB and EMORB underneath the ridge produces a large amount of NMORB, whereas the lack of efficient melt aggregation at intra-transform spreading settings ([Morgan and Forsyth, 1988](#); [Reynolds and Langmuir, 1997](#)) and seamounts ([Fornari et al., 1988](#); [Perfit et al., 1996](#); [Niu et al., 2002](#)) results in less NMORB and more DMORB and EMORB. Our model not only reproduces the KDEs of the samples, but also the trace element contents and isotopic composition of EPR MORB ([Fig. 16a–d](#)). Note the “fan-shape” distribution of the samples in plots of very incompatible trace element ratios versus isotopes are pinned at the isotopic composition of the D-DMM and spreads as it gets closer to those of E-DMM ([Fig. 16b–d](#)). This suggests that the melts produced during variable degrees of melting of the E-DMM controls most of the MORB geochemical variation. Although we cannot rule out the presence of an NMORB mantle source, we do not find any compelling argument to support its existence and by simply applying the Occam’s Razor principle, this hypothesis loses credence.

Although our model reproduces the KDEs and compositional range of our samples fairly well ([Figs. 14 and 16](#)) by considering several key assumptions (a uniform distribution of D-DMM and E-DMM, the escape of a fraction of the low degree melting from the E-DMM and different extent of melt aggregation at different ridge settings), there are several other parameters that could influence the results, but for simplicity have not been considered yet. Exploration of parameters such as difference in the final depth of melting among distinct ridge settings ([Morgan and Forsyth, 1988](#); [Shen and Forsyth, 1992](#)) and ridge migration over the mantle ([Carbotte et al., 2004](#)) are outside the scope of this paper and will be part of future work.

In the following section we explore the implications of the two-component mantle melting-mixing model on the evaluation of volatile-refractory trace element ratios of basalts and the volatile budget of the Pacific upper mantle.

5.5. Modeling of the volatile to trace element ratios

5.5.1. Carbon: melting-mixing model

The two-component mantle melting-mixing model and the CO₂ concentration of D-DMM (22 ppm) and E-DMM (990 ppm) ([Table 1](#) and [Section 5.3](#)) reproduces the CO₂, Nb, and Ba of our most depleted DMORB samples, those estimated for Macquarie Island samples, and the samples corrected for degassing by [Cartigny et al. \(2008\)](#) ([Fig. 17a–d](#)).

Deep low degree melts are more ITE enriched and have higher CO₂/Nb ratios than shallow high degree melts due to the more incompatible behavior of CO₂ than Nb

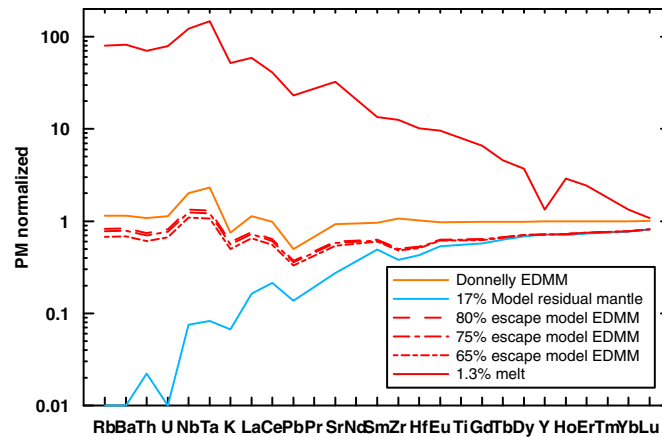


Fig. 15. Primitive mantle normalized trace element diagram of a modeled E-DMM produced by addition of a fraction ($f_{\text{escape}} = 65\text{--}80\%$) of low degree melt ($F < F_{\text{ext}} = 1.3\%$) to the bottom 22% of the model residual mantle (both calculated using pHMELTS). The E-DMM composition from [Donnelly et al. \(2004\)](#) is shown for comparison.

([Rosenthal et al., 2015](#)). Hence, CO_2/Nb ratio in the samples may differ from those in the source if the incremental melts of the source did not completely aggregate. However, this requires preferential loss or gain of extremely low degree melts, and also considering the uncertainty of $\sim 20\%$ in our estimated CO_2/Nb of D-DMM and E-DMM, the effect of this process may not be significant. Instead of using the CO_2/Nb ratio, the relatively constant CO_2/Ba ratio of 105–134 in MORB can be used to estimate the primitive CO_2 concentration of MORB samples. However, fractional crystallization of plagioclase affects the CO_2/Ba ratio of magmas (Section 4.4). Furthermore interaction of magmas with gabbro, especially gabbro with ITE enriched plagioclase derived from EMORB can affect the Ba concentration of the melt ([Saal et al., 2007](#)). These processes may explain the larger variability in CO_2/Ba ratios of $\text{CO}_2\text{--H}_2\text{O}$ vapor undersaturated DMORB in this study ($\pm 60\%$, 105 ± 61 (2σ)) compared to their less variable CO_2/Nb ratios ($\pm 16\%$, 258 ± 40 (2σ)). Larger variability in CO_2/Ba relative to CO_2/Nb is also observed in the Siqueiros melt inclusions ([Saal et al., 2002](#)). The opposite observation (CO_2/Ba variability $<$ CO_2/Nb variability) is expected from a melting process since the $\text{CO}_2\text{--Ba}$ pair behaves more similarly compared to $\text{CO}_2\text{--Nb}$ pair ([Rosenthal et al., 2015](#)). CO_2/Nb ratio of MORB is less affected by either interaction with gabbro or by fractional crystallization, thus it is an alternative tool to estimate the primitive CO_2 concentration of degassed MORB samples.

The CO_2 content of the average oceanic crust was estimated using the two component melting-mixing model. Using the model parameters that reproduce the KDEs of EPR axial MORB compilation ($p_{\text{DDMM}} = 0.78$, $F_{\text{ext}} = 1.3\%$, $f_{\text{escape}} = 0.80$) and setting the mixing parameter N to ∞ (complete mixing), we obtain an average oceanic crust CO_2 content of 955 ppm. The average CO_2 flux from the ridge is 1.32×10^{12} mol yr^{-1} or 58 Mt yr^{-1} using a MOR mass flux of $21 \text{ km}^3 \text{ yr}^{-1}$ ([Crisp, 1984](#)) and oceanic crust density of 2890 kg/m^3 ([Carlson and Raskin, 1984](#)). This compares well with the CO_2 flux of $2.2 \pm 0.9 \times 10^{12}$ mol yr^{-1} calculated by

[Marty and Tolstikhin \(1998\)](#) using the $\text{C}/^3\text{He}$ ratio in MORB and the mid-ocean ridge He flux.

5.5.2. Chlorine: melting-mixing model

The two-component mantle melting-mixing model and the Cl concentration of D-DMM (0.4 ppm) and E-DMM (22 ppm) ([Table 1](#) and Section 5.3) reproduces the Cl/K of QDG transform fault, NEPR seamount, and Macquarie Island samples ([Fig. 18a](#) and [S5a](#)). In [Fig. 18a](#), note that some model mixtures do not plot within the area defined by the E- and D-DMM melting curves due to the curvature of the mixing between the model E- and DMORB.

The range of Cl/K produced by the model melts can be used to constrain the maximum Cl/K of the uncontaminated DMORB and NMORB samples at 0.04 and 0.06 respectively ([Fig. 18a](#)), which were used in Section 5.3 to filter our samples for contamination. The highest Cl/K ratio for uncontaminated DMORB therefore could be much higher than previously defined (~ 0.01 of ([Michael and Cornell, 1998](#); [Saal et al., 2002](#))) due simply to the mixing process. Therefore, DMORB and NMORB samples with Cl/K below 0.04 and 0.06 may be potentially uncontaminated by high salinity brine or seawater. The model reproduces some but not all of the range in Cl/K for a given Th/La of the enriched samples ([Fig. 18a](#)). This is most likely due to the difference in partition coefficient between Cl (Kd similar to Ba) and K that becomes more evident in melts produced by low degree of melting of a E-DMM, such as the Macquarie Island lavas.

5.5.3. Fluorine: melting-mixing model

The two-component mantle melting-mixing model using F concentration in the D-DMM and E-DMM of 8 ppm and 31 ppm respectively ([Table 1](#) and Section 4.3) reproduce the F/Nd ratios of the QDG transform fault, NEPR seamount, and Macquarie Island samples ([Figs. 18b](#) and [S5b](#)). The high F/Nd ratio (~ 50) of the modeled low degree melting of the E-DMM source is due to the different partition coefficient between F and Nd (max. fractionation of \sim factor of 2 from the E-DMM source F/Nd of 25) during

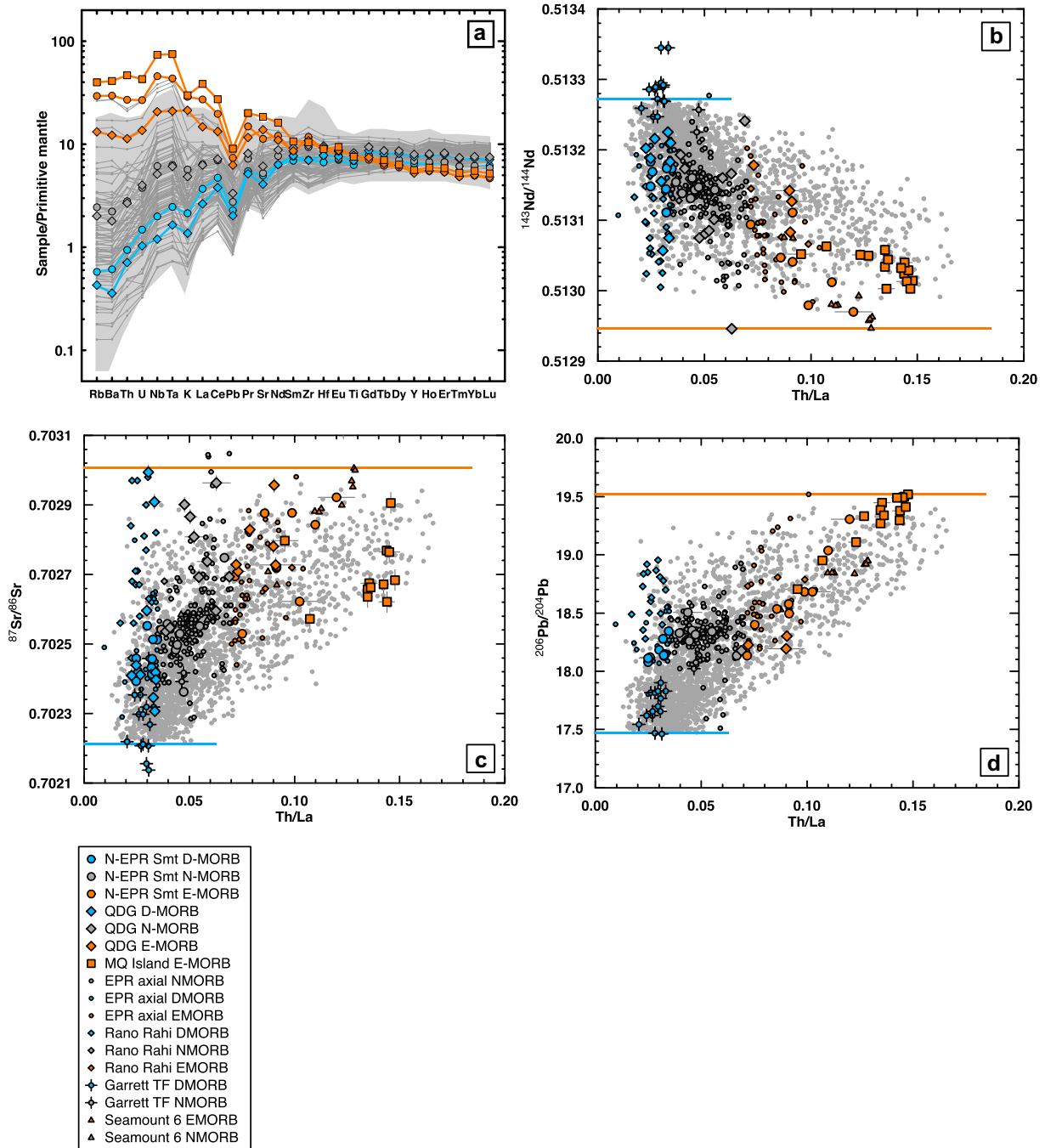


Fig. 16. (a) Primitive mantle normalized trace element diagram of a randomly selected set of melt produced by the two-component mantle melting-mixing model (gray line with dot symbols), and representative composition of natural samples collected from each location. The grey field is the entire range of trace element abundance observed in a compilation of EPR axial MORB Gale et al. (2013), Mallick et al. (in revision) that have greater than 6 wt% MgO. The trace element concentrations of the model mixtures are increased by 81% (assuming perfect incompatibility of the trace elements in crystallizing phases) to take into account that our samples have experienced fractional crystallization. This is based on the fractional crystallization model using the MELTS program Ghiorso and Sack (1995), Asimow and Ghiorso (1998) (see Section 4.4) that suggests a primitive melt with MgO of 12.5 wt% fractionally crystallizes 38 to 55% of its mass until reaching a MgO of 8.5–7.5 wt%. (b) Nd, (c) Sr, and (d) Pb isotopic composition versus Th/La of our model results (grey points) and natural samples. The model melt mixture between incremental melts from the E-DMM (orange line) and the D-DMM (blue line) using pHMELTS reproduces the field defined by the EPR MORB (see Section 5.4 for information about the model). The small circles are EPR axial MORB Gale et al. (2013), Mallick et al. (in revision), small diamonds are Rano Rahi seamounts Hall et al. (2006), small triangles are Seamount 6 Brandl et al. (2012), and the circle with sticks are Garrett transform fault Wendt et al. (1999). The model presented here is the one used for modeling the QDG TF samples with lowest degree of mixing ($N = 16$) that illustrate the largest compositional range. Error bars are 2σ SD for isotopic composition and 2σ SE for the Th/La ratios. (For interpretation of the references to colour in this figure legend, the reader is referred to the web version of this article.)

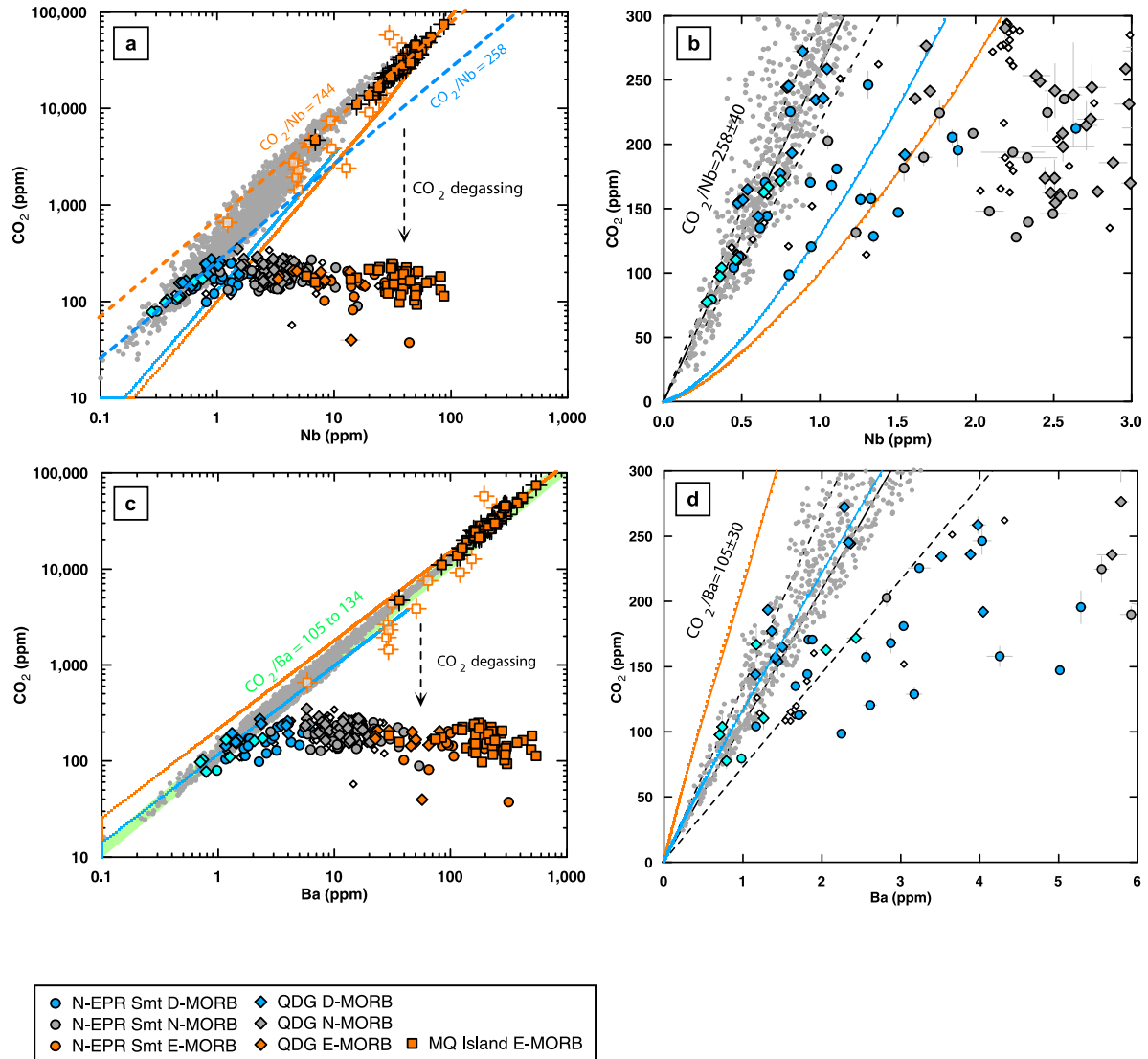


Fig. 17. CO_2 versus Nb (a, b) and Ba (c, d) for the model mixture (grey points), incremental melting model of D-DMM (solid blue line), and E-DMM (solid orange line) using pHMELTS (see Section 4.4 for model explanation) along with our samples and compilation of EPR MORB (small open diamonds) Michael (1988), Danyushevsky et al. (2000), Eiler et al. (2000), Saal et al. (2002), Wanless et al. (2011), Soule et al. (2012), Clog et al. (2013). CO_2 estimated for Macquarie Island samples (filled square with cross) using CO_2 –Cl–Nb correlation (see Section 5.3). Also plotted are the estimated CO_2 versus measured Nb and Ba for Mid-Atlantic Ridge MORB samples (open square with cross) from Cartigny et al. (2008). The model mixture reproduces our most depleted DMORB samples, the estimated Macquarie Island samples, and the Mid-Atlantic Ridge (MAR) MORB samples from Cartigny et al. (2008). (b) and (d) shows that the model mixture reproduces the CO_2/Nb and CO_2/Ba of our most depleted vapor undersaturated samples. In (b) and (d), the incremental melting models are discrete points rather than lines, but for clarity they are shown as lines. (For interpretation of the references to color in this figure legend, the reader is referred to the web version of this article.)

melting in the presence of garnet, where Nd is more compatible than F. The most enriched model mixtures ($\text{Th}/\text{La} > \sim 0.10$) reproduces the high F/Nd ratio of Macquarie Island samples, consistent with the major, trace and isotopic composition of these samples strongly suggesting that they were low degree melts from an E-DMM that hardly mixed with DMORB melts (Figs. 16 and 18, S1, S5b, Appendix D). Once garnet is no longer present in the source, F and Nd starts to behave more similarly producing a kink in the E-DMM melting curve at Th/La of ~ 0.095 . At

higher degrees of melting after consumption of clinopyroxene, for both E-DMM and D-DMM, the bulk partition coefficient of fluorine becomes higher than Nd, resulting in a continuous increase in F/Nd with increasing degrees of melting. Thus, initially F/Nd decreases during melting in the garnet field and after clinopyroxene consumption F/Nd increases with the increasing degree of melting. Note that in a plot F/Nd versus Nd isotopes (Fig. S5b), the two-component melting-mixing produce non-linear mixing trends indicating that the observed compositional variation

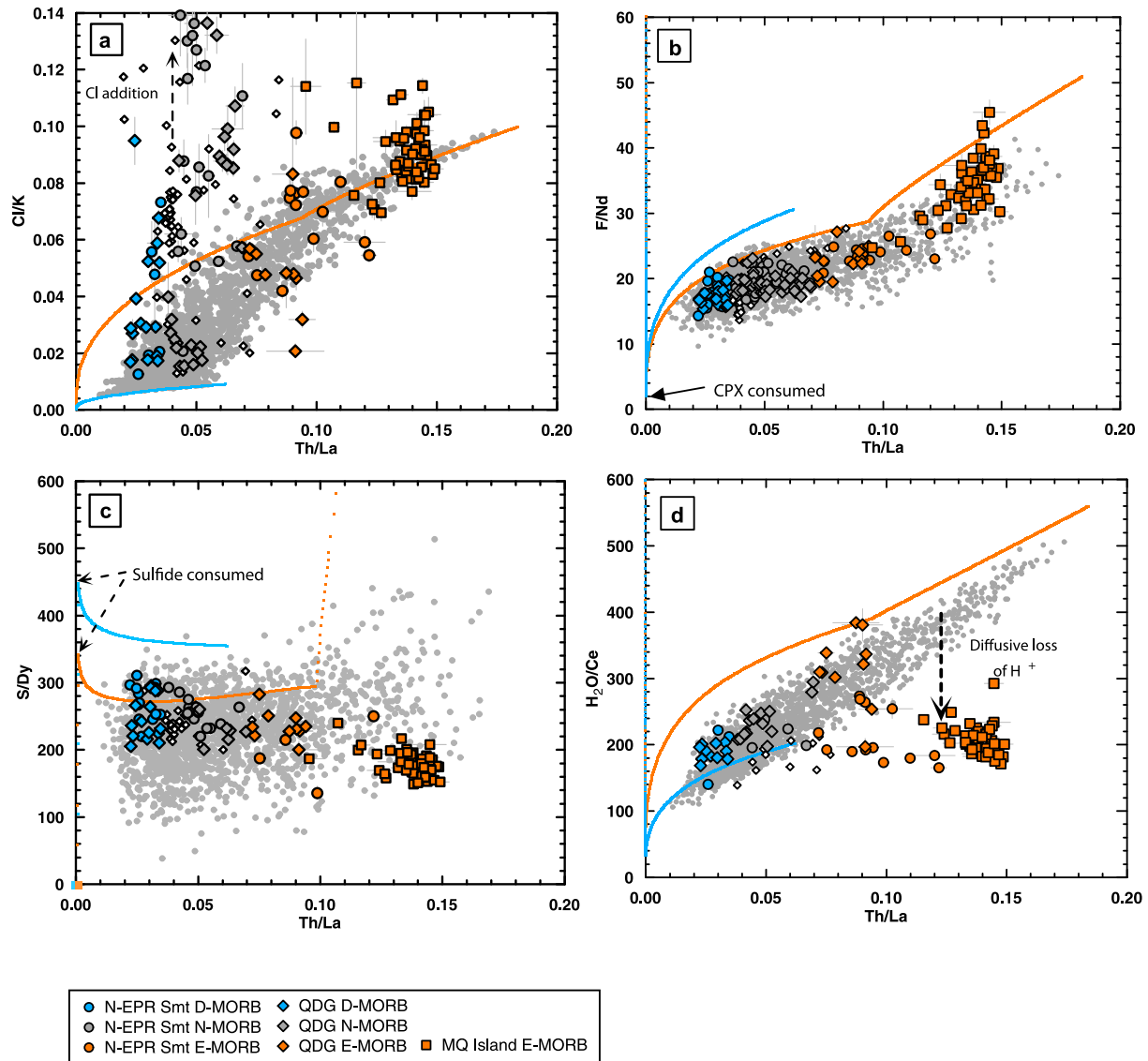


Fig. 18. (a) Cl/K, (b) F/Nd, (c) S/Dy, and (d) H₂O/Ce versus Th/La of the model mixture (grey points), incremental melting model of D-DMM (blue line), and E-DMM (orange line) using pHMELTS (see Section 5.4 for model explanation) along with our samples and EPR compilation (small open diamonds) Michael (1988), Danyushevsky et al. (2000), Eiler et al. (2000), Saal et al. (2002), Wanless et al. (2011), Soule et al. (2012) and Clog et al. (2013). The kinks in the E-DMM melting model curves at Th/La of ~ 0.095 is due to the consumption of garnet in the source. The samples plotted in (c) and (d) are filtered for sulfide saturation (see Section 4.3) and Cl contamination (see Section 4.2) respectively. In (a), the mixture limits the possible Cl/K of uncontaminated DMORB and NMORB samples at 0.04 and 0.06 respectively. In (b), the model mixture reproduces the samples including the high F/Nd samples from Macquarie Island. Note that the F/Nd trend changes after clinopyroxene consumption. In (c) the model mixture reproduces the range of S/Dy ratios in our DMORB and NMORB, but not the consistently low S/Dy ratios in the EMORB samples in particular those from Macquarie Island (refer to Section 5.5.6 for the explanation). In (d) the two-component mantle melting-mixing model reproduces the H₂O/Ce and Th/La of the DMORB, NMORB, and EMORB samples with high H₂O/Ce, but not the ones with low H₂O/Ce. This low H₂O/Ce may be due to variable diffusive loss of H₂O (H⁺) from the E-DMM to the ambient D-DMM as a result of either variable residence time and length scale of the E-DMM or EMORB melt percolation and extraction (see Section 5.5.5 and Fig. 19). Note H₂O/Ce change after clinopyroxene is consumed (18% melting for DDMM and 19.5% melting for EDMM). (For interpretation of the references to colour in this figure legend, the reader is referred to the web version of this article.)

does not require more than two mantle source components (Stracke and Bourdon, 2009; Brandl et al., 2012). The model mixture, as expected, also reproduces the curved field defined by our samples in an Yb/Nd-La/Nd diagram (not shown), which was observed by Brandl et al. (2012).

5.5.4. Water: melting-mixing model

The two-component mantle melting-mixing model and the H₂O concentration of D-DMM (59 ppm) and E-DMM (660 ppm) (Table 1 and Section 5.3) reproduces the H₂O/Ce of DMORB and NMORB samples, and the

EMORB samples with higher H_2O/Ce (Figs. 18d and S5d). Similar to F/Nd, the consumption of clinopyroxene in the source at higher degrees of melting makes the bulk partition coefficient of water higher than Ce, which results in a continuous increase in H_2O/Ce with increasing degrees of fractional melting. The two-component mantle melting-mixing model cannot explain the entire range of H_2O/Ce in the EMORB samples. The lower H_2O/Ce EMORB samples may either be melts from a low H_2O/Ce E-DMM or they may be melts from a high H_2O/Ce E-DMM that experienced subsequent kinetic process that decreased its H_2O .

5.5.5. Water in E-DMM and EMORB: fractionation of H_2O/Ce due to H^+ diffusion

One likely explanation for the range in H_2O/Ce of the E-DMM might be different degrees of diffusive loss of H_2O (H^+) during its storage in the ambient D-DMM (Workman et al., 2006). A 1D diffusion model was used to calculate the H_2O/Ce of an E-DMM within a semi-infinite ambient D-DMM as a function of its residence time and length-scale (Fig. 19). The initial H_2O content for E-DMM (660 ppm) and D-DMM (59 ppm) are used in the two-component mantle melting mixing model (Section 5.4). We assume that the average temperature of the E-DMM is 1453 °C during its residence time (temperature at the mid-depth of the upper mantle assuming 0.5 °C/km mantle adiabat (McKenzie and Bickle, 1988) and potential temperature of 1350 °C (Ita and Stixrude, 1992)). Diffusivity of H^+ in the D-DMM and E-DMM is assumed to be the same. We assume olivine controls the H^+ diffusivity, and consider two H^+ diffusion mechanisms charge compensated by (1) flux of polarons-electrons in olivine (average diffusivity of $5.73 \times 10^{-9} \text{ m}^2/\text{s}$), and (2) diffusion of intrinsic point defects such as metal vacancy in olivine (average H diffusivity of $1.20 \times 10^{-9} \text{ m}^2/\text{s}$) (Kohlstedt and Mackwell, 1998). Diffusivity of Ce in clinopyroxene is slow (Van Orman

et al., 2001) compared to H^+ , so the Ce concentration in the E-DMM is assumed to be constant. The model produces a range of H_2O/Ce from ~ 350 to as low as 150 depending on the length-scale and residence time of the E-DMM (Fig. 19). Based on the mantle pseudo-isochron of Donnelly et al. (2004) the estimated residence time of the Pacific mantle E-DMM is ~ 300 Ma, and thus, the mantle length-scale would range from ~ 2 to 25 km to reproduce the observed range in H_2O/Ce observed in EMORB. Although our simple diffusion model does not consider other mantle phases such as clinopyroxene, which could decrease the hydrogen bulk diffusivity (Zhang and Liu, 2012), our model does not consider faster grain boundary diffusion of H^+ either, thus providing a simple but robust model. The observation of both low H_2O/Ce EMORB samples and high H_2O/Ce EMORB samples in all three sample locations (QDG TF, NEPR seamounts, and Macquarie Island) supports the hypothesis that the variation in the H_2O/Ce of these samples is due to a diffusion process rather than a mantle source variation.

Another possible cause of the range in H_2O/Ce is diffusive H^+ loss from the EMORB melts as it percolates through the D-DMM beneath the ridge. The E-DMM, enriched in volatile and trace elements, starts to melt deeper relative to the D-DMM (e.g. Green, 1976; Asimow and Langmuir, 2003; Asimow et al., 2004). Since the H_2O concentration gradient between the EMORB melts and the surrounding D-DMM is large, the diffusive loss of H^+ from the EMORB melt may be significant. Kogiso et al. (2004) modeled this melt-solid diffusion process for Fe, Mg and Os to constrain the length scale of heterogeneity in the MORB mantle. This 1D model is applied here to H^+ diffusion to estimate the minimum length scale of a partially molten E-DMM that can preserve its primary melt H_2O content. The model calculates two important time-scales. The first time-scale is the 1D diffusion time-scale, which is

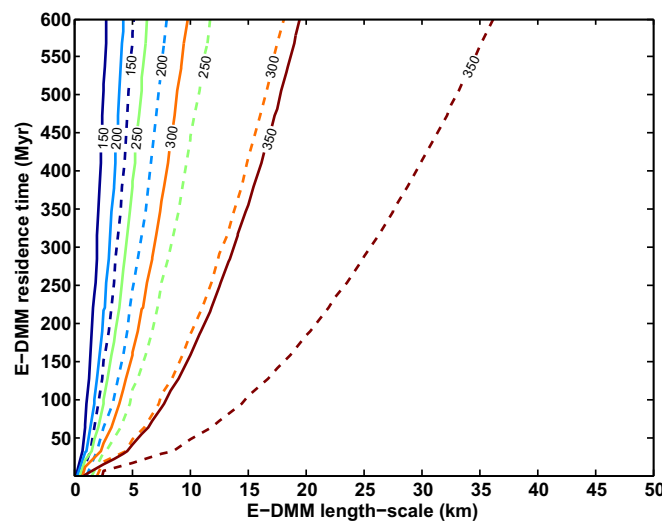


Fig. 19. Contour plot of H_2O/Ce of the E-DMM as a function of length-scale and residence time. The model is a 1D diffusion model of an E-DMM within a semi-infinite ambient D-DMM. The solid contour lines are the results (H_2O/Ce ratio of the E-DMM) for which H diffusion is charge-compensated by the diffusion of intrinsic point defects such as metal vacancy, and the dashed contour lines are the results where it is charge compensated by flux of polarons-electrons Kohlstedt and Mackwell (1998).

Table 3
Parameters used in the H⁺ diffusion model.

Parameter	Value	Description
ϕ	0.01	Porosity
D_{ol}^a	2.97×10^{-9}	Diffusivity of H ⁺ in olivine (m ² /s)
D_m^b	8.13×10^{-5}	Diffusivity of H ⁺ in melt (m ² /s)
D_{eff}^c	4.80×10^{-5}	Effective diffusivity of H ⁺ in a partially molten E-DMM (m ² /s)
K_{bulk}^d	0.007	Bulk partition coefficient of H ₂ O between solid and melt
dF/dz^e	0.0333	Melt production rate of peridotite assuming 1 kbar = 3 km (%/km)
dz/dt	0.1	EPR mantle upwelling rate (m/yr)
$\zeta + 4/3\eta$	$10^{18f,g}$	Viscosity of EDMM solid matrix (Pa s)
η	$1^{g,h}$	Viscosity of EDMM partial melt (Pa s)
ρ_m	3300	Density of EDMM solid (kg/m ³)
ρ_s	2800	Density of EDMM melt (kg/m ³)
k_ϕ	$a^2\phi^2/3000^i$	Permeability (m ²)
a	0.001	Grain size (m)
g	10	Acceleration due to gravity (m/s ²)

^a Kohlstedt and Mackwell (1998), $T = 1673$ K. Average diffusivity of H⁺ charge compensated by a flux of polarons-electrons in olivine.

^b Zhang et al. (2007), $T = 1673$ K, 1 wt% H₂O.

^c Eq. (A12) from Lee (1995).

^d Hauri et al. (2006).

^e Asimow et al. (2004) (0.1%/kbar).

^f Jin et al. (2001).

^g McKenzie (1985).

^h Murase and McBirney (1973).

ⁱ McKenzie (2000).

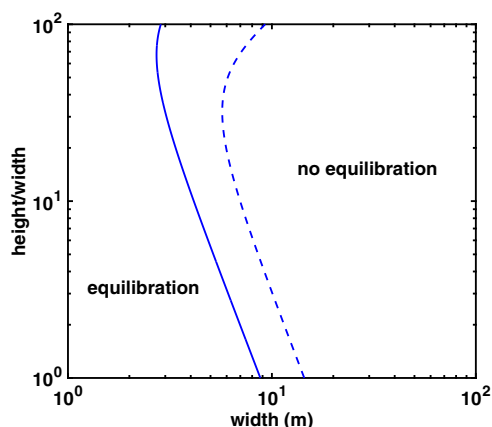


Fig. 20. Minimum length scale of the partially molten E-DMM required for the segregation and extraction of the melt to occur without significant diffusive H₂O (H⁺) loss. Partially molten E-DMM of aspect ratio (height/width) and width to the right of the blue lines will extract the melt without significant diffusive H₂O (H⁺) loss. The solid blue line is the result for which H⁺ diffusion is charge-compensated by the diffusion of intrinsic point defects such as metal vacancy, and the dashed line is the result where it is charge compensated by flux of polarons-electrons Kohlstedt and Mackwell (1998). For example, assuming the H⁺ diffusion is charge compensated by flux of polarons-electrons in olivine, the minimum length scale of a partially molten E-DMM with an aspect ratio of 1 is 14.8 m × 14.8 m. Parameters used for the model are given in Table 3. (For interpretation of the references to colour in this figure legend, the reader is referred to the web version of this article.)

the time required for the diffusing species, in this case H⁺ in the EMORB, to reach $e/(e+1) \sim 73\%$ of its equilibrium concentration with the surrounding D-DMM (i.e., that is attained at $T = \infty$). The second time-scale is the 1D melt

segregation time-scale, which is calculated using the compaction time (t_c) from the model of (McKenzie, 1984, 1985). This is the time required to reduce the mass of the melt by a factor of e (~ 2.718) in the partially molten region. If the melt segregation time-scale of the EMORB melt is shorter than its diffusion time-scale, the EMORB melt may be extracted from the partially molten E-DMM without significant diffusive loss of H₂O (H⁺). The values of the parameters used are shown in Table 3. The model result suggests that 14.4 m × 14.4 m (assuming an aspect ratio of melt height: width = 1:1 and H⁺ diffusion mechanism charge compensated by flux of polarons-electrons in olivine) is the estimated minimum length scale of the partially molten E-DMM required for the segregation and extraction of the melt to occur without significant diffusive loss of H⁺ (Fig. 20). The model results of using the H⁺ diffusivity charge compensated by diffusion of intrinsic point defects such as metal vacancy in olivine (Mackwell and Kohlstedt, 1990) requires a smaller length scale of 8.8 m × 8.8 m due to slower diffusivity of H⁺. These results may suggest that the large range in H₂O/Ce observed in our EMORB samples may be due to variable diffusive loss of H⁺ (H₂O) from the EMORB melt to the surrounding D-DMM as a result of variable partially molten E-DMM length scale. Alternatively diffusive loss of H⁺ (H₂O) from the EMORB melt to the surrounding mantle may occur shallower at mantle lithospheric depths, which may be responsible for the high H₂O contents observed in abyssal peridotites (Warren and Hauri, 2014).

Diffusive loss of H⁺ from the E-DMM and/or EMORB melt is also supported by the lack of other significant geochemical difference between the EMORB samples with different H₂O/Ce ratios. The process that produced the range in H₂O/Ce of the samples did not affect the other

volatile and trace element contents and ratios in the mantle nor the melt produced from it, consistent with diffusive fractionation of H₂O/Ce due to the much faster diffusivity of H⁺ compared to those of other elements.

5.5.6. Sulfur: melting-mixing model

The two-component mantle melting-mixing model, and the S concentration of D-DMM (100 ppm) and E-DMM (165 ppm) (Table 1 and Section 5.3) reproduces the range of S/Dy ratios in our DMORB and NMORB samples (Figs. 18c and S5c), but not the consistently low S/Dy ratios in the EMORB samples, in particular those from Macquarie Island. Instead, the model EMORB tend to have higher S/Dy due to both the effect of garnet and also the high SCSS calculated for H₂O rich model EMORB. Given the possibility of a lower H₂O E-DMM due to diffusive loss of H⁺ in solid state discussed in the previous section (Section 5.5.5), we ran our two component mantle melting-mixing model with an EDMM mantle that has a lower H₂O content of 264 ppm (calculated using H₂O/Ce ratio of 150 and Ce concentration of 1.65 ppm (Donnelly et al., 2004)). In this low H₂O model, the calculated EMORB with similar Th/La to those of the Macquarie Island samples (Th/La = 0.12–0.15) have relatively high S/Dy ratios (237 ± 99 (2σ)) that does not match those in the Macquarie Island samples (163 ± 49 (2σ)).

Alternatively, the Macquarie Island samples might have had higher initial S/Dy ratios, which subsequently decreased due to sulfide saturation induced by diffusive loss of H⁺ from the EMORB melts to the surrounding mantle as was discussed in the previous section. To test this hypothesis, we compared the measured sulfur content of the Macquarie Island samples to their calculated SCSS using the model of Fortin et al. (2015) and the measured H₂O content in the lavas at the P-T conditions along the melting path of EDMM from the AlphaMelts program (Ghiorso and Sack, 1995; Asimow and Ghiorso, 1998; Smith and Asimow, 2005; Antoshechkina et al., 2010). The result is that our samples never reached sulfide saturation in the mantle with our measured S and H₂O contents. Furthermore, our samples show a negative correlation between their measured S and H₂O concentrations (Fig. S6), which is opposite to those expected from sulfide saturation due to the diffusive loss of H, since experimental results show higher SCSS in melts with higher H₂O content (Fortin et al., 2015). There is a possibility that the existing models overestimate the SCSS of our samples since the model parameterization does not consider Cu and Ni content in the sulfides as discussed in Section 4.3.

Alternatively, degassing of S from the EMORB samples may explain their low S content and S/Dy ratios. Experimental data on the distribution of S between silicate melts and CO₂–H₂O fluids at relatively reducing conditions similar to MORB (Keppler, 2010; Lesne et al., 2011; Zajacz et al., 2012; Fiege et al., 2015) suggests that S will degas under those conditions. This hypothesis is supported by our samples showing a negative correlation between their measured S and H₂O concentrations (Fig. S6). Furthermore, Fe–Cu sulfides are found in CO₂-bearing bubbles decorating the bubble-glass interface in Macquarie Island

samples suggesting that S and Cu are soluble in CO₂ rich fluid (Kamenetsky and Eggin, 2012).

The S content of the E-DMM estimated in our model (165 ppm) is the least well-constrained mantle volatile content in this study. In addition to the potential overestimation of SCSS by the models and the effect of S degassing discussed above, S/Dy of our two component melting-mixing model is not very sensitive to the initial S content of the EDMM. This is shown by the similarity between the S/Dy of our original model mixture (Fig. 18c) and those calculated using 3 times higher E-DMM S content of 510 ppm (Fig. S7) (calculated assuming Pacific upper mantle S content of 190 ppm, D-DMM S content of 100 ppm, and 78% D-DMM (22% E-DMM) in the Pacific upper mantle). Therefore, the estimated S content of the E-DMM (165 ppm) is a minimum estimate in our two-component melting mixing model.

5.6. Volatile content of the MORB mantle and implications

We use the results of our two-component mantle melting-mixing model to estimate the volatile contents of the Pacific upper mantle. Using the proportions of D-DMM (78%) and E-DMM (22%) and their estimated volatile element contents, we calculate the volatile element content of Pacific upper mantle as follows: CO₂ = 235 ppm, H₂O = 191 ppm, F = 13 ppm, Cl = 5 ppm, and S = 114 ppm (Table 1). This weighted average volatile content using the proportions of the two mantle components is within the range of the previous estimates made for the upper mantle volatile content (Fig. 21a and Table 4) (Schilling et al., 1980; Michael, 1988; Javoy and Pineau, 1991; Sobolev and Chaussidon, 1996; Marty and Tolstikhin, 1998; Dixon et al., 2002; Saal et al., 2002; Salters and Stracke, 2004; Bézoz et al., 2005; Workman and Hart, 2005; le Roux et al., 2006; Hirschmann and Dasgupta, 2009; Beyer et al., 2012; Marty, 2012; Halliday, 2013; Le Voyer et al., 2015).

The estimated volatile and refractory ITE content for the E-DMM relative to the D-DMM decreases as a function of increasing elemental peridotite-basaltic melt bulk partition coefficient (Fig. 21b), suggesting that the two sources can be related by a single melting event. One hypothesis for the origin of the E-DMM is the presence of recycled oceanic crust in the MORB source (e.g. Hirschmann and Stolper, 1996; Sobolev et al., 2007), and the higher C content of the EMORB relative to the NMORB has been ascribed to recycling of C (e.g. Marty and Zimmermann, 1999). However, dehydration of subducting oceanic crust alters its volatile and fluid mobile element abundances. For example, dehydration releases Cl from the subducting oceanic crust more efficiently than C (Wallace, 2005). Thus, a recycled oceanic crust should have characteristically higher CO₂/Cl ratio relative to D-DMM. Contrary to this prediction, the E-DMM and D-DMM have a relatively constant CO₂/Cl ratio of ~57 (Section 5.3). An alternative proposed hypothesis for the origin of the E-DMM is metasomatism of the oceanic mantle lithosphere by a low degree mantle melt (Niu et al., 2002). In this scenario, the metasomatized oceanic lithosphere will have

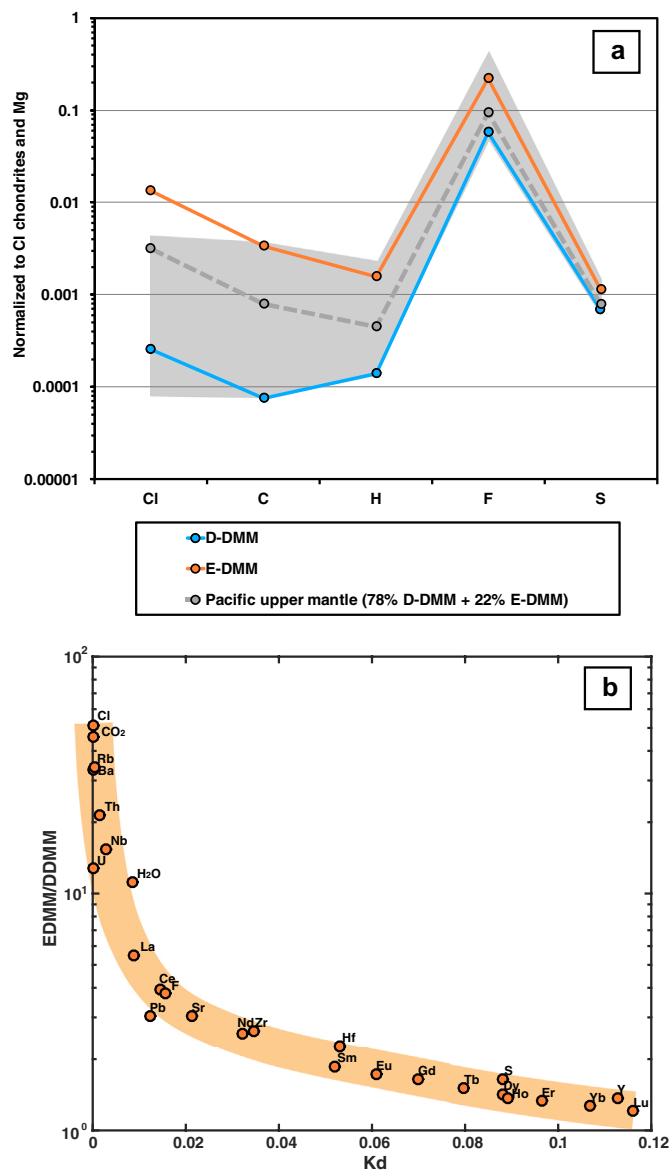


Fig. 21. (a) Carbonaceous chondrite normalized volatile element abundance in the D-DMM, E-DMM, and the Pacific upper mantle assuming 78% D-DMM and 22% E-DMM. The gray field is defined by the maximum and minimum estimates of the upper mantle volatile content from previous studies (Table 4) Schilling et al. (1980), Michael (1988), Javoy and Pineau (1991), Sobolev and Chaussidon (1996), Marty and Tolstikhin (1998), Dixon et al. (2002), Saal et al. (2002), Salters and Stracke (2004), Bézou et al. (2005), Workman and Hart (2005), le Roux et al. (2006) Hirschmann and Dasgupta (2009), Beyer et al. (2012), Marty (2012), Halliday (2013) and Le Voyer et al. (2015). The carbonaceous chondrite composition is from Anders and Grevesse (1989). (b) D-DMM normalized refractory and volatile element abundance of the E-DMM versus the element's bulk peridotite-basaltic melt partition coefficient. The abundances of elements in E-DMM relative to the D-DMM decreases as a function of increasing elemental peridotite-basaltic melt bulk partition coefficient, suggesting that the two sources can be related by a single melting event. The refractory trace element composition of D-DMM and E-DMM were taken from Workman and Hart (2005) from Donnelly et al. (2004), respectively and the volatile contents are from this study. Refractory trace and volatile element mineral-melt partition coefficient are from Kelemen et al. (2003), Hauri et al. (2006) and Rosenthal et al. (2015). Dy partition coefficient was used for the S partition coefficient since S behaves as a relatively compatible element during sulfide saturated E-DMM mantle melting (Fig. 18c). The mineral assemblage of the peridotite (55.2% olivine, 25.1% opx, 16.0% cpx, 3.6% spinel) is from pHMELTS model Ghiorso et al. (2002), Asimow et al. (2004) for the D-DMM.

volatile and ITE element abundance pattern related to the D-DMM and E-DMM by simple melting, and this pattern will not largely change as they are protected from the dehydration process during recycling back to the mantle at subduction zones. Therefore, the origin of the E-DMM

as a recycled oceanic lithosphere metasomatized by low degree melts (Niu et al., 2002) is a process that is consistent with the observation that (1) the E-DMM and D-DMM have a relatively constant CO₂/Cl ratio of ~57 (Section 4.3), and that (2) the volatile and refractory ITE for the E-DMM

Table 4

Comparison of our estimated volatile element composition of D-DMM, E-DMM, Pacific upper mantle, and upper mantle to previous estimates.

Reference	Mantle source	CO ₂ (ppm)	Cl (ppm)	H ₂ O (ppm)	F (ppm)	S (ppm)
This study	D-DMM	22	0.4	59	8	100
This study	E-DMM	990	22	660	31	165
This study	Pacific upper mantle (78% D-DMM + 22% E-DMM)	235	5	191	13	114
Schilling et al. (1980)	Large ion lithophile element depleted asthenosphere	–	7.3	–	65	–
Javoy and Pineau (1991)	Upper mantle	1100	–	–	–	–
Michael (1988)	Incompatible-element-depleted upper mantle	–	–	140 ± 40	–	–
Michael (1988)	Incompatible-element enriched upper mantle	–	–	350 ± 100	–	–
Sobolev and Chaussidon (1996)	Depleted MORB mantle source	–	–	80–330	–	–
Sobolev and Chaussidon (1996)	T-MORB mantle source	–	–	190–290	–	–
Sobolev and Chaussidon (1996)	E-MORB mantle source	–	–	200–950	–	–
Marty and Tolstikhin (1998)	Upper mantle	136 ± 83	–	–	–	–
Marty and Tolstikhin (1998)	EMORB type upper mantle	198 ± 140	–	–	–	–
Dixon et al. (2002)	DMM	–	–	100	–	–
Saal et al. (2002)	MORB mantle source	72 ± 19	1 ± 0.5	142 ± 85	16 ± 3	146 ± 35
Salters and Stracke (2004)	Depleted mantle	50.3 ± 12	0.51 ± 0.09	116 ± 58	11 ± 4.5	119 ± 30
Workman and Hart (2005)	DMM	36 ± 12	0.38 ± 0.25	70–160	–	–
Bézos et al. (2005)	Depleted mantle source	–	–	–	–	190 ± 40
Le Roux et al. (2006)	MORB mantle	–	5 ± 1	128 ± 5	17 ± 1	129 ± 6
Hirschmann and Dasgupta (2009)	DMM	60 ± 35	–	110 ± 55	–	–
Beyer et al. (2012)	Depleted MORB mantle	–	–	–	12	–
Marty (2012)	Depleted mantle	73 ± 29	–	150 ± 50	–	–
Halliday (2013)	Earth mantle (Model 3 – Basaltic glass)	163 ± 76	–	300 ± 100	–	–
Le Voyer et al. (2015)	DMM	–	1	110	12	–

relative to the D-DMM simply decreases as a function of increasing elemental peridotite-basaltic melt bulk partition coefficient (Fig. 21b).

6. CONCLUSION

We have reported major, trace, and volatile element (CO₂, H₂O, F, Cl, S) data as well as Sr, Nd, and Pb isotope composition of MORB glass samples from the Northern East Pacific Rise off-axis seamounts, Quebrada-Discovery-GoFar transform fault system, and Macquarie Island. The incompatible trace element (ITE) pattern of the samples range from highly depleted (DMORB, Th/La ≤ 0.035) to enriched (EMORB, Th/La ≥ 0.07), and the isotopic composition spans the entire range observed in EPR MORB.

At the time of melt generation, the source that generated the EMORB was essentially peridotitic. The variable incompatible trace element ratios (e.g. Th/La) of basalts

with Sr, Nd and Pb isotope ratios similar to E-DMM suggests that the E-DMM melted incrementally without the aggregation of the different melt fractions. The identical major and trace elements composition of DMORB generated from both E-DMM and D-DMM, suggest that the E-DMM is a peridotitic source.

NMORB might represent mixing of melts from a two-component mantle (D-DMM and E-DMM), rather than an actual DMM mantle source. This is consistent with the similar frequency distribution of Nd isotopes generated from clinopyroxene from abyssal peridotites (at the centimeter spatial scale) and lavas from the QDG transform fault and NEPR seamounts. These observations when considered together with the observed correlations between crustal thickness and extent of magma aggregation and differentiation (Pickle et al., 2009) strongly suggest that the NMORB might represent mixing of melts from a two-component D-DMM and E-DMM rather than melting an actual DMM mantle source.

After filtering the volatile data for secondary processes (volatile degassing, sulfide saturation, assimilation of seawater-derived component, and fractional crystallization), we use the volatile to trace element ratios of our samples and a two-component mantle melting-mixing model to estimate the volatile content of D-DMM ($\text{CO}_2 = 22$ ppm, $\text{H}_2\text{O} = 59$ ppm, $\text{F} = 8$ ppm, $\text{Cl} = 0.4$ ppm, and $\text{S} = 100$ ppm) and of the E-DMM ($\text{CO}_2 = 990$ ppm, $\text{H}_2\text{O} = 660$ ppm, $\text{F} = 31$ ppm, $\text{Cl} = 22$ ppm, and $\text{S} = 165$ ppm). A particularly important observation is the fairly constant CO_2/Cl ratio of $\sim 57 \pm 8$ in the D-DMM and E-DMM, which is difficult to reconcile with a recycled oceanic crust origin of E-DMM. Recycled oceanic mantle lithosphere metasomatized by a low degree mantle melt is a more consistent hypothesis with the observation.

Our two-component mantle melting-mixing model reproduces the trace, volatile element contents, and isotopic composition of our samples, in particular the kernel density estimates (KDE) of Th/La and $^{143}\text{Nd}/^{144}\text{Nd}$ isotopic composition of our samples and axial MORB data compiled from the literature. Moreover, our model suggests that the melts produced during variable degrees of melting of the E-DMM controls most of the MORB geochemical variation.

The parameters of the model required to match the observation suggests that (1) 78% of the upper mantle is highly depleted in volatile and refractory ITE (D-DMM) and 22% is enriched in volatile and refractory ITE (E-DMM), and (2) a fraction (~ 65 to 80%) of the low degree EMORB melts ($\sim 1.3\%$) may escape melt aggregation by freezing at the base of the oceanic lithosphere significantly enriching it in volatile and trace elements, consistent with proposed geodynamical processes acting at mid-ocean ridges and with the generation and composition of the E-DMM.

Our two-component mantle melting-mixing model allows us to make the following statements. (1) The estimated primitive CO_2 content (955 ppm) of the average oceanic crust suggests a CO_2 flux from the ridge of 1.32×10^{12} mol yr^{-1} or 58 Mt yr^{-1} . (2) The Cl/K ratio for uncontaminated DMORB and NMORB may be higher than previously defined due to mixing of fractional melts of E-DMM and D-DMM. (3) The large range in F/Nd (14.3–45.4) of our samples is due to variation in the mantle source F/Nd ratio and also the significant fractionation of F/Nd during melting of garnet peridotite. (4) The negative correlation between S and H_2O content of our samples along with the failure of our model to reproduce the negative correlation between S/Dy and Th/La ratios of our samples suggests either the model of Fortin et al. (2015) might be overestimating the SCSS of our samples or our samples might have lost S due to some process other than sulfide saturation, such as S partitioning into the CO_2 – H_2O phase during degassing. (5) Our model does not reproduce the large range in $\text{H}_2\text{O}/\text{Ce}$ (150–400) of EMORB samples, indicating variable amounts of diffusive loss of H^+ from the E-DMM to the ambient D-DMM, or from the EMORB during percolation through the surrounding D-DMM. (6) The volatile and refractory ITE abundances in E-DMM normalized to D-DMM decreases as a function of increas-

ing peridotite-basaltic melt bulk partition coefficient suggesting the two sources can be related by a single melting event. This observation and the relatively constant CO_2/Cl ratio of $\sim 57 \pm 8$ for the E-DMM and D-DMM is consistent with the origin of the E-DMM as a recycled oceanic lithosphere metasomatized by low degree melts.

Using the proportion of D-DMM of 78% and E-DMM of 22% and the estimated D-DMM and E-DMM volatile element contents, we calculate the volatile element content of Pacific upper mantle ($\text{CO}_2 = 235$ ppm, $\text{H}_2\text{O} = 191$ ppm, $\text{F} = 13$ ppm, $\text{Cl} = 5$ ppm, and $\text{S} = 114$ ppm). The volatile element budget of the Pacific upper mantle presented in this paper provides a fundamental constraint to establish the origin and evolution of the volatile element budget in the Earth.

ACKNOWLEDGEMENTS

We would like to thank the crew of the R/V Knorr in mapping and sample collection. We thank Joe Devine and Joe Boesenberg for his assistance with EMP analyses, Soumen Mallick for his assistance with the LA-ICP-MS and isotope measurements, and Jianhua Wang for his assistance with the SIMS analyses. Michael Perfit, Jacqueline Dixon, John Rudge, and an anonymous reviewer are thanked for their constructive reviews and Marc Norman and Janne Blichert-Toft are thanked for editorial handling. This study was supported by NSF-OCE 0962195 and 1355932 awarded to A.E.S.

APPENDIX A. SUPPLEMENTARY DATA

Supplementary data associated with this article can be found, in the online version, at <http://dx.doi.org/10.1016/j.gca.2015.10.033>.

APPENDIX B. MAJOR ELEMENT CORRECTION FOR FRACTIONAL CRYSTALLIZATION

The major element composition of primitive melts provide useful information for estimating the mantle source lithology of the heterogeneous Earth's upper mantle. However, most MORB are not primitive melts since they experience variable degrees of fractional crystallization affecting the major element composition of the melts. Therefore, the major element composition of MORB must be corrected for fractional crystallization before interpreting them to infer mantle source lithology.

Previous method to correct the major element composition of MORB for fractional crystallization by Niu et al. (1999) assumes a single liquid line of descent (LLD) for melts that ranges from DMORB to EMORB. This assumption may lead to erroneous fractional crystallization correction since EMORB and DMORB have different LLDs due to the higher H_2O content in EMORB compared to DMORB (Danyushevsky, 2001; Michael and Chase, 1987). Thus, the correlation between the estimated primitive melt major element composition and their isotopic composition observed by Niu et al. (1999) (Fig. S3) may be an artifact of the fractional crystallization correction.

To take into account the different H₂O content of the samples, we fit a polynomial function to the LLDs calculated for DMORB (H₂O poor) and EMORB (H₂O rich) in Section 4.4, and use these functions to correct the major element composition of samples for fractional crystallization to an Mg# of 72. We only correct the major element composition of DMORB and EMORB samples with Mg# higher than 60 using their respective LLDs to avoid the complicating effect of melt mixing in the more evolved samples and in the NMORB. Furthermore, we only use samples from NEPR seamounts in order to make direct comparison between the results of our method and those of Niu et al. (1999). The estimated primitive major element composition of the DMORB and EMORB samples from NEPR seamounts are plotted against their isotopic composition (Fig. S3), and are compared to those estimated by the method of Niu et al. (1999). The estimated primitive EMORB melt using our method is higher in FeO, Na₂O, TiO₂, and K₂O, while lower in Al₂O₃ and CaO compared to estimated primitive DMORB; more importantly our trends for FeO and Al₂O₃ are opposite to those using the method of Niu et al. (1999). Niu et al. (1999) interpreted the low FeO and high Al₂O₃ of their estimated primitive EMORB to be consistent with low F melt of peridotite at relatively low pressure (10 kbar) (Baker et al., 1995), but their trends are most likely an artifact of not taking into account the effect of H₂O content on the delay of plagioclase saturation in EMORB. Instead, the lower Al₂O₃ and CaO and higher FeO content in the primitive EMORB estimated using our method is consistent with melting of the E-DMM in the garnet stability at higher pressure than the D-DMM, consistent with experimental melt composition of garnet peridotite (Walter, 1998) having lower Al₂O₃ and CaO and higher FeO content compared to spinel peridotite (Wasylenski et al., 2003). Therefore the estimated primitive EMORB major element composition is consistent with melting of E-DMM in the garnet stability field at high pressure.

APPENDIX C. TWO-COMPONENT MANTLE MELTING-MIXING MODEL

The incremental near fractional melts from the D-DMM and E-DMM were calculated using pHMELTS (Asimow et al., 2004; Ghiorso et al., 2002; Smith and Asimow, 2005) and are mixed following the method of Rudge et al. (2013). Here we briefly describe the mixing method. We calculate 2000 weighted averages of the compositions of the individual fractional melts,

$$\hat{C} = \sum_{j=1}^m \sum_{i=1}^{n_j} \hat{r}_j c_j^i, \quad (1)$$

where c_j^i are concentrations of the i th fractional melt of the j th mantle source, and \hat{r}_j are random weights assigned for the i th fractional melt of the j th mantle source that has an expected value that takes into account the triangular geometry of the melting region and the masses of the individual incremental melts. Specifically for our case, the equation can be written as,

$$\hat{C} = \sum_{i=1}^{n_{DMORB}} \hat{r}_{DMORB}^i c_{DMORB}^i + \sum_{i=1}^{n_{EMORB}} \hat{r}_{EMORB}^i c_{EMORB}^i \quad (2)$$

where c_{DMORB}^i and c_{EMORB}^i are i th fractional melts of the D-DMM and E-DMM, and \hat{r}_{DMORB}^i and \hat{r}_{EMORB}^i are the randomly chosen weights that satisfy the conditions,

$$\hat{r}_{DMORB}^i \geq 0, \hat{r}_{EMORB}^i \geq 0, \quad (3)$$

$$\sum_{i=1}^{n_{DMORB}} \hat{r}_{DMORB}^i + \sum_{i=1}^{n_{EMORB}} \hat{r}_{EMORB}^i = 1, \quad (4)$$

$$E(\hat{r}_{DMORB}^i) = f_{DMORB} \tilde{\omega}_{DMORB}^i, \quad (5)$$

$$E(\hat{r}_{EMORB}^i) = f_{EMORB} \tilde{\omega}_{EMORB}^i, \quad (6)$$

where f_{DMORB} and (where $f_{EMORB} = 1 - f_{DMORB}$) are the average fraction of D-DMM and E-DMM melts that makes up the model melts, $\tilde{\omega}_{DMORB}^i$ and $\tilde{\omega}_{EMORB}^i$ are normalized weights, and $E(\hat{r}_{DMORB}^i)$ and $E(\hat{r}_{EMORB}^i)$ are the expected values of \hat{r}_{DMORB}^i and \hat{r}_{EMORB}^i . The normalized weights $\tilde{\omega}_{DMORB}^i$ and $\tilde{\omega}_{EMORB}^i$ are normalized melt generation depth from the top of the melting region calculated for a triangle with a 45° angle from horizontal to the melting regime boundary. The fractions f_{DMORB} and f_{EMORB} are given by,

$$f_{DMORB} = \frac{P_{DDMM} \sum_{i=1}^{n_{DMORB}} \omega_{DMORB}^i}{P_{DDMM} \sum_{i=1}^{n_{DMORB}} \omega_{DMORB}^i + P_{EDMM} \sum_{i=1}^{n_{EMORB}} \omega_{EMORB}^i} \quad (7)$$

$$f_{EMORB} = \frac{P_{EDMM} \sum_{i=1}^{n_{EMORB}} \omega_{EMORB}^i}{P_{DDMM} \sum_{i=1}^{n_{DMORB}} \omega_{DMORB}^i + P_{EDMM} \sum_{i=1}^{n_{EMORB}} \omega_{EMORB}^i} \quad (8)$$

where p_{DDMM} and p_{EDMM} (where $p_{EDMM} = 1 - p_{DDMM}$) are the solid fractions of D-DMM and E-DMM in the Pacific upper mantle, ω_{DMORB}^i and ω_{EMORB}^i are melt generation depth from the top of the melting region. The random weights \hat{r}_{DMORB}^i and \hat{r}_{EMORB}^i are distributed as a Dirichlet distribution with parameters $\alpha_{DMORB}^{n_{DMORB}}$ and $\alpha_{EMORB}^{n_{EMORB}}$ given by,

$$\{\hat{r}_{DMORB}^1, \dots, \hat{r}_{DMORB}^{n_{DMORB}}, \hat{r}_{EMORB}^1, \dots, \hat{r}_{EMORB}^{n_{EMORB}}\} \sim Dir(\alpha_{DMORB}^1, \dots, \alpha_{DMORB}^{n_{DMORB}}, \alpha_{EMORB}^1, \dots, \alpha_{EMORB}^{n_{EMORB}}), \quad (9)$$

$$\alpha_{DMORB}^{n_{DMORB}} = (N - 1) f_{DMORB} \tilde{\omega}_{DMORB}^i, \quad (10)$$

$$\alpha_{EMORB}^{n_{EMORB}} = (N - 1) f_{EMORB} \tilde{\omega}_{EMORB}^i, \quad (11)$$

where N is the mixing parameter that controls the amount of mixing between the melts. $N = 1$ means no mixing while $N = \infty$ means complete mixing.

APPENDIX D. REASON FOR WHY WE DID NOT ATTEMPT TO REPRODUCE THE MACQUARIE ISLAND SAMPLES USING OUR MODEL

The samples from Macquarie Island are distinctly enriched compared to the other ridge settings (Figs. 2a and 3c). This enriched composition can be reproduced mostly by low degree EMORB melts ($F = 0.5$ – 0.7%) that hardly mix with DMORB (0–30%); consistent with the tectonic origin of the Macquarie Island (Kamenetsky et al., 2000). Macquarie Island represents a transition from an extensional environment forming a mid-ocean ridge to transpressional conditions that tectonically uplifted it

5~10 Ma ago (e.g. Christodoulou et al., 1984; Goscombe and Everard, 1998; Johnson and Molnar, 1972; Ruff et al., 1989; Varne et al., 2000; Varne et al., 1969). During the last stages of spreading (5–10 Ma) the transpression produced a gradual shut off of the magmatism. During the shutting off of the magmatism the low degree melts from the E-DMM are most likely the last melts extracted at the sea floor. The eruption age of Macquarie Island lavas coincides with that of the tectonic uplift of the island (Duncan and Varne, 1988), supporting such an interpretation. Hence, the Macquarie Island samples are most likely the last melts from a E-DMM that were extracted at the surface after the shut off of the ridge magmatism; and therefore, it made no sense to reproduce the KDE of these samples using our mixing model.

REFERENCES

- Anders E. and Grevesse N. (1989) Abundances of the elements – Meteoritic and solar. *Geochim. Cosmochim. Acta* **53**, 197–214.
- Anderson D. L. and Spetzler H. (1970) Partial melting and the low-velocity zone. *Phys. Earth Planet. Int.* **4**, 62–64.
- Antoshechkina P., Asimow P., Hauri E. and Luffi P. (2010) Effect of water on mantle melting and magma differentiation, as modeled using *Adiabat_1ph 3.0*, AGU Fall Meeting Abstracts, p. 2264.
- Ariskin A. A., Danyushevsky L. V., Bychkov K. A., McNeill A. W., Barmina G. S. and Nikolaev G. S. (2013) Modeling solubility of Fe–Ni sulfides in basaltic magmas: the effect of nickel. *Econ. Geol.* **108**, 1983–2003.
- Asimow P. D., Dixon J. and Langmuir C. (2004) A hydrous melting and fractionation model for mid-ocean ridge basalts: application to the Mid-Atlantic Ridge near the Azores. *Geochem. Geophys. Geosyst.* **5**.
- Asimow P. D. and Ghiorso M. S. (1998) Algorithmic modifications extending MELTS to calculate subsolidus phase relations. *Am. Mineral.* **83**, 1127–1132.
- Asimow P. D. and Langmuir C. H. (2003) The importance of water to oceanic mantle melting regimes. *Nature* **421**, 815–820.
- Baker M., Hirschmann M., Ghiorso M. and Stolper E. (1995) Compositions of near-solidus peridotite melts from experiments and thermodynamic calculations. *Nature* **375**, 308–311.
- Batiza R. and Niu Y. L. (1992) Petrology and magma chamber processes at the East Pacific Rise~9°30'N. *J. Geophys. Res.* **97**, 6779–6797.
- Batiza R., Niu Y. L. and Zayac W. C. (1990) Chemistry of Seamounts near the East Pacific Rise – implications for the Geometry of Subaxial Mantle Flow. *Geology* **18**, 1122–1125.
- Beyer C., Klemme S., Wiedenbeck M., Stracke A. and Vollmer C. (2012) Fluorine in nominally fluorine-free mantle minerals: experimental partitioning of F between olivine, orthopyroxene and silicate melts with implications for magmatic processes. *Earth Planet. Sci. Lett.* **337**, 1–9.
- Bézos A., Lorand J.-P., Humler E. and Gros M. (2005) Platinum-group element systematics in Mid-Oceanic Ridge basaltic glasses from the Pacific, Atlantic, and Indian Oceans. *Geochim. Cosmochim. Acta* **69**, 2613–2627.
- Bindeman I., Kamenetsky V., Palandri J. and Vennemann T. (2012) Hydrogen and oxygen isotope behaviors during variable degrees of upper mantle melting: Example from the basaltic glasses from Macquarie Island. *Chem. Geol.* **310**, 126–136.
- Bindeman I. N., Davis A. M. and Drake M. J. (1998) Ion microprobe study of plagioclase-basalt partition experiments at natural concentration levels of trace elements. *Geochim. Cosmochim. Acta* **62**, 1175–1193.
- Blundy J. and Wood B. (1994) Prediction of crystal melt partition coefficients from elastic moduli. *Nature* **372**, 452–454.
- Brandl P. A., Beier C., Regelous M., Abouchami W., Haase K. M., Garbe-Schönberg D. and Galer S. J. (2012) Volcanism on the flanks of the East Pacific Rise: quantitative constraints on mantle heterogeneity and melting processes. *Chem. Geol.* **298**, 41–56.
- Carbotte S. M., Small C. and Donnelly K. (2004) The influence of ridge migration on the magmatic segmentation of mid-ocean ridges. *Nature* **429**, 743–746.
- Carlson R. and Raskin G. (1984) Density of the ocean crust. *Nature* **311**, 555–558.
- Carroll M. R. and Webster J. D. (1994) Solubilities of sulfur, noble-gases, nitrogen, chlorine, and fluorine in magmas. *Rev. Mineral.* **30**, 231–279.
- Cartigny P., Pineau F., Aubaud C. and Javoy M. (2008) Towards a consistent mantle carbon flux estimate: insights from volatile systematics (H₂O/Ce, δD, CO₂/Nb) in the North Atlantic mantle (14°N and 34°N). *Earth Planet. Sci. Lett.* **265**, 672–685.
- Chaussidon M., Albarède F. and Sheppard S. M. (1989) Sulphur isotope variations in the mantle from ion microprobe analyses of micro-sulphide inclusions. *Earth Planet. Sci. Lett.* **92**, 144–156.
- Christodoulou C., Griffin B. J. and Foden J. (1984) The geology of Macquarie Island. *ANARE Res. Note* **21**, 1–15.
- Clog M., Aubaud C., Cartigny P. and Dosso L. (2013) The hydrogen isotopic composition and water content of southern Pacific MORB: a reassessment of the D/H ratio of the depleted mantle reservoir. *Earth Planet. Sci. Lett.* **381**, 156–165.
- Cooper K. M., Eiler J. M., Asimow P. D. and Langmuir C. H. (2004) Oxygen isotope evidence for the origin of enriched mantle beneath the mid-Atlantic ridge. *Earth Planet. Sci. Lett.* **220**, 297–316.
- Cottrell E. and Kelley K. A. (2011) The oxidation state of Fe in MORB glasses and the oxygen fugacity of the upper mantle. *Earth Planet. Sci. Lett.* **305**, 270–282.
- Crisp J. A. (1984) Rates of magma emplacement and volcanic output. *J. Volcanol. Geotherm. Res.* **20**, 177–211.
- Danyushevsky L. V. (2001) The effect of small amounts of H₂O crystallisation of mid-ocean ridge and backarc basin magmas. *J. Volcanol. Geotherm. Res.* **110**, 265–280.
- Danyushevsky L. V., Eggins S. M., Falloon T. J. and Christie D. M. (2000) H₂O abundance in depleted to moderately enriched mid-ocean ridge magmas; Part I: incompatible behaviour, implications for mantle storage, and origin of regional variations. *J. Petrol.* **41**, 1329–1364.
- Dasgupta R. and Hirschmann M. M. (2006) Melting in the Earth's deep upper mantle caused by carbon dioxide. *Nature* **440**, 659–662.
- Dasgupta R., Mallik A., Tsuno K., Withers A. C., Hirth G. and Hirschmann M. M. (2013) Carbon-dioxide-rich silicate melt in the Earth's upper mantle. *Nature* **493**, 211–U222.
- Dickinson J., Harb N., Portner R. and Daczko N. (2009) Glassy fragmental rocks of Macquarie Island (Southern Ocean): mechanism of formation and deposition. *Sediment. Geol.* **216**, 91–103.
- Dixon J. E. (1997) Degassing of alkalic basalts. *Am. Mineral.* **82**, 368–378.
- Dixon J. E., Leist L., Langmuir C. and Schilling J. G. (2002) Recycled dehydrated lithosphere observed in plume-influenced mid-ocean-ridge basalt. *Nature* **420**, 385–389.
- Dixon J. E. and Stolper E. M. (1995) An experimental study of water and carbon dioxide solubilities in mid-ocean ridge

- basaltic liquids. Part 2: applications to degassing. *J. Petrol.* **36**, 1633–1646.
- Dixon J. E., Stolper E. M. and Holloway J. R. (1995) An experimental study of water and carbon dioxide solubilities in mid ocean ridge basaltic liquids. Part 1: calibration and solubility models. *J. Petrol.* **36**, 1607–1631.
- Donnelly K. E., Goldstein S. L., Langmuir C. H. and Spiegelman M. (2004) Origin of enriched ocean ridge basalts and implications for mantle dynamics. *Earth Planet. Sci. Lett.* **226**, 347–366.
- Duncan R. A. and Varne R. (1988) The age and distribution of the igneous rocks of Macquarie Island. *Paper Proc. R. Soc. Tasmania* **122**, 45–50.
- Edmonds M., Gerlach T. M. and Herd R. A. (2009) Halogen degassing during ascent and eruption of water-poor basaltic magma. *Chem. Geol.* **263**, 122–130.
- Eiler J. M., Schiano P., Kitchen N. and Stolper E. M. (2000) Oxygen-isotope evidence for recycled crust in the sources of mid-ocean-ridge basalts. *Nature* **403**, 530–534.
- Evans R. L., Hirth G., Baba K., Forsyth D., Chave A. and Mackie R. (2005) Geophysical evidence from the MELT area for compositional controls on oceanic plates. *Nature* **437**, 249–252.
- Faul U. H. and Jackson I. (2005) The seismological signature of temperature and grain size variations in the upper mantle. *Earth Planet. Sci. Lett.* **234**, 119–134.
- Fiege A., Holtz F., Behrens H., Mandeville C. W., Shimizu N., Crede L. S. and Göttlicher J. (2015) Experimental investigation of the S and S-isotope distribution between H₂O–S ± Cl fluids and basaltic melts during decompression. *Chem. Geol.* **393**, 36–54.
- Filiberto J., Dasgupta R., Gross J. and Treiman A. H. (2014) Effect of chlorine on near-liquidus phase equilibria of an Fe–Mg-rich tholeiitic basalt. *Contrib. Mineral. Petrol.* **168**, 1–13.
- Filiberto J., Wood J., Dasgupta R., Shimizu N., Le L. and Treiman A. H. (2012) Effect of fluorine on near-liquidus phase equilibria of an Fe–Mg rich basalt. *Chem. Geol.* **312**, 118–126.
- Fornari D. J., Perfit M. R., Allan J. F. and Batiza R. (1988) Small-scale heterogeneities in depleted mantle sources: near-ridge seamount lava geochemistry and implications for mid-ocean-ridge magmatic processes. *Nature* **331**, 511–513.
- Forsyth D. W. (1975) The early structural evolution and anisotropy of the oceanic upper mantle. *Geophys. J. Int.* **43**, 103–162.
- Fortin M.-A., Riddle J., Desjardins-Langlais Y. and Baker D. R. (2015) The effect of water on the sulfur concentration at sulfide saturation (SCSS) in natural melts. *Geochim. Cosmochim. Acta* **160**, 100–116.
- Gaetani G. A. and Grove T. L. (1998) The influence of water on melting of mantle peridotite. *Contrib. Mineral. Petrol.* **131**, 323–346.
- Gale A., Dalton C. A., Langmuir C. H., Su Y. and Schilling J. G. (2013) The mean composition of ocean ridge basalts. *Geochem. Geophys. Geosyst.* **14**, 489–518.
- Ghiorso M. S., Hirschmann M. M., Reiners P. W. and Kress V. C. (2002) The pMELTS: a revision of MELTS for improved calculation of phase relations and major element partitioning related to partial melting of the mantle to 3 GPa. *Geochem. Geophys. Geosyst.* **3**, 1–35.
- Ghiorso M. S. and Sack R. O. (1995) Chemical mass-transfer in magmatic processes. 4. A revised and internally consistent thermodynamic model for the interpolation and extrapolation of liquid–solid equilibria in magmatic systems at elevated-temperatures and pressures. *Contrib. Mineral. Petrol.* **119**, 197–212.
- Goscombe B. D. and Everard J. L. (1998) Geology of Macquarie Island, sheets 1–7, Geological Atlas 1:10 000 series. Rosny Park: Tasmanian Geological Survey.
- Green D. H. (1976) Experimental testing of ‘equilibrium’ partial melting of a peridotite under water-saturated, high-pressure conditions. *Can. Mineral.* **14**, 255–268.
- Gregg P. M., Behn M. D., Lin J. and Grove T. L. (2009) Melt generation, crystallization, and extraction beneath segmented oceanic transform faults. *J. Geophys. Res.* **114**.
- Hall L., Mahoney J., Sinton J. and Duncan R. A. (2006) Spatial and temporal distribution of a C-like asthenospheric component in the Rano Rahi Seamount Field, East Pacific Rise, 15–19°S. *Geochem. Geophys. Geosyst.* **7**.
- Halliday A. N. (2013) The origins of volatiles in the terrestrial planets. *Geochim. Cosmochim. Acta* **105**, 146–171.
- Hauri E. (2002) SIMS analysis of volatiles in silicate glasses, 2: isotopes and abundances in Hawaiian melt inclusions. *Chem. Geol.* **183**, 115–141.
- Hauri E., Wang J. H., Dixon J. E., King P. L., Mandeville C. and Newman S. (2002) SIMS analysis of volatiles in silicate glasses: 1. Calibration, matrix effects and comparisons with FTIR. *Chem. Geol.* **183**, 99–114.
- Hauri E. H., Gaetani G. A. and Green T. H. (2006) Partitioning of water during melting of the Earth’s upper mantle at H₂O-undersaturated conditions. *Earth Planet. Sci. Lett.* **248**, 715–734.
- Havlin C., Parmentier E. and Hirth G. (2013) Dike propagation driven by melt accumulation at the lithosphere–asthenosphere boundary. *Earth Planet. Sci. Lett.* **376**, 20–28.
- Hebert L. B. and Montesi L. G. J. (2010) Generation of permeability barriers during melt extraction at mid-ocean ridges. *Geochem. Geophys. Geosyst.* **11**.
- Hebert L. B. and Montesi L. G. J. (2011) Melt extraction pathways at segmented oceanic ridges: application to the East Pacific Rise at the Siqueiros transform. *Geophys. Res. Lett.* **38**.
- Herzberg C. and Asimow P. D. (2008) Petrology of some oceanic island basalts: PRIMELT2.XLS software for primary magma calculation. *Geochem. Geophys. Geosyst.* **9**.
- Hirschmann M. M. and Dasgupta R. (2009) The H/C ratios of Earth’s near-surface and deep reservoirs, and consequences for deep Earth volatile cycles. *Chem. Geol.* **262**, 4–16.
- Hirschmann M. M. and Stolper E. M. (1996) A possible role for garnet pyroxenite in the origin of the “garnet signature” in MORB. *Contrib. Mineral. Petrol.* **124**, 185–208.
- Hirschmann M. M., Tenner T., Aubaud C. and Withers A. (2009) Dehydration melting of nominally anhydrous mantle: the primacy of partitioning. *Phys. Earth Planet. Int.* **176**, 54–68.
- Hirth G. and Kohlstedt D. L. (1996) Water in the oceanic upper mantle: implications for rheology, melt extraction and the evolution of the lithosphere. *Earth Planet. Sci. Lett.* **144**, 93–108.
- Holland H. D. (1984) *The Chemical Evolution of the Atmosphere and Oceans*. Princeton University Press.
- Ita J. and Stixrude L. (1992) Petrology, elasticity, and composition of the mantle transition zone. *J. Geophys. Res.* **97**, 6849–6866.
- Jacobsen S. D., Jiang F. M., Mao Z., Duffy T. S., Smyth J. R., Holl C. M. and Frost D. J. (2008) Effects of hydration on the elastic properties of olivine. *Geophys. Res. Lett.* **35**.
- Jarosewich E., Nelen J. and Norberg J. A. (1980) Reference samples for electron microprobe analysis. *Geostandard. Newslett.* **4**, 43–47.
- Javoy M. and Pineau F. (1991) The volatiles record of a popping rock from the mid-Atlantic Ridge at 14°N – chemical and isotopic composition of gas trapped in the vesicles. *Earth Planet. Sci. Lett.* **107**, 598–611.
- Javoy M., Pineau F. and Allegre C. J. (1982) Carbon geodynamic cycle. *Nature* **300**, 171–173.
- Jin Z.-M., Zhang J., Green H. and Jin S. (2001) Eclogite rheology: implications for subducted lithosphere. *Geology* **29**, 667–670.

- Johnson E. A. (2006) Water in nominally anhydrous crustal minerals: speciation, concentration, and geologic significance. *Rev. Mineral. Geochem.* **62**, 117–154.
- Johnson T. and Molnar P. (1972) Focal mechanisms and plate tectonics of Southwest Pacific. *J. Geophys. Res.* **77**, 5000–5032.
- Jung H. and Karato S. (2001) Water-induced fabric transitions in olivine. *Science* **293**, 1460–1463.
- Kamenetsky V., Davidson P., Mernagh T., Crawford A., Gemmill J., Portnyagin M. and Shinjo R. (2002) Fluid bubbles in melt inclusions and pillow-rim glasses: high-temperature precursors to hydrothermal fluids? *Chem. Geol.* **183**, 349–364.
- Kamenetsky V. S. and Eggins S. M. (2012) Systematics of metals, metalloids, and volatiles in MORB melts: effects of partial melting, crystal fractionation and degassing (a case study of Macquarie Island glasses). *Chem. Geol.* **302**, 76–86.
- Kamenetsky V. S., Everard J. L., Crawford A. J., Varne R., Eggins S. M. and Lanyon R. (2000) Enriched end-member of primitive MORB melts: petrology and geochemistry of glasses from Macquarie Island (SW Pacific). *J. Petrol.* **41**, 411–430.
- Kamenetsky V. S. and Maas R. (2002) Mantle-melt evolution (dynamic source) in the origin of a single MORB suite: a perspective from magnesian glasses of Macquarie Island. *J. Petrol.* **43**, 1909–1922.
- Karato S. I. (2012) On the origin of the asthenosphere. *Earth Planet. Sci. Lett.* **321**, 95–103.
- Karato S. I. and Jung H. (1998) Water, partial melting and the origin of the seismic low velocity and high attenuation zone in the upper mantle. *Earth Planet. Sci. Lett.* **157**, 193–207.
- Katz R. F. (2008) Magma dynamics with the enthalpy method: benchmark solutions and magmatic focusing at mid-ocean Ridges. *J. Petrol.* **49**, 2099–2121.
- Katz R. F. and Weatherley S. M. (2012) Consequences of mantle heterogeneity for melt extraction at mid-ocean ridges. *Earth Planet. Sci. Lett.* **335**, 226–237.
- Kelemen P. B., Yogodzinski G. M. and Scholl D. W. (2003) Along-strike variation in the Aleutian Island Arc: genesis of high Mg# andesite and implications for continental crust. *Inside Subduct. Factory*, 223–276.
- Kelley D. S. and Delaney J. R. (1987) Two-phase separation and fracturing in mid-ocean ridge gabbros at temperatures greater than 700 °C. *Earth Planet. Sci. Lett.* **83**, 53–66.
- Kendrick M. A., Kamenetsky V. S., Phillips D. and Honda M. (2012) Halogen systematics (Cl, Br, I) in mid-ocean ridge basalts: a Macquarie Island case study. *Geochim. Cosmochim. Acta* **81**, 82–93.
- Kent A. J. R., Norman M. D., Hutcheon I. D. and Stolper E. M. (1999) Assimilation of seawater-derived components in an oceanic volcano: evidence from matrix glasses and glass inclusions from Loihi seamount, Hawaii. *Chem. Geol.* **156**, 299–319.
- Kent A. J. R., Peate D. W., Newman S., Stolper E. M. and Pearce J. A. (2002) Chlorine in submarine glasses from the Lau Basin: seawater contamination and constraints on the composition of slab-derived fluids. *Earth Planet. Sci. Lett.* **202**, 361–377.
- Kepler H. (2010) The distribution of sulfur between haplogranitic melts and aqueous fluids. *Geochim. Cosmochim. Acta* **74**, 645–660.
- Kingsley R. H. and Schilling J. G. (1995) Carbon in mid-atlantic ridge basalt glasses from 28°N to 63°N – evidence for a carbon-enriched azores mantle plume. *Earth Planet. Sci. Lett.* **129**, 31–53.
- Kiseeva E. S. and Wood B. J. (2015) The effects of composition and temperature on chalcophile and lithophile element partitioning into magmatic sulphides. *Earth Planet. Sci. Lett.* **424**, 280–294.
- Kogiso T., Hirschmann M. M. and Reiners P. W. (2004) Length scales of mantle heterogeneities and their relationship to ocean island basalt geochemistry. *Geochim. Cosmochim. Acta* **68**, 345–360.
- Kohlstedt D. L. and Mackwell S. J. (1998) Diffusion of hydrogen and intrinsic point defects in olivine. *Zeitschrift für physikalische Chemie* **207**, 147–162.
- Langmuir C. H. and Bender J. F. (1984) The geochemistry of oceanic basalts in the vicinity of transform faults: observations and implications. *Earth Planet. Sci. Lett.* **69**, 107–127.
- Langmuir C. H., Klein E. M. and Plank T. (1993) Petrological systematics of mid-ocean ridge basalts: constraints on melt generation beneath ocean ridges. *Mantle Flow Melt Generat. Mid-Ocean Ridge*, 183–280.
- Lassiter J. C., Hauri E. H., Nikogosian I. K. and Barszczus H. G. (2002) Chlorine-potassium variations in melt inclusions from Raivavae and Rapa, Austral Islands: constraints on chlorine recycling in the mantle and evidence for brine-induced melting of oceanic crust. *Earth Planet. Sci. Lett.* **202**, 525–540.
- Le Bas M., Le Maitre R., Streckeis A. and Zanettin B. (1986) A chemical classification of volcanic rocks based on the total alkali-silica diagram. *J. Petrol.* **27**, 745–750.
- le Roux P. J., Shirey S. B., Hauri E. H., Perfit M. R. and Bender J. F. (2006) The effects of variable sources, processes and contaminants on the composition of northern EPR MORB (8–10°N and 12–14°N): evidence from volatiles (H₂O, CO₂, S) and halogens (F, Cl). *Earth Planet. Sci. Lett.* **251**, 209–231.
- Le Voyer M., Cottrell E., Kelley K. A., Brounce M. and Hauri E. H. (2015) The effect of primary versus secondary processes on the volatile content of MORB glasses: An example from the equatorial Mid-Atlantic Ridge (5°N–3°S). *J. Geophys. Res.* **120**, 125–144.
- Lee J. K. (1995) Multipath diffusion in geochronology. *Contrib. Mineral. Petrol.* **120**, 60–82.
- Lesne P., Kohn S. C., Blundy J., Witham F., Botchornikov R. E. and Behrens H. (2011) Experimental simulation of closed-system degassing in the system basalt–H₂O–CO₂–S–Cl. *J. Petrol.* **52**, 1737–1762.
- Liu Y. N., Samaha N. T. and Baker D. R. (2007) Sulfur concentration at sulfide saturation (SCSS) in magmatic silicate melts. *Geochim. Cosmochim. Acta* **71**, 1783–1799.
- Lorand J. (1990) Are spinel Iherzolite xenoliths representative of the abundance of sulfur in the upper mantle? *Geochim. Cosmochim. Acta* **54**, 1487–1492.
- Macdonald G. A. and Katsura T. (1964) Chemical composition of Hawaiian Lavas. *J. Petrol.* **5**, 82–133.
- Mackwell S. J. and Kohlstedt D. L. (1990) Diffusion of hydrogen in olivine: implications for water in the mantle. *J. Geophys. Res.* **95**, 5079–5088.
- Mallick S., Salters V. J. M. and Langmuir C. H. (in revision) Geochemical variability along the northern East Pacific Rise: Coincident source composition and ridge segmentation. *Geochim. Geophys. Geosyst.*
- Marty B. (2012) The origins and concentrations of water, carbon, nitrogen and noble gases on Earth. *Earth Planet. Sci. Lett.* **313**, 56–66.
- Marty B. and Tolstikhin I. N. (1998) CO₂ fluxes from mid-ocean ridges, arcs and plumes. *Chem. Geol.* **145**, 233–248.
- Marty B. and Zimmermann L. (1999) Volatiles (He, C, N, Ar) in mid-ocean ridge basalts: assessment of shallow-level fractionation and characterization of source composition. *Geochim. Cosmochim. Acta* **63**, 3619–3633.
- Mavrogenes J. A. and O'Neill H. S. C. (1999) The relative effects of pressure, temperature and oxygen fugacity on the solubility of sulfide in mafic magmas. *Geochim. Cosmochim. Acta* **63**, 1173–1180.
- McDonough W. F. and Sun S. S. (1995) The composition of the Earth. *Chem. Geol.* **120**, 223–253.

- McKenzie D. (1984) The generation and compaction of partially molten rock. *J. Petrol.* **25**, 713–765.
- McKenzie D. (1985) The extraction of magma from the crust and mantle. *Earth Planet. Sci. Lett.* **74**, 81–91.
- McKenzie D. (2000) Constraints on melt generation and transport from U-series activity ratios. *Chem. Geol.* **162**, 81–94.
- McKenzie D. and Bickle M. J. (1988) The volume and composition of Melt generated by extension of the lithosphere. *J. Petrol.* **29**, 625–679.
- Medard E. and Grove T. L. (2008) The effect of H₂O on the olivine liquidus of basaltic melts: experiments and thermodynamic models. *Contrib. Mineral. Petrol.* **155**, 417–432.
- Michael P. J. (1988) The concentration, behavior and storage of H₂O in the suboceanic upper mantle – implications for mantle metasomatism. *Geochim. Cosmochim. Acta* **52**, 555–566.
- Michael P. J. (1995) Regionally distinctive sources of depleted MORB – evidence from trace-elements and H₂O. *Earth Planet. Sci. Lett.* **131**, 301–320.
- Michael P. J. and Chase R. L. (1987) The influence of primary magma composition, H₂O and pressure on Midocean Ridge basalt differentiation. *Contrib. Mineral. Petrol.* **96**, 245–263.
- Michael P. J. and Cornell W. C. (1998) Influence of spreading rate and magma supply on crystallization and assimilation beneath mid-ocean ridges: evidence from chlorine and major element chemistry of mid-ocean ridge basalts. *J. Geophys. Res.* **103**, 18325–18356.
- Michael P. J. and Graham D. W. (2013) Concentration and behavior of CO₂ in MORB and OIB: a reevaluation, Goldschmidt 2013 Conference Abstracts, p. 1752.
- Montesi L. G. J. and Behn M. D. (2007) Mantle flow and melting underneath oblique and ultraslow mid-ocean ridges. *Geophys. Res. Lett.* **34**.
- Morgan J. P. and Forsyth D. W. (1988) Three-dimensional flow and temperature perturbations due to a transform offset: effects on oceanic crustal and upper mantle structure. *J. Geophys. Res.* **93**, 2955–2966.
- Morgan J. W. (1986) Ultramafic xenoliths – clues to Earth's late accretionary history. *J. Geophys. Res.* **91**, 2375–2387.
- Murase T. and McBirney A. R. (1973) Properties of some common igneous rocks and their melts at high temperatures. *Geol. Soc. Am. Bull.* **84**, 3563–3592.
- Nishimura C. E. and Forsyth D. W. (1989) The anisotropic structure of the upper mantle in the Pacific. *Geophys. J. Int.* **96**, 203–229.
- Niu Y. L. and Batiza R. (1997) Trace element evidence from seamounts for recycled oceanic crust in the eastern Pacific mantle. *Earth Planet. Sci. Lett.* **148**, 471–483.
- Niu Y. L., Collerson K. D., Batiza R., Wendt J. I. and Regelous M. (1999) Origin of enriched-type mid-ocean ridge basalt at ridges far from mantle plumes: the East Pacific Rise at 11°20'N. *J. Geophys. Res.* **104**, 7067–7087.
- Niu Y. L., Regelous M., Wendt J. I., Batiza R. and O'Hara M. J. (2002) Geochemistry of near-EPR seamounts: importance of source vs. process and the origin of enriched mantle component. *Earth Planet. Sci. Lett.* **199**, 327–345.
- Niu Y. L., Waggoner D. G., Sinton J. M. and Mahoney J. J. (1996) Mantle source heterogeneity and melting processes beneath seafloor spreading centers: the East Pacific Rise, 18–19°S. *J. Geophys. Res.* **101**, 27711–27733.
- O'Neill H. S. C. and Mavrogenes J. A. (2002) The sulfide capacity and the sulfur content at sulfide saturation of silicate melts at 1400 °C and 1 bar. *J. Petrol.* **43**, 1049–1087.
- Patten C., Barnes S.-J., Mathez E. A. and Jenner F. E. (2013) Partition coefficients of chalcophile elements between sulfide and silicate melts and the early crystallization history of sulfide liquid: LA-ICP-MS analysis of MORB sulfide droplets. *Chem. Geol.* **358**, 170–188.
- Perfit M., Fornari D., Ridley W., Kirk P., Casey J., Kastens K., Reynolds J., Edwards M., Desonie D. and Shuster R. (1996) Recent volcanism in the Siqueiros transform fault: picritic basalts and implications for MORB magma genesis. *Earth Planet. Sci. Lett.* **141**, 91–108.
- Pickle R. C., Forsyth D. W., Harmon N., Nagle A. N. and Saal A. (2009) Thermo-mechanical control of axial topography of intra-transform spreading centers. *Earth Planet. Sci. Lett.* **284**, 343–351.
- Portner R. A., Daczko N. R. and Dickinson J. A. (2010) Vitriclastic lithofacies from Macquarie Island (Southern Ocean): compositional influence on abyssal eruption explosivity in a dying Miocene spreading ridge. *Bull. Volcanol.* **72**, 165–183.
- Priestley K. and McKenzie D. (2006) The thermal structure of the lithosphere from shear wave velocities. *Earth Planet. Sci. Lett.* **244**, 285–301.
- Quilty P. G., Crundwell M. P. and Wise S. W. (2008) Microplankton provide 9 Ma age for sediment in the Macquarie Island ophiolite complex. *Aust. J. Earth. Sci.* **55**, 1119–1125.
- Reynolds J. R. and Langmuir C. H. (1997) Petrological systematics of the Mid-Atlantic Ridge south of Kane: implications for ocean crust formation. *J. Geophys. Res.* **102**, 14915–14946.
- Rosenthal A., Hauri E. and Hirschmann M. (2015) Experimental determination of C, F, and H partitioning between mantle minerals and carbonated basalt, CO₂/Ba and CO₂/Nb systematics of partial melting, and the CO₂ contents of basaltic source regions. *Earth Planet. Sci. Lett.* **412**, 77–87.
- Rudge J. F., MacLennan J. and Stracke A. (2013) The geochemical consequences of mixing melts from a heterogeneous mantle. *Geochim. Cosmochim. Acta* **114**, 112–143.
- Ruff L. J., Given J. W., Sanders C. O. and Sperber C. M. (1989) Large earthquakes in the Macquarie Ridge complex – transitional tectonics and subduction initiation. *Pure Appl. Geophys.* **129**, 71–129.
- Saal A., Kurz M., Hart S., Blusztajn J., Blichert-Toft J., Liang Y. and Geist D. (2007) The role of lithospheric gabbros on the composition of Galapagos lavas. *Earth Planet. Sci. Lett.* **257**, 391–406.
- Saal A. E., Hauri E. H., Langmuir C. H. and Perfit M. R. (2002) Vapour undersaturation in primitive mid-ocean-ridge basalt and the volatile content of Earth's upper mantle. *Nature* **419**, 451–455.
- Salters V. J. and Stracke A. (2004) Composition of the depleted mantle. *Geochem. Geophys. Geosyst.* **5**.
- Schilling J. G., Bergeron M. B. and Evans R. (1980) Halogens in the Mantle beneath the North-Atlantic. *Philos. Trans. R. Soc. Lond. A* **297**, 147–178.
- Shaw A., Hauri E., Fischer T., Hilton D. and Kelley K. (2008) Hydrogen isotopes in Mariana arc melt inclusions: implications for subduction dehydration and the deep-Earth water cycle. *Earth Planet. Sci. Lett.* **275**, 138–145.
- Shen Y. and Forsyth D. W. (1992) The effects of temperature- and pressure-dependent viscosity on three-dimensional passive flow of the mantle beneath a ridge-transform system. *J. Geophys. Res.* **97**, 19717–19728.
- Shen Y. and Forsyth D. W. (1995) Geochemical constraints on initial and final depths of melting beneath mid-ocean ridges. *J. Geophys. Res.* **100**, 2211–2237.
- Simons K., Dixon J., Schilling J. G., Kingsley R. and Poreda R. (2002) Volatiles in basaltic glasses from the Easter-Salas y Gomez Seamount Chain and Easter Microplate: Implications for geochemical cycling of volatile elements. *Geochem. Geophys. Geosys.* **3**.

- Sims K. W. W., Goldstein S. J., Blichert-Toft J., Perfit M. R., Kelemen P., Fornari D. J., Michael P., Murrell M. T., Hart S. R., DePaolo D. J., Layne G., Ball L., Jull M. and Bender J. (2002) Chemical and isotopic constraints on the generation and transport of magma beneath the East Pacific Rise. *Geochim. Cosmochim. Acta* **66**, 3481–3504.
- Sinton J. M. and Detrick R. S. (1992) Mid-ocean ridge magma chambers. *J. Geophys. Res.* **97**, 197–216.
- Sinton J. M. and Fryer P. (1987) Mariana Trough lavas from 18°N: implications for the origin of back arc basin basalts. *J. Geophys. Res.* **92**, 12782–12802.
- Smith P. M. and Asimow P. D. (2005) Adibat_1ph: A new public front-end to the MELTS, pMELTS, and pHMELTS models. *Geochem. Geophys. Geosyst.* **6**.
- Sobolev A. V. and Chaussidon M. (1996) H₂O concentrations in primary melts from supra-subduction zones and mid-ocean ridges: implications for H₂O storage and recycling in the mantle. *Earth Planet. Sci. Lett.* **137**, 45–55.
- Sobolev A. V., Hofmann A. W., Kuzmin D. V., Yaxley G. M., Arndt N. T., Chung S.-L., Danyushevsky L. V., Elliott T., Frey F. A., Garcia M. O., Gurenko A. A., Kamenetsky V. S., Kerr A. C., Krivolutsкая N. A., Matvienkov V. V., Nikogosian I. K., Rocholl A., Sgurdsson I. A., Sushchevskaya N. M. and Teklay M. (2007) The amount of recycled crust in sources of mantle-derived melts. *Science* **316**, 412–417.
- Soule S., Nakata D., Fornari D., Fundis A., Perfit M. and Kurz M. (2012) CO₂ variability in mid-ocean ridge basalts from sym-emplacment degassing: constraints on eruption dynamics. *Earth Planet. Sci. Lett.* **327**, 39–49.
- Sparks D. W. and Parmentier E. (1991) Melt extraction from the mantle beneath spreading centers. *Earth Planet. Sci. Lett.* **105**, 368–377.
- Sparks R. S. J. (1978) The dynamics of bubble formation and growth in magmas: a review and analysis. *J. Volcanol. Geotherm. Res.* **3**, 1–37.
- Stracke A. (2012) Earth's heterogeneous mantle: a product of convection-driven interaction between crust and mantle. *Chem. Geol.* **330**, 274–299.
- Stracke A. and Bourdon B. (2009) The importance of melt extraction for tracing mantle heterogeneity. *Geochim. Cosmochim. Acta* **73**, 218–238.
- Stronck N. A. and Haase K. M. (2004) Chlorine in oceanic intraplate basalts: constraints on mantle sources and recycling processes. *Geology* **32**, 945–948.
- Tenner T. J., Hirschmann M. M. and Humayun M. (2012) The effect of H₂O on partial melting of garnet peridotite at 3.5 GPa. *Geochem. Geophys. Geosyst.* **13**.
- Todt W., Cliff R. A., Hanser A. and Hofmann A. (1996) Evaluation of a 202Pb–205Pb Double spike for high-precision lead isotope analysis. *Earth processes: reading the isotopic code*, 429–437.
- van Keken P. E., Hauri E. H. and Ballentine C. J. (2002) Mantle mixing: the generation, preservation, and destruction of chemical heterogeneity. *Annu. Rev. Earth Planet. Sci. Lett.* **30**, 493–525.
- Van Orman J. A., Grove T. L. and Shimizu N. (2001) Rare earth element diffusion in diopside: influence of temperature, pressure, and ionic radius, and an elastic model for diffusion in silicates. *Contrib. Mineral. Petrol.* **141**, 687–703.
- Vanko D. A. (1988) Temperature, pressure, and composition of hydrothermal fluids, with their bearing on the magnitude of tectonic uplift at mid-ocean ridges, inferred from fluid inclusions in oceanic layer 3 rocks. *J. Geophys. Res.* **93**, 4595–4611.
- Varne R., Brown A. V., Jenner G. A. and Falloon T. (2000) Macquarie Island: its geology and structural history, and the timing and tectonic setting of its N-MORB to E-MORB magmatism. In *Ophiolites and Oceanic Crust: New Insights from Field Studies and Ocean Drilling Program* (eds. Y. Dilek, E. M. Moores, D. Elthon and A. Nicolas). Geological Society of America Special Publication.
- Varne R., Gee R. D. and Quilty P. G. J. (1969) Macquarie Island and Cause of oceanic linear magnetic anomalies. *Science* **166**, 230–233.
- Wallace P. and Carmichael I. S. E. (1992) Sulfur in basaltic magmas. *Geochim. Cosmochim. Acta* **56**, 1863–1874.
- Wallace P. J. (2005) Volatiles in subduction zone magmas: concentrations and fluxes based on melt inclusion and volcanic gas data. *J. Volcanol. Geotherm. Res.* **140**, 217–240.
- Walter M. J. (1998) Melting of garnet peridotite and the origin of komatiite and depleted lithosphere. *J. Petrol.* **39**, 29–60.
- Wanless V., Perfit M., Ridley W., Wallace P., Grimes C. and Klein E. (2011) Volatile abundances and oxygen isotopes in basaltic to dacitic lavas on mid-ocean ridges: the role of assimilation at spreading centers. *Chem. Geol.* **287**, 54–65.
- Warren J. and Shimizu N. (2010) Cryptic variations in abyssal peridotite compositions: evidence for shallow-level melt infiltration in the oceanic lithosphere. *J. Petrol.* **51**, 395–423.
- Warren J. M. and Hauri E. H. (2014) Pyroxenes as tracers of mantle water variations. *J. Geophys. Res.* **119**, 1851–1881.
- Warren J. M., Shimizu N., Sakaguchi C., Dick H. J. and Nakamura E. (2009) An assessment of upper mantle heterogeneity based on abyssal peridotite isotopic compositions. *J. Geophys. Res.* **114**.
- Wasylenki L. E., Baker M. B., Kent A. J. and Stolper E. M. (2003) Near-solidus melting of the shallow upper mantle: partial melting experiments on depleted peridotite. *J. Petrol.* **44**, 1163–1191.
- Wendt J. I., Regelous M., Niu Y., Hékinian R. and Collerson K. D. (1999) Geochemistry of lavas from the Garrett Transform Fault: insights into mantle heterogeneity beneath the eastern Pacific. *Earth Planet. Sci. Lett.* **173**, 271–284.
- Wilson L., Sparks R. S. J. and Walker G. P. (1980) Explosive volcanic eruptions—IV. The control of magma properties and conduit geometry on eruption column behaviour. *Geophys. J. Int.* **63**, 117–148.
- Witham F., Blundy J., Kohn S. C., Lesne P., Dixon J., Churakov S. V. and Botcharnikov R. (2012) SolEx: a model for mixed COHSCI-volatile solubilities and exsolved gas compositions in basalt. *Comput. Geosci.* **45**, 87–97.
- Workman R. K. and Hart S. R. (2005) Major and trace element composition of the depleted MORB mantle (DMM). *Earth Planet. Sci. Lett.* **231**, 53–72.
- Workman R. K., Hauri E., Hart S. R., Wang J. and Blusztajn J. (2006) Volatile and trace elements in basaltic glasses from Samoa: implications for water distribution in the mantle. *Earth Planet. Sci. Lett.* **241**, 932–951.
- Wykes J. L., O'Neill H. S. C. and Mavrogenes J. A. (2015) The effect of FeO on the sulfur content at sulfide saturation (SCSS) and the selenium content at selenide saturation of silicate melts. *J. Petrol.* **56**, 1407–1424.
- Zajacz Z., Candela P. A., Piccoli P. M. and Sanchez-Valle C. (2012) The partitioning of sulfur and chlorine between andesite melts and magmatic volatiles and the exchange coefficients of major cations. *Geochim. Cosmochim. Acta* **89**, 81–101.
- Zhang Y. and Liu L. (2012) On diffusion in heterogeneous media. *Am. J. Sci.* **312**, 1028–1047.
- Zhang Y., Xu Z., Zhu M. and Wang H. (2007) Silicate melt properties and volcanic eruptions. *Rev. Geophys.* **45**.